37th Annual Condensed Matter and Materials Meeting

Wagga 2013

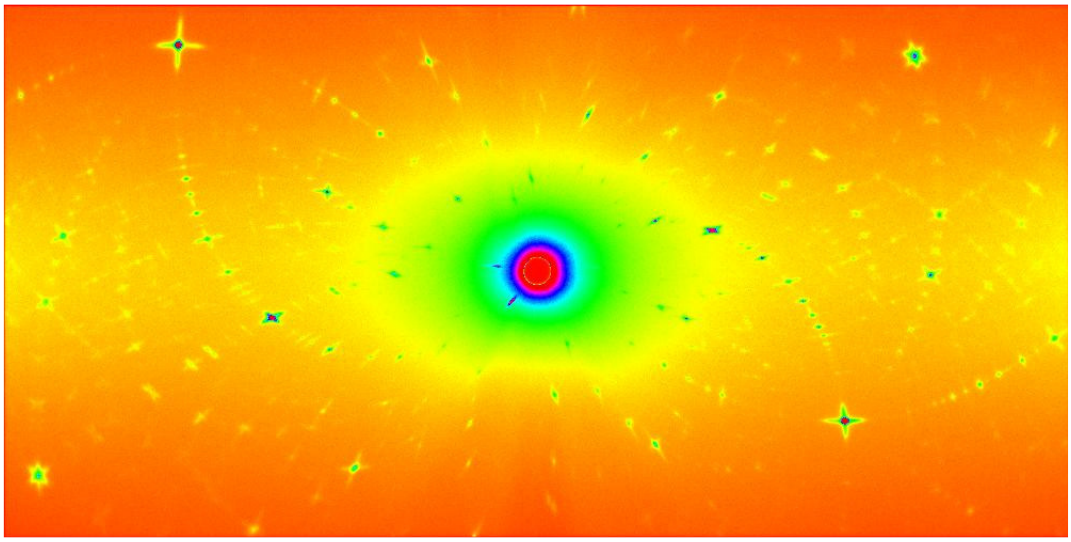

Charles Sturt University, Wagga Wagga, NSW
5th February – 8th February, 2013

ISBN: 978-0-646-59459-0

Editorial Note
Proceedings of Wagga 2013
The 37th Annual Condensed Matter and Materials Meeting
ISBN: 978-0-646-59459-0
Editors: Garry McIntyre and Richard Mole

The 37th Annual Condensed Matter and Materials Meeting was held at Charles Sturt University, Wagga Wagga, NSW from 5th – 8th February, 2013. There were 88 attendees, including international visitors from Singapore, Brazil, Turkey and Germany. A total of 11 invited and 18 contributed oral papers were presented during the two and one half days of scientific sessions. There were also two sessions with a total of 53 poster presentations. All presenters were invited to submit a manuscript for publication in the conference proceedings. Each manuscript was refereed by at least two anonymous reviewers who worked to a set of guidelines made available by the editors. Each accepted publication therefore satisfies the requirements for classification as a refereed conference publication (E1). The organizers would like to thank the 25 reviewers for their time and effort in reviewing manuscripts, which resulted in 14 papers being accepted for publication. The accepted manuscripts are available at the on-line publication section of the Australian Institute of Physics national web site (http://www.aip.org.au/).

Organising committee: Garry McIntyre, Richard Mole, Kate Picirillo, Gordon Thoroughgood and Anna Paradowska

May 2014

2013 OVERALL TIMETABLE

Tuesday 5 February

16:00 -	Registration desk open
16:00 – 18:00	*Conference bar open*
18:00 – 19:30	*Dinner*
19:00 -	Posters wp1-wp28 to be mounted
19:30 – 21:00	*Wine, beer, and cheese tasting*

Wednesday 6 February

07:30 – 08:30	*Breakfast*
09:00 – 09:10	Conference opening
09:10 – 10:30	Oral Session: Papers wo1-wo3
10:30 – 11:00	*Morning tea*
11:00 – 12:30	Oral Session: Papers wo4-wo7
12:30 – 14:00	*Lunch*
14:00 – 14:50	Oral Session: Papers wo9, tp3
14:50 – 15:30	Poster Clips: wp1-wp28
15:30 – 16:00	*Afternoon Tea*
16:00 – 18:00	Poster Session: Papers wp1-wp28
18:00 -	Posters**:** tp1-tp25 to be mounted
16:30 – 18:00	*Conference bar open*
18:30 – 22:00	*Conference Dinner*

Thursday 7 February

07:30 – 08:30	*Breakfast*
09:00 – 10:30	Oral Session: Papers to1-to4
10:30 – 11:00	*Morning tea*
11:00 – 12:30	Oral Session: Papers wo8, to6-to8
12:30 – 14:00	*Lunch*
14:00 – 15:00	Oral Session: Papers to9-to10
15:00 – 15:30	Poster Clips: tp1-tp25
15:30 – 16:00	*Afternoon Tea*
16:00 – 18:00	Poster Session: tp1-tp25
16:30 – 18:00	*Conference bar open*
18:00 – 19:30	*Dinner*
19:30 – 22:00	Trivia Quiz (Lindsay Davis Cup)

Friday 8 February

07:30 – 08:30	*Breakfast*
09:00 – 10:30	Oral Session: Papers fo1-fo4
10:30 – 11:00	*Morning tea*
11:00 – 12:20	Oral Session: Papers fo5-fo7
12:20 – 12:40	Presentations and Closing
12:40 – 14:00	*Lunch*

2013 PROGRAM

Tuesday 5 February

16:00 -		Registration desk open
16:00 – 18:00		Conference bar open
18:00 – 19:30		Dinner
19:30 – 21:00		Wine, beer, and cheese tasting

Wednesday 6 February

09:00 – 09:10 **Opening: *Garry McIntyre, ANSTO***

09:10 – 10:30 **Chairperson: *Stephen Collocott, CSIRO Lindfield***

09:10 – 09:40 wo1 Magnetic Structures of Rare-Earth Intermetallics: A two-pronged Attack Featuring Neutron Diffraction and Rare-Earth Mössbauer Spectroscopy
Seán Cadogan, UNSW Canberra *INVITED*

09:40 – 10:00 wo2 Optical Investigation of the Magnetoelectric Coupling via Phonons and Electromagnons in Multiferroics
Pauline Rovillain, UNSW Kensington/ANSTO

10:00 – 10:30 wo3 Coupling Between Electronic and Lattice Degrees of Freedom in 4f-Electron Systems Investigated by Inelastic Neutron Scattering
Michael Loewenhaupt, IFP Dresden *INVITED*

10:30 – 11:00 Morning tea

11:00 – 12:30 **Chairperson: *Jeff Sellar, Monash University***

11:00 – 11:30 wo4 Atomic Scale Modelling for Real Nuclear Engineering Problems and Applications
Simon Middleburgh, ANSTO *INVITED*

11:30 – 11:50 wo5 Measuring Homogeniety of Metallic Glasses Using Novel Scanning/Transmission Electron Microscopy Techniques
Amelia Liu, Monash University

11:50 – 12:10 wo6 Micron Resolution Strain Spectroscopy of a Rare-Earth Ion Doped Crystal
John Bartholomew, Australian National University

12:10 – 12.30 wo7 A One-Dimensional Spin-Orbit Interferometer
Tommy Li, UNSW Kensington

12:30 – 14.00 Lunch

14:00 – 15:40 **Chairperson: *Roger Lewis, University of Wollongong***

14:00 – 14:30 wo8 High Resolution Dynamic Imaging at the Australian Synchrotron
Daniel Häusermann, Australian Synchrotron *INVITED*

14:30 – 14:50 wo9 Element Specific and Depth-Resolved Interface Magnetism in $BiFeO_3/La_{0.67}Sr_{0.33}MnO_3$ Thin Films
Joel Bertinshaw, UNSW Kensington

14:50 – 15:10 wo10 Quantum Molecular Dynamics Simulation of Newly Developed Magnesium Based Bulk Metallic Glasses
Reza Mahjoub, UNSW Kensington

15:10 – 15:40 Poster Advertisement wp1-wp28: selected 2 minute talks

15:40 – 16:00		**Afternoon Tea**
16:00 – 18:00		**Poster Session:** wp1-wp28
18:30 – 22:00		**Conference Dinner**
	wo11	The Higgs Boson at the Large Hadron Collider *Sara Diglio, University of Melbourne* *INVITED*

Thursday 7 February

09:00 – 10:30		**Chairperson: *Chris Ling, University of Sydney***
09:00 – 09:30	to1	Power Generation in Remote Areas Using Concentrated Solar Thermal and Hydrogen *Craig Buckley, Curtin University* *INVITED*
09:30 – 09:50	to2	A Novel Multi-Scale Modelling Approach for Determining the Bulk Properties of Difficult-to-Characterise Composites *Paul Mignone, University of Melbourne*
09:50 – 10:10	to3	MD Simulation and Experimental INS: A Marriage in Atomic Dynamics *Elvis Shoko, ANSTO*
10:10 – 10:30	to4	The Search for Optically Addressable Single Spins in the Solid State: Lessons Learnt from the NV Colour Centre in Diamond *Marcus Doherty, ANU*
10:30 – 11:00		**Morning tea**
11:00 – 12:30		**Chairperson: *Richard Mole, ANSTO***
11:00 – 11:30	to5	Graphene and Topological Insulators: In What Ways Are the Transport Propoerties Different from Other Two Dimensional Electron Gases *Shaffique Adam, Yale-NUS College, Singapore* *INVITED*
11:30 – 11:50	to6	Effect of External Electric Field on the Application of Graphene *Zhimin Ao, UNSW Kensington*
11:50 – 12:10	to7	Haldane-Like Models in Buckled Lattices *Anthony Wright, University of Queensland*
12:10 – 12:30	to8	Time Resolved Magnetic Depth Profiles of a Thin Film Using Polarized Neutron Reflectometry *David Cortie, University of Wollongong*
12:30 – 14.00		**Lunch**
14:00 – 15:40		**Chairperson: *Oleg Sushkov, UNSW***
14:00 – 14:30	to9	Transforming Carbon Onions into Nanodiamond: a New Pathway to sp^3 Carbon with Astrophysical Implications *Nigel Marks, Curtin University* *INVITED*
14:30 – 14:50	to10	Magnetic Neutron Scattering on Nanomagnets: Decrypting Cross-Section Images Using Micromagnetic Simulations *Andreas Michel, University of Luxembourg*
14:50 – 15.10	to11	Ferromagnetism in Teflon *Jiabao Yi, UNSW Kensington*
15:10 – 15:40		Poster Advertisement tp1-tp25: selected 2 minute talks
15:40 – 16:00		**Afternoon Tea**

16:00 – 18:00 **Poster Session:** tp1-tp25

18:00 – 19:30 **Dinner**

19:30 – 22:00 **Trivia Quiz, Conference Centre**
Quizmaster: Trevor Finlayson, University of Melbourne

Friday 8 February

09:00 – 10:30 **Chairperson: *Lou Vance, ANSTO***

09:00 – 09:30 fo1 Polyamorphism: Fact or Fiction?
Simon Clark, Macquarie University and ANSTO *INVITED*

09:30 – 09:50 fo2 Novel Block Co-polymer of DGEBA and Poly(trimethylene terephthalate): Preparation, Characterization and Properties
Sarath Chandran, Mahatma Gandhi University, Kottayam, India

09:50 – 10:10 fo3 Effects of Strain on the Electronic Properties of InAs/GaAs Core/Shell Nanowires: First Principles Study
Quanguo Jiang, UNSW Kensington

10:10 – 10:30 fo4 Exchange Bias in Neutron Irradiated Concentrated CuMn Spin Glass
Lester Barnsley, Griffith University

10:30 – 11:00 **Morning tea**

11:00 – 12:20 **Chairperson: *Stewart Campbell, UNSW Canberra***

11:00 – 11:30 fo5 What's so Exciting about Low Dimensional, Magnetic Copper Oxides?
Kirrily Rule, ANSTO *INVITED*

11:30 – 11:50 fo6 Spin Gap Evolution upon Ca Doping in the Spin Ladder Superconductor System $Sr_{14-x}Ca_xCu_{24}O_{41}$
Guochu Deng, ANSTO

11:50 – 12:20 fo7 Magnetism and Magnetic Structure of $TbNiAl_4$
Wayne Hutchison, UNSW Canberra *INVITED*

12:20 – 12:40 **Awards and Closing:**
Glen Stewart, UNSW Canberra, and Garry McIntyre, ANSTO

12:40 – 14:00 **Lunch**

2013 POSTER SESSION: Wednesday 6 February

Theory, modeling, simulation

wp1 Detecting Artificial Graphene in GaAs Heterostructures
S. Bladwell and O.P. Sushkov

wp2 Modeling of Electrostatic Potential on Artificial Graphene
Z.-L. Cai and O.P. Sushkov

wp3 Dynamic Phase Transitions in the Spin-1 Blume-Capel Model under an Oscillating Magnetic Field within the Path Probability Method*
M. Ertaş and M. Keskin

wp4 Phase Diagrams of Spin S=1 Bilinear-Biquadratic Heisenberg Models
C.J. Hamer and J. Oitmaa

wp5 Skyrmion Liquid and Skyrmion Glass in the Spin Spiral State of Underdoped Cuprates
R. Kumar and O.P. Sushkov

wp6 The Energy Cost of Measurement for a Specific Curie-Weiss Model
D.J. Miller

wp7 Domain Wall Functionality in Complex Oxides
J.Seidel

wp8 Chemical Bonding in Aluminium: Comparison between QCBED and DFT
A.E. Smith, P.N.H. Nakashima, and B.C. Muddle

wp9 Topological Insulating States in Ordinary Semiconductors
O.P. Sushkov and A. H. Castro Neto

wp10 Using Quantum Magnetic Oscillations to Observe the 'Topological' in Topological Insulators
A.R. Wright and R.H. McKenzie

Magnetism (transition metal, rare-earth, actinide)

wp11 The Effect of Dy on the Time Dependent Behaviour of the Magnetization in $Nd_{60-x}Fe_{30}Al_{10}Dy_x$, x = 0 to 4, Bulk Amorphous Ferromagnets
S.J. Collocott, X.H. Tan, and H. Xu

wp12 Magnetoelectric Coupling in $TbMnO_3$ Explored via Raman Spectroscopy
P.J. Graham, M. Bartkowiak, P. Rovillain, A.M. Mulders, M. Yethiraj, E. Pomjakushina, K. Conder, M. Kenzelmann, and C. Ulrich

wp13 Giant Magnetoelasticity at a Spin Gap Transition in the 5*d* Oxide $Ba_3BiIr_2O_9$
C.D. Ling, W. Miiller, B.J. Kennedy, and M. Avdeev

wp14 Magnetic Properties and Magnetocaloric Effect in Layered $NdMn_{1.7}V_{0.3}Si_2$
M.F. Md Din, J.L. Wang, R. Zeng, W.D. Hutchison, M.Avdeev, S.J. Kennedy, and S. X. Dou

wp15 ^{18}O Isotope Substitution on the Multiferroic Compound $DyMnO_3$
N. Narayanan, F. Li, W.D. Hutchison, N. Reynolds, P. Rovillain, C. Ulrich, J. Hester, G.J. McIntyre, and A.M. Mulders

wp16 Thermodynamic Properties of an Anisotropic Heisenberg Model for the XY Pyrochlore $Er_2Ti_2O_7$
J. Oitmaa and R.R.P. Singh

wp17 The Effect of Fe and Ni Substitution in Magnetocaloric MnCoGe
Q. Ren, W.D. Hutchison, J.L. Wang, W. Kemp, J.M. Cadogan, and S.J. Campbell

wp18 Investigations into the Magnetic and Crystal Field Excitations of the Orthorhombically Distorted Perovskites RVO_3 (R=Dy, Tb, Pr, Ce)
N. Reynolds, P. Rovillain, S. Danilkin, K. Schmalzl, M. Reehuis, S. Miyasaka, F. Fujioka, Y. Tokura, B. Keimer, G.J. McIntyre, and C. Ulrich

wp19 Magnetic Order and Spin-Reorientations in RGa (R = Dy, Ho and Er) Intermetallic Compounds
R.A. Susilo, J.M. Cadogan, D.H. Ryan, N.R. Lee-Hone, R. Cobas, S. Muñoz-Pérez, B. Rosendahl-Hansen, and M. Avdeev

wp20 Spin-Reorientation in GdGa
R.A. Susilo, J.M. Cadogan, D.H. Ryan, N.R. Lee-Hone, R. Cobas, and S. Muñoz-Pérez

wp21 Structure and Properties of New Technetium Compounds
G.J. Thorogood, B.J. Kennedy, M. Avdeev, J. Ting, Z. Zhang, and G.R. Lumpkin

wp22 Magnetic Properties and Magnetocaloric Effect in $Mn_{0.9}Ti_{0.1}CoGe$
J.L. Wang, P. Shamba, W.D. Hutchison, M.F. Md Din, M. Avdeev, S.J. Kennedy, S.J. Campbell, R. Zeng, and S.X. Dou

Nanoscience (nanomaterials, spintronics, molecular magnetism)

wp23 Black Hydrogenated Titanium Dioxide
P. Imperia, R. Aldus, N. Booth, J. Muir, V. Jovic, and G. Waterhouse

wp24 Magnetic Properties of 3d Metal Nanoparticles Formed in SiO_2 via Ion Implantation
A.E. Malik, W.D. Hutchison, K. Nishimura, and R.G. Elliman

wp25 Explorations into the Electron-Phonon Interactions of the NV Colour Centre in Diamond
N.B. Manson and M.W. Doherty

wp26 ZnO/Ti-Compound Nanocomposites Prepared by Polyol Method
A. Murador Filho, D.I. dos Santos, J.G. Kim, D.Q. Shi, and S.X. Dou

wp27 Long-Range Transfer of Electron–Phonon Coupling in Oxide Superlattices
C. Ulrich, A.N. Driza, S. Blanco-Canosa, M. Bakr,, S. Soltan, M. Khalid, L. Mustafa, K. Kawashima, G. Christiani, H.-U. Habermeier, G. Khaliullin, M. Le Tacon, and B. Keimer

wp28 Controlled Synthesis of Nanocrystalline BaFCl:Sm^{3+} X-ray Storage Phosphor
X. Wang and H. Riesen

2013 POSTER SESSION: Thursday 7 February

Surfaces and interfaces

tp1 Analysis of Varied Richardson Constant Based on Numerical Device Model in Organic Light Emitting Diodes (OLEDs)
T. Hirai, K. Weber, J. O'Connell, M. Bown, and K. Ueno

tp2 Electron Self-Energy Variation from Rydberg Surface-State Resonances on Cu(110)
M.N. Read

tp3 Wettability and Electrical Conductivity Switching in UV Irradiated Graphene Films
Z. Xu, Z. Ao, D. Chu, and S. Li

Materials, engineering

tp4 Biomimetic Structure Design from Wood with Epoxy-Silica Composites
N. Daud and R.A. Shanks

tp5 In Scotch Whisky, Where Are the Fe^{3+} and Cu^{2+} Ions (EPR Detected) Formed?
S. Drew and G.J. Troup

tp6 Whither Wagga?
T.R. Finlayson and G.A. Stewart

tp7 Investigation of Residual Stresses in Aluminothermic Rail Welds
B. Khodabakhshi, A.M. Paradowska, P. Mutton, and R. Ibrahim

tp8 Residual Stresses in High Strength Steel Tubes for Large Scale Infrastructure
F.R. Mashiri, A.M. Paradowska, M. Khan, B. Uy, and Z. Tao

tp9 Non-Isothermal Crystallization Kinetics of Poly(lactic Acid)-Hemp Nanocomposites Plasticized with Tributyl Citrate
I.R. Mustapa, S. Chandran, R.A. Shanks, and I. Kong

tp10 Point Defect Engineering Strategies to Retard Phosphorous Diffusion in Germanium
H.A. Tahini, A. Chroneos, R.W. Grimes, U. Schwingenschlogel, and H. Bracht

tp11 U Valences and Site Occupancies in Doped $Gd_2Zr_2O_7$ Pyrochlore-Structured Nuclear Ceramics
E.R. Vance, D.J. Gregg, P. Gaugliardo, Y. Zhang, Z. Zhang, I. Karatchevtseva, G. Griffiths, J. Davis, G.R. Lumpkin, and G. Triani

Measurement techniques, instrumentation

tp12 An Alternative Recoil Implantation of the $^{100}Pd/^{100}Rh$ TDPAC Probe with Suppression of Elastically Scattered Projectiles
A.A. Abiona, W. Kemp, E. Williams, and H. Timmers

tp13 Epitaxial thin films of $La_{0.85}Ag_{0.15}MnO_3$ produced by Polymer Assisted Deposition
R. Cobas, S. Muñoz-Pérez, J.M. Cadogan, W.D. Hutchison, M.C. Ridgway, T. Puig, and X. Obradors

tp14 Time Resolved Magnetic Depth Profiles of a Thin Film Using Polarized Neutron Reflectometry
D.L. Cortie, X.L. Wang, K.-W. Lin, F. Klose, and A. Nelson

tp15 Attenuation and Multiple-Scattering Correction to a Neutron Time-of-Flight In-Situ Study
M.T. Crossley, E.MacA. Gray, C.J. Webb, and R.L. Smith

tp16 Commissioning of Polarised ^{3}He Based Neutron Polarisers and Analysers on OPAL Instruments
W.T. Lee, T. D'Adam, F. Klose, D. Jullien, K.H. Andersen, K.C. Rule, A.J. Studer, and S. Danilkin

tp17 On the AFNMR & NQR Signal Enhancement via Population Transfer
J.A. Lehmann-Horn and D.G. Miljak

tp18 Low Temperature THz Spectroscopy of 2, 4-dinitrotoluene
L.M. Lepodise and R. A. Lewis

tp19 Terahertz Emission From Lateral and Sideways Photo-Dember Effects
J. Mabon, K. Radhanpura, and R. A. Lewis

tp20 Neutron Laue Diffraction from Spin-Polarised Protons
G.J. McIntyre, M. Karlsson, F. Piegsa, B. van den Brandt, P. Hautle, T. Konter, O. Zimmer, E.M. Forgan, and C.J. Carlile

tp21 Pelican: An Inelastic Neutron Scattering Spectrometer With Polarization Analysis
R.A. Mole and D. Yu

tp22 Effect of Heavy Noble Gas Ion Irradiation on Terahertz Emission Efficiency of InP (100) and (111) Crystal Planes
K. Radhanpura and R. A. Lewis

tp23 Recent Developments for Taipan at ANSTO
K.C. Rule, S. Danilkin, A.P.J. Stampfl, and W.T Lee

tp24 A Be-Filter-Based Neutron Spectrometer for Vibrational Spectroscopy
A.P.J. Stampfl, A. Chellappah, K.C. Rule, S. Danilkin, G.J. Kearley, and J.A. Stride

tp25 Exploiting Fitted Electric Field Gradient Parameters: Axis Ambiguity and the Asymmetry Parameter Constraint, $0 < \eta < 1$
G.A. Stewart

Papers:

11. (tp5) In Scotch Whisky, From Where are the Fe^{3+} and Cu^{2+} Ions Sourced?

    Simon C. Drew, Blaine Roberts and G.J.Troup

12. (to2) A Novel Multi-scale Modelling Approach for Determining the Bulk Properties of Difficult-to-Characterise Composites

    P.J. Mignone, M. Wang, T.R. Finlayson, M.P. Echlin, A. Mottura, T.M. Pollock, D.P. Riley, G.V. Franks

13. (wp17) The Effect of Fe and Ni Substitution in Magnetocaloric MnCoGe

    Q. Y. Ren, W. D. Hutchison, J. L. Wang, W. Kemp, R. Cobas, J. M. Cadogan and S. J. Campbell

14. (to6) Effect of External Electric Field on the Application of Graphene

    Z. M. Ao, Q. G. Jiang, and S. Li

PROCEEDINGS - 37th ANNUAL CONDENSED MATTER AND MATERIALS MEETING, 5 - 8 February, 2013. Wagga Wagga, NSW, Australia

The S = 1 Bilinear Biquadratic Spin Model on the Square Lattice: A Series Expansion Study

J. Oitmaa and C.J. Hamer

School of Physics, The University of New South Wales, Sydney 2052, Australia.

We use extensive series expansions at T = 0 to investigate the phase diagram of a spin-1 Hamiltonian on the square lattice. The model includes bilinear and biquadratic interactions (the 'J-K' model) and has been studied recently using a variety of other methods. We find a clear indication of the three-sublattice order conjectured recently via indirect arguments. We also compute the energy and order parameter in the quadrupolar phases.

1. Introduction

There has been considerable interest recently in spin-1 Heisenberg models with both bilinear and biquadratic nearest-neighbour exchange terms. The generic Hamiltonian, which we refer to hereafter as the 'J-K ' model, is

$$H = J \sum_{<i,j>} \mathbf{S}_i \cdot \mathbf{S}_j + K \sum_{<I,j>} (\mathbf{S}_i \cdot \mathbf{S}_i)^2$$

The exchange parameters J, K may have either sign, and are often parametrized by J = cos θ, K = sin θ.

Studies of this Hamiltonian go back at least to the 1960s [1,2]. The mean-field phase diagram was discussed by Chen and Levy [2], where phases of both dipolar and quadrupolar nature were identified, and a more detailed discussion was given by Papanicolaou on the basis of semiclassical 'flavour-wave' theory [3]. More recently, the model on the triangular lattice was invoked to explain unusual properties of the material $NiGe_2S$ [4-7], and the presence of significant biquadratic exchange (with K < 0) in the iron pnictides has been suggested [8].

In the present paper we consider the model defined above on the two-dimensional square lattice. For K = 0, and by continuity for |K| << |J|, we expect a normal collinear ferromagnetic or antiferromagnetic (Néel) phase for J < 0, J > 0 respectively. In other regions of the phase diagram, phases with quadrupolar order, ferroquadrupolar (FQ) or antiferroquadrupolar (AFQ), may occur. Another feature of this Hamiltonian is the existence of special points (θ = π/4, -3π/4, ± π), where the spin symmetry group is enlarged from O(3) to U(3) [3].

In Figure 1 we show a schematic phase diagram, based on the flavour-wave theory of Papanicolaou [3], confirmed by Quantum Monte Carlo (QMC) studies [9,10] for K < 0, and a more recent study by Toth *et al.* [11] combining flavour-wave theory with numerical exact diagonalization. The phase structure is firmly established in the lower half of the phase diagram, where QMC calculations are valid, but not in the upper half, since QMC calculations suffer from a minus sign problem for K > 0. The most interesting quadrant is the region 0 < θ < π/2. Toth *et a*l. [11] find a 3-sublattice AFQ phase (termed 'AFQ3') to be stable throughout the region π/4 < θ < π/2. Their approach becomes less certain below θ = π/4, but they argue, by continuity, that a three-sublattice antiferromagnetic phase will be the preferred ground state in a finite window below θ = π/4. This is the conjectured AFM3 phase illustrated in Fig. 1, in which the spins

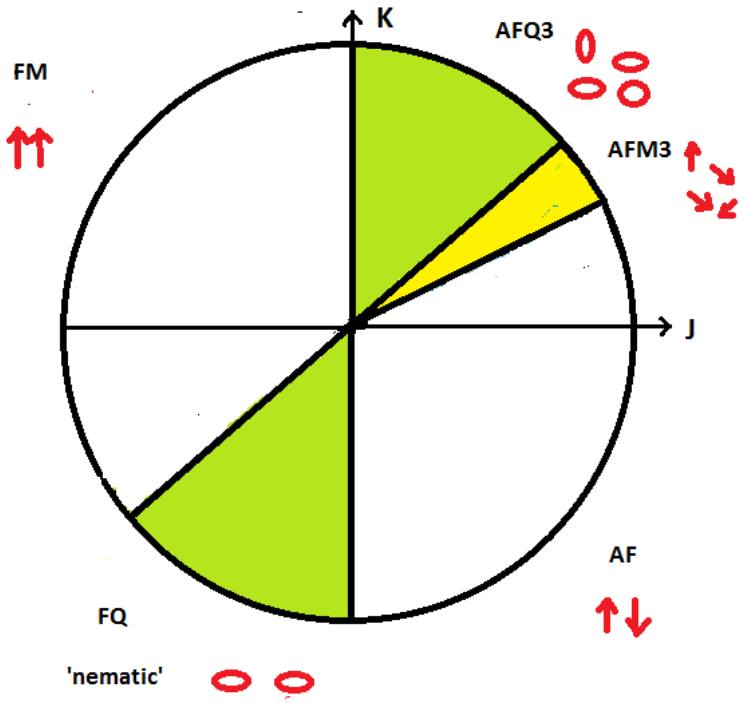

Fig. 1 Phase diagram as a function of angle θ. Key: FM: ferromagnetic; AF: antiferromagnetic; FQ: ferroquadrupolar; AFQ3: antiferroquadrupolar with 3-sublattice order; AFM3: antiferromagnetic, with 3-sublattice order.

are coplanar with a 120^0 angle between spins on successive diagonal sublattices.

The initial motivation for the present work was to find more direct evidence for the AFM3 phase, and to locate the position of the boundary between the AFM3 and Néel phases. At the same time we also obtain independent estimates of both the ground state energy and quadrupole moment in the quadrupolar phases. Given the inherent uncertainty in analytic approaches to S = 1 systems, it is important to test such results by other methods.

2. Method

In our calculations, we employ the method of linked cluster perturbation expansions [12], in which the Hamiltonian is written as

$$H = H_0 + \lambda V$$

and series are obtained for various quantities, such as ground state energy and order parameters, in powers of λ up to some order (typically 10-15). A basis is chosen in each phase, usually consisting of simple product states, where the ground state possesses the expected order in that phase. The unperturbed Hamiltonian H_0 then contains all the diagonal terms in that basis, and the perturbation V all the off-diagonal ones, so that the physical Hamiltonian corresponds to $\lambda = 1$. The series are analysed by standard methods (usually direct or Dlog Pade approximants), and evaluated at $\lambda = 1$. The unperturbed ground state is expected to be adiabatically connected to the true many-body ground state of the full Hamiltonian H. It is possible to check this by testing for a singularity with $\lambda < 1$ in the series. The method has been used successfully in many previous studies, including our previous work [13] on a spin-1 model with single-ion anisotropy.

The calculation then proceeds along standard lines [12], with series for a sequence of finite clusters of increasing size combined to give series for the bulk system in the thermodynamic limit. We have used a total of 23937 clusters with 14 or fewer sites, which yields series for the ground state energy per site $E_0(\lambda)$, the magnetization $M(\lambda) = \langle S^z_i \rangle$ and

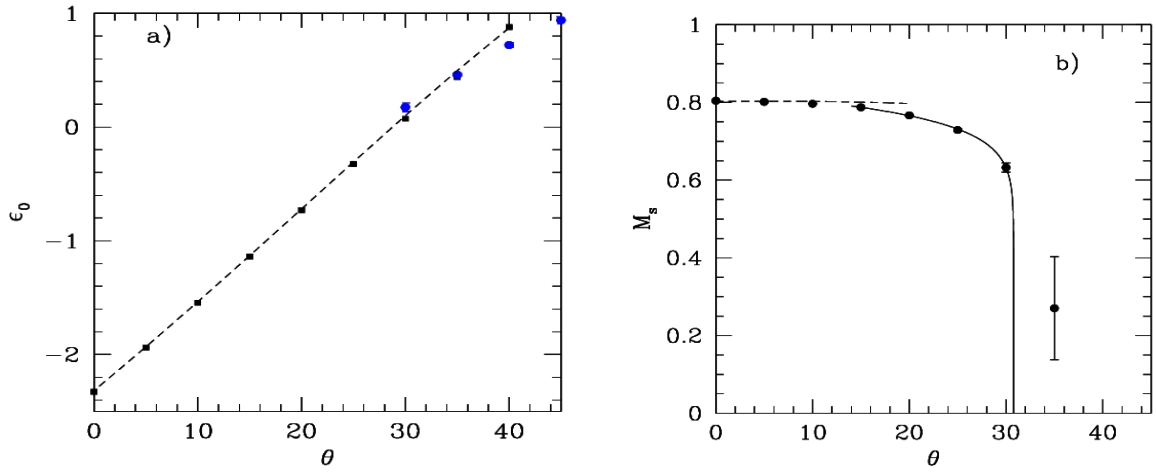

Fig.2. (a) Ground state energy per site from expansions in the Néel phase (black squares) and the AFM3 phase (blue circles). Dashed line: flavour-wave prediction; (b) Estimates of the magnetization in the Néel phase. Dashed line: flavour-wave prediction; solid line: a fit to the data.

the quantity $Q = \langle (S^z_i)^2 \rangle$, which is related to the quadrupole moment, to order λ^{15}. The series data are too extensive to reproduce here, but can be supplied on request. The results are discussed below.

3. Results

3.1 The Néel and AFM3 phases

We now turn to the results. In Fig. 2(a) we show the ground state energy per site, as a function of θ, from series in both the Néel and AFM3 phases. It can be seen that the Néel energy is the lower at small θ, until the AFM3 energy crosses over to become the lower at a transition point which we estimate around $\theta = 36^0$. This is in good agreement with the estimates of Toth *et a*l [11]. The flavour-wave estimate of the Néel energy is in extremely good agreement with the series results.

Figure 2(b) shows our estimates of the magnetization as a function of θ. It can be seen that the flavour-wave estimate is again very accurate at small θ. A fit to the simple form $M^z \sim a(\theta_c - \theta)^\beta$ to the data over the range $15 < \theta < 30$ degrees predicts that the magnetization vanishes at about $\theta = 31^0$, with a very small exponent $\beta \sim 0.1$. Even including the uncertain point at 35^0 in the fit gives a transition point near but below $\theta = 35^0$.

The transition from one ordered state to a state with different order is generally expected to be 1st order. From the data above, the transition between the Néel and AFM3 phases looks more like a 2nd order transition. If it is a 1st order transition, it must be a very weak one. Another possibility might be the existence of intermediate (spiral?) phases. We do not explore that possibility further here.

3.2 The AFQ3 Quadrupolar Phase

In the region $\pi/4 < \theta < \pi/2$, Toth *et al* [11] propose a 3-sublattice antiferroquadrupolar (AFQ3) phase. Our series results for the ground state energy per site and quadrupolar moment Q in this region are shown in Figs. 3(a) and 3(b), respectively. As can be seen from Fig. 3(a), our series results for the ground state energy are in excellent agreement with those of Toth *et al* in this region, and join on smoothly to those for the AFM3 phase. This argues for a 2nd order transition between the AFM3 and AFQ3 phases, presumably fixed at $\theta = 45^0$ by the higher symmetry obtaining there, where the dipolar AFM3 order parameter vanishes. Our

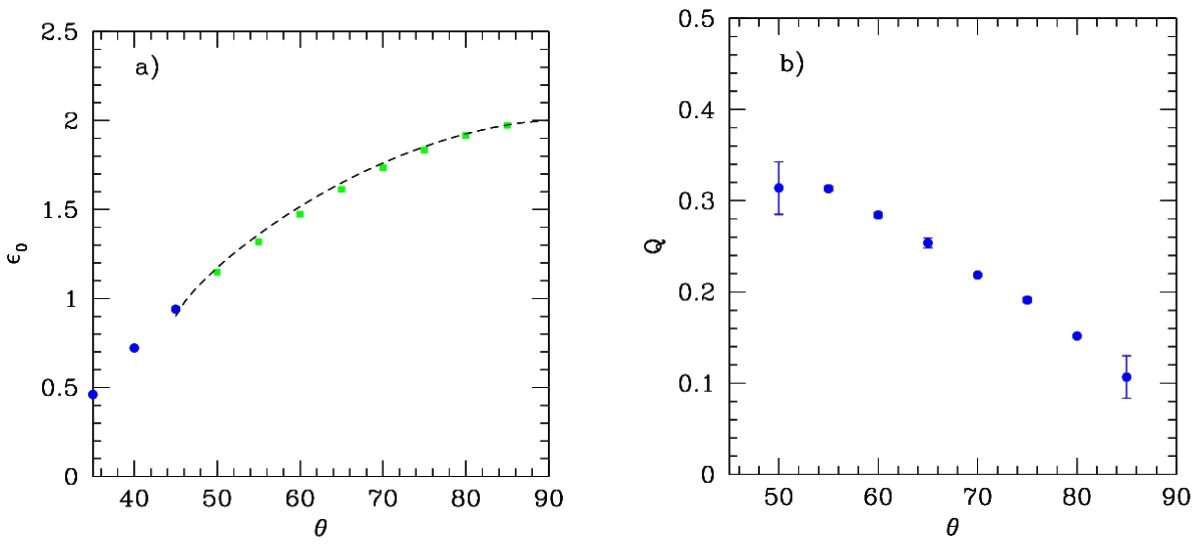

Fig.3. (a) Ground state energy per site from expansions in the AFQ3 phase (green squares) and the AFM3 phase (blue circles). Dashed line: flavour-wave prediction (Toth et al [11]; (b) Estimates of the quadrupole order parameter Q in the AFQ3 phase.

results for this order parameter (not shown) are not sufficiently accurate to confirm this, but are consistent with the magnetization vanishing with exponent ½ at $\theta = 45^0$., as would be predicted by spin-wave/flavour-wave theory.

4. Summary and Conclusions

Our series results are in excellent agreement with the phase diagram suggested by Toth *et al* [11] for this model. The nature of the phase transitions between the different phases requires further exploration.

Acknowledgments

We are grateful for the computing resources provided by the Australian Partnership for Advanced Computing (APAC) National Facility.

References

[1] Blume M. and Hsieh Y.Y., 1969. J. Appl. Phys. **40**, 4267.
[2] Chen H. H. and Levy P. M., 1973. *Phys. Rev.* **B7**, 4267.
[3] Papanicolaou N., 1988. *Nucl. Phys*. **303**, 367.
[4] Nakatsuji S., *et al*, 2003. *Science* **309**, 1697.
[5] Tsunetsugu H. and Arikawa M., 2006. *J. Phys. Soc. Japan* 75, 083701.
[6] Lauchli A., Mila F. and Penc K., 2006. *Phys. Rev. Lett*. **97**, 087205.
[7] Bhattacharjee S., Sheny V. B. and Senthil T., 2006. *Phys. Rev*. **B74**, 092406.
[8] Stanek D., Sushkov O.P. and Uhrig G.S., 2011. *Phys. Rev*. **B84**, 064505.
[9] Harada K. and Kawashima N., 2001. *J. Phys. Soc. Japan* **70**, 13.
[10] Harada K. and Kawashima N., 2002. *Phys. Rev*. B65, 052403.
[11] Toth T. A., Lauchli A. M., Mila F. and Penc K., 2012. *Phys. Rev*. **B85**, 140403 (R).
[12] Oitmaa J., Hamer C. J. and Zheng W-H., 2006. *'Series Expansion Methods for Strongly Interacting Lattice Models'* (Cambridge University Press)
[13] Oitmaa J. and Hamer C. J., 2008. *Phys. Rev*. **B77**, 224435.

PROCEEDINGS - 37th ANNUAL CONDENSED MATTER AND MATERIALS MEETING, 5 - 8 February, 2013. Wagga Wagga, NSW, Australia

Asymmetric Magnetization Reversal from a Cluster/Spin Glass Model

L.C. Barnsley[a], E.MacA. Gray[a] and C.J. Webb[a]

[a] *Queensland Micro- and Nanotechnology Centre, Griffith University, Queensland 4111, Australia.*

A modified Stoner-Wohlfarth model to describe an ensemble of ferromagnetic clusters interacting with a quasi-isotropic spin glass was developed to account for asymmetric reversal in concentrated spin glass systems. The model used a Gaussian distribution of cluster easy axes orientations, which successfully simulated magnetic hysteresis loops exhibited by two concentrated CuMn alloys. Physically plausible scenarios for the dependences of model parameters on cooling field were extracted.

1. Introduction

The exchange bias effect conventionally occurs in systems with an interface between ferromagnetic (FM) and antiferromagnetic (AFM) components due to an exchange interaction with unidirectional anisotropy, and manifests as shifted magnetic hysteresis loops when the system is cooled in field below the AFM Néel temperature, T_N [1]. Spin glass systems exhibit both positive and negative exchange without magnetic long-range order. Spin glasses display a cusp in the temperature dependent magnetization at the glass temperature, T_g, and unusual behaviour at lower temperatures that is understood in terms of magnetic clusters and a frozen, magnetically frustrated component of magnetization [2]. In recent years, there has been increasing recognition of the analogues between exchange bias systems and spin glasses [3], such as shifted hysteresis loops, training effects and asymmetric reversal. These analogues are even more apparent in concentrated, mictomagnetic spin glasses, where the behaviour is understood in terms of FM clusters interacting with disordered, mostly AFM clusters [2].

Asymmetric reversal was first recognized in Fe/FeF_2 exchange biased multilayers [4], but was observed in mictomagnetic CuMn before then [5]. Asymmetric reversal is defined in general either as an asymmetry between the magnetization reversal mechanisms from positive to negative saturation and the reversal mechanisms in the other direction, or as an asymmetry of the *M-H* curve with respect to the field axis [6]. Modified Stoner-Wohlfarth models have been used to account for asymmetric reversal in multilayer systems by allowing the layer easy axes to misalign with the applied field, H [7-9]. In this paper, a Stoner-Wohlfarth model is adopted and extended to describe magnetic clusters interacting with a disordered, quasi-isotropic spin glass component. This model is used to successfully account for the cooling field dependence of two mictomagnetic CuMn samples.

2. Model and method

Hysteresis loops measured on spin glass systems at low temperature tend to linear dependence on H at high fields with a strong non-linear response in the region where switching of the magnetization occurs. Concentrated spin glasses exhibit hysteresis loops with asymmetric reversal after cooling in field. In CuMn, this typically takes the form of a sharp, high curvature transition on the positive side of the hysteresis loop, and a low curvature, gradual decrease in magnetization on the negative side of the step, typically the signature of a coherent rotation of magnetic moments [5,10].

Monte Carlo simulations involving an ensemble of ferromagnetically aligned clusters that each have a unique easy axis and experience a molecular field due to exchange interactions with the local spin glass, were run to fit the non-linear component of hysteresis

loops where noticeable asymmetric reversal was observed. The linear component was fitted in the high field region to extract a value for the high-field susceptibility, $\chi_{H\rightarrow H\max}$ and the linear component was then subtracted from the loop, leaving the non-linear component.

The total cluster energy was expressed using a modified Stoner-Wohlfarth model [7,11] to sum the Zeeman energy, shape (uniaxial) anisotropy energy and exchange (unidirectional) anisotropy energy due to the cluster's interaction with the local spin glass:

$$E(\theta) = -\mu_{\text{eff}}\mu_0 H\cos\theta + KV\sin^2(\phi-\theta) - JV\cos(\alpha-\theta). \quad (1)$$

Here, θ is the angle between the applied field and the alignment of the cluster moment, μ_{eff} is the magnitude of the effective cluster moment, K is the uniaxial cluster anisotropy energy per unit volume, ϕ gives the direction of the cluster easy axis with respect to the applied field, J is the total energy per unit volume of all exchange interactions between the cluster and the local spin glass moments, α is the angle between the applied field and the effective molecular field experienced by the cluster owing to the local spin glass and V is the volume of the cluster.

The probability of a cluster moment having an alignment θ is given by a Boltzmann distribution over all angles between 0 and 180º. After N Monte-Carlo trials, the resultant normalized magnetization was obtained by averaging the projections corresponding to the trial θ values on the measuring axis (parallel to the field axis).

Assumptions about cluster composition were avoided by using parameters KV, the uniaxial anisotropy energy per cluster and JV, the exchange interaction energy per cluster, instead of K, J and V. Given the large number of interdependent variables, physically reasonable values can only be extracted if assumptions are made about one or more of the parameters. These assumptions differ between samples, however three particular assumptions relevant to the cases of concentrated spin glasses are discussed here.

Firstly, asymmetric reversal was accounted for by allowing the easy axes to deviate from the direction of the cooling field, H_{FC} so that $0 \leq \phi \leq 180º$. The distribution of ϕ was considered to result from freezing of a paramagnetic ensemble cooled in H_{FC}, and was found to be fairly well approximated by a Gaussian in ϕ. A Gaussian distribution for easy axes, with a mean value of 0º and normalized probability over 180º, was adopted for simplicity. This model successfully accounted for hysteresis loops from two concentrated CuMn samples (section 3). The parameter ϕ then becomes ϕ_{stdev}, the standard deviation of this distribution.

Secondly, it was assumed for simplicity that the clusters are mostly internally ferromagnetic in alignment, and interact only with a frozen "spin glass" component but not with each other. The spin glass component was modelled as quasi-isotropic by allowing α to take random orientations between 0 and 180º. Finally, when the observed exchange bias fields were negative, positive values for J were assumed.

3. Results and simulations

Fig. 1 shows the effect changing parameters μ_{eff}, J, K and ϕ_{stdev} has on simulated M-H loops, assuming V to be proportional to μ_{eff}. Increasing the effective cluster size increases the curvature of the loop around the step, while increasing J shifts the loop along the field axis in the negative direction. Increasing K while pinning the cluster easy axis to align with the field also has the effect of increasing the curvature of the loop, but once the variable reaches appreciable values, of the order of 1×10^5 J/m^3, the model becomes relatively insensitive to even large changes in K. However, once ϕ is allowed to deviate from the field axis, changes in K have a drastic effect on the asymmetry of the simulated loops.

Fig. 2 demonstrates how the model can be used to parameterize low temperature magnetic hysteresis loops in an investigation of the cooling field dependence of two CuMn alloys, one prepared via aging at 348 K (Sample A) [10] and the other via neutron irradiation

(Sample I) [12]. The model was used to fit the first "up" branch of minor hysteresis loops measured between ±477 kA/m at 5 K after cooling in various fields between 7 and 637 kA/m.

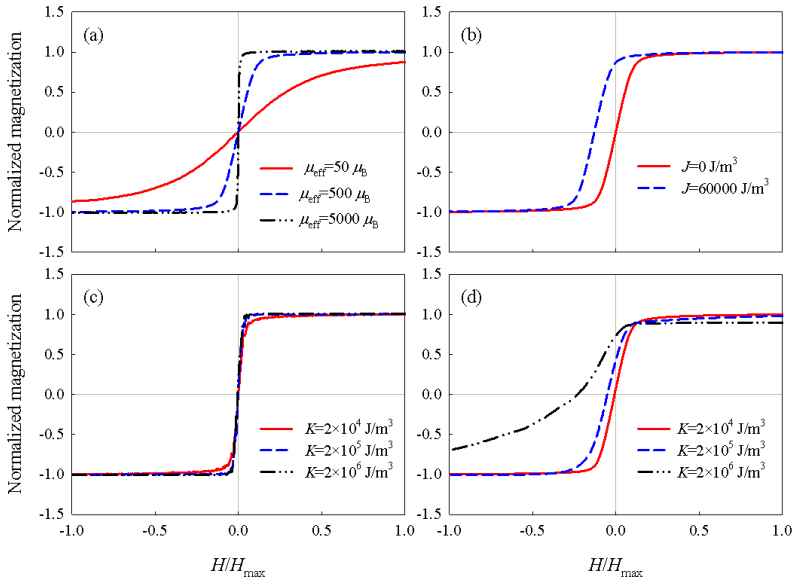

Fig. 1. Simulated *M*-*H* curves, demonstrating the effects of changing (a) μ_{eff}, (b) *J*, (c) *K* with $\phi_{stdev} = 0^o$, (d) *K* with $\phi_{stdev} = 30^o$.

The values for μ_{eff} extracted from Sample I in Fig. 2(a) suggest a decrease in the cluster moment above $H_{FC} \geq 80$ kA/m, coinciding with the suppression of asymmetric reversal by high cooling fields. This is interpreted as evidence for the fragmentation of clusters into multi-domain particles with high H_{FC}. In comparison, μ_{eff} for Sample A increases monotonically with cooling field.

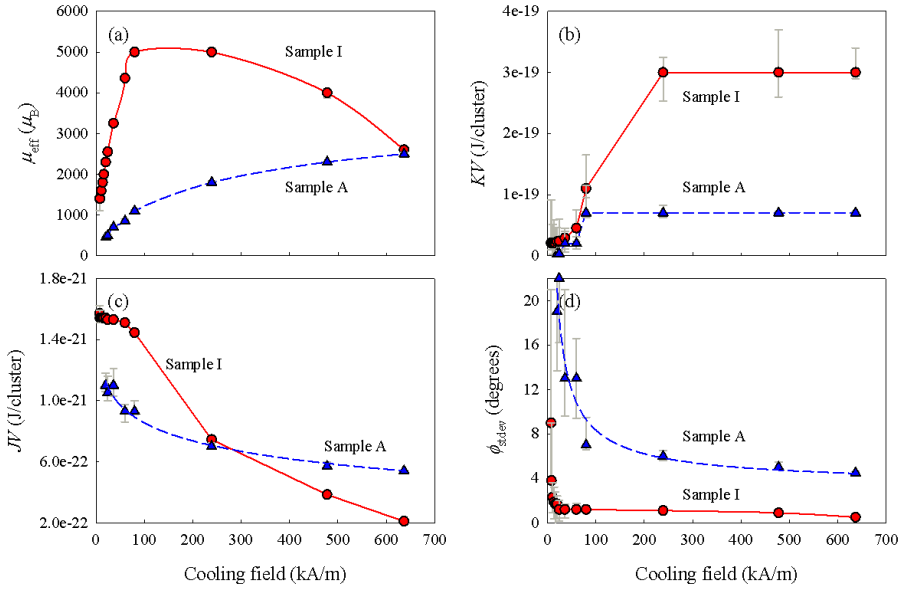

Fig. 2. The model was used to parameterize minor hysteresis loops of two CuMn samples measured between ±477 kA/m at 5 K after cooling in various fields. Parameters (a) μ_{eff}, (b) *KV*, (c) *JV* and (d) ϕ_{stdev} are displayed as functions of the cooling field.

For both systems, *KV* appears to saturate at higher cooling fields ($H_{FC} \geq 80$ kA/m for Sample I and $H_{FC} \geq 240$ kA/m for Sample A). The uniaxial anisotropy energy per cluster is

significantly larger in Sample I than it is in Sample A, even at $H_{FC} = 637$ kA/m, where the effective cluster moments are comparable. The large uncertainty attached to this parameter is due to the model's relative insensitivity to K when K is high and ϕ_{stdev} is low, but the behaviour seen in Fig. 2(b) may also be reconciled with the ramified nature of magnetic clusters in CuMn, as determined by small angle neutron scattering (SANS) [13], in that uniaxial anisotropy may saturate at a certain cluster size [10].

JV for Sample I decreases slowly in the low to moderate cooling field range, before decreasing rapidly once $H_{FC} > 80$ kA/m. In this cooling field range, JV falls with $H_{FC}^{-0.87}$. This decrease in unidirectional anisotropy with H_{FC} is seen as qualitatively consistent with the domain state model for exchange bias, in that it's enhanced by disorder and pinning of domain walls in the AFM (or analogously, "spin glass") component of an exchange bias system [14].

Clusters in Sample I are considerably susceptible to alignment by the cooling field, with ϕ_{stdev} rapidly decreasing to less than 2° once $H_{FC} \geq 24$ kA/m. This, along with the behaviour of μ_{eff}, demonstrates the significantly more ferromagnetic character induced in Sample I by the irradiation process [12], compared with Sample A.

4. Conclusion

A modified Stoner-Wohlfarth model based on an interaction between ferromagnetic clusters and a quasi-isotropic spin glass component was successfully used to parameterize hysteresis loops from two mictomagnetic CuMn samples that exhibit intrinsic exchange bias at temperatures well below T_g. Asymmetric reversal in these hysteresis loops was successfully accounted for using a Gaussian distribution of cluster easy axes, and the resultant scenarios for the dependences of parameters on cooling field were considered as physically plausible. The scenarios explored using the model could be verified with experimental techniques that probe magnetic clusters, particularly SANS.

Acknowledgments

LCB acknowledges receipt of an Australian Postgraduate Award. The research was supported by a grant from the Australian Research Council, grant number R19800120.

References

[1] Meiklejohn W H and Bean C P 1956 *Phys. Rev.* **102** 1413
[2] Beck P A 1972 *J. Less-Common Met.* **28** 193
[3] Ali M, Adie P, Marrows C H, Greig D, Hickey B J and Stamps R L 2007 *Nature Mater.* **6** 70
[4] Fitzsimmons M R, Yashar P, Leighton C, Schuller I K, Nogués J, Majkrzak C F and Dura J A 2000 *Phys. Rev. Lett.* **84** 3986
[5] Mukhopadhyay A and Beck P A 1975 *Solid State Commun.* **16** 1067
[6] Li Z P, Petracic O, Morales R, Olamit J, Batlle X, Liu K and Schuller I K 2006 *Phys. Rev. Lett.* **96** 217205
[7] Camarero J, Sort J, Hoffmann A, Garcia-Martin J M, Dieny B, Miranda R and Nogués J 2002 *Phys. Rev. Lett.* **95** 057204
[8] Chen J, Jin G and Ma Y Q 2007 *J. Phys.: Condens. Matter* **19** 236225
[9] Iglesias O, Batlle X and Labarta A 2007 *J. Magn. Magn. Mater.* **316** 140
[10] Barnsley L C, Gray E M and Webb C J 2013 *J. Phys.: Condens. Matter* **25** 086003
[11] Stoner E C and Wohlfarth E P 1948 *Phil. Trans. R. Soc. Lond. A* **240** 599
[12] Gray E M 1996 *J. Phys.: Condens. Matter* **8** 751
[13] Gray E M, Hicks T J and Smith J H 1982 *J. Phys. F: Met. Phys.* **12** L189
[14] Nowak U, Misra A and Usadel K D 2001 *J. Appl. Phys.* **89** 7269

Biomimetic Structure Design from Wood with Epoxy–Silica Composites

N. Daud[a,b] and R.A. Shanks[a]

[a] *School of Applied Sciences, RMIT University, Melbourne, VIC 3000, Australia.*
[b] *Chem. Dept., Fac. Sc. & Maths, UPSI, 35900 Tg Malim, Perak, Malaysia.*

The cellular structure of wood was replicated with sol-gel silica and the structure was strengthened by epoxy resin impregnation. This was achieved by oxidative alkaline extraction of non-fibre components from a pinewood template. A porous silica skeleton was obtained after calcining at 500 °C and this cellular structure was maintained as an epoxy-silica composite, replicating the cellular morphology of the wood.

1. Introduction

Biomimetic supramolecular structure design based on natural structural materials, such as wood, imparts high integrity and repetition from the template wood due to hierarchical morphology. Wood is a natural fibre composite that is structured on several levels of hierarchy. Wood tissues are made of interconnected cells with open spaces (lumens). At the micrometer scale, wood has a cellular architecture resembling a honeycomb structure. The nanoscale structure of wood is characterised by the molecular cellulose fibres and membrane structures of cell walls. The cell walls are composed of cellulose microfibrils embedded into matrix of hemicelluloses and lignin [1].

Replication of a biological template into an inorganic structural material, known as biomorphic or biomimetic mineralization, provides a powerful tool to create complex material structures [2-4]. Wood has been widely used as a natural template for manufacturing porous ceramics with cellular morphology, usually by liquid infiltration of carbonised wood with liquid reactant and subsequent sintering in inert atmosphere. Examples are carbide ceramics like SiC [5-7], oxide ceramics like SiO_2 [8], Al_2O_3 [9] and TiO_2 [10] and ceramic composite like Si–SiC, SiC–Si [11] and TiC–C [12].

In nature, per-mineralisation and petrification of wood by mineral solution, such as silicates, are well known. Silica replicas of wood structure can be obtained by infiltration with Si-containing sols, which decompose into SiO_2 during subsequent heat treatment (calcination) in air. In earlier attempts to artificially 'silicify' wood, the template was soaked in water glass (sodium silicate). However, the silicate minerals were found located mainly in the lumina of the wood cells and the structure of the gels were not stable and easily collapse once the organic part was removed [13-14]. Therefore, to improve the properties of the silica–wood composites, the inorganic silicates must be incorporated onto and within the cell walls. Previous studies showed that the sol-gel process was effective to impregnate wooden materials [2,15-16]. Bound water in the cell wall was used to direct the sol-gel process as to achieve a deposition of the silicate within the walls. The degree of crosslinking of the polysiloxanes and the depth of the penetration were influenced by the concentration of silicon alkoxide in ethanol and by other parameters such as reaction time.

The aim was to replicate wood morphology in a composite containing synthetic materials that will retain the structure or cellulose framework while removing other components. In this study, a wood template was vacuum impregnated with tetraethyl orthosilicate (TEOS) via a sol-gel process, without catalyst, to allow sufficient time for the sol to penetrate deep into the cell walls. The challenge was to maintain the wood structure after removing the fibre cellulose from the composite during calcination. Subsequently, the silica skeleton needed to be strong enough to maintain its cellular structure during epoxy resin impregnation.

2. Experimental

Pinewood (*Pinus Radiata*) was cut in dimensions of 40 mm x 20 mm x 5 mm (radial x tangential x longitudinal) and washed by extraction with toluene–ethanol solution in the volume ratio 2:1 and then with the same amount of pure ethanol for 6 h each using a Soxhlet extraction apparatus. The extracted wood were delignified with sodium chlorite (4.2 g) and acetic acid (1.5 g) in water (69.3 g) at 70 °C. Delignification solutions were renewed after 3 h and the templates treated for another 3 h. Following the treatment, the templates were extracted with ethanol to remove the residual treatment solution and were stored in ethanol until required. This was to avoid collapse and warping of the structure due to drying effects. Silica–wood templates were prepared by the sol-gel process with, TEOS (4.7 g), ethanol (17.4 g) and water (7.0 g) using vacuum–pressure impregnation technique. The templates were immersed in sol solution for 24 h before drying in an oven at 50 °C (24 h) and 105 °C (5 h). The silica-wood template was calcined at 500 °C for 2 h to produce a silica skeleton with a cellular structure mimicking the structure of wood. Epoxy–silica composite was prepared through infiltration of silica skeleton with epoxy resin using vacuum–pressure impregnation technique. The composite was cured at room temperature for 3 d and post cured at 100 °C (3 h) and 150 °C (3 h).

Specimens were transferred onto a sample holder covered with conductive carbon tape and sputter coated with carbon for scanning electron microscopy (SEM) analysis (FEI Quanta 200 ESEM) coupled with energy dispersive X-ray spectrometer (SEM-EDX) to study its morphology and distribution of silica in composites. The images taken from SEM micrographs were used to determine the cell wall thickness and the size of the cells.

3. Results and Discussion

The infiltration of silica sol into the wood was done by a vacuum–pressure impregnation technique to increase the penetration depth of silica into the wood templates [15]. The template was infiltrated with an anhydrous mixture of ethanol and TEOS, without acid or base catalyst to reduce the hydrolysis rate. The effectiveness of this method could be observed by the stability of the sol solution, which stayed clear during the impregnation process. If the TEOS was hydrolysed and condensed before penetrating the cell wall, its oligomeric units would not have been able to enter the interstitial space [2]. The hydrolysis, condensation reactions and formation of inorganic gels are as shown in the equation (1) and (2) below.

$$Si(OEt)_4 + 4H_2O \rightarrow Si(OH)_4 + 4EtOH \quad (1)$$

$$2Si(OH)_4 \rightarrow Si(OH)_3 - O - Si(OH)_3 + H_2O \rightarrow (SiO_2)_n + nH_2O \quad (2)$$

SEM micrographs of the silica infiltrated and calcined (silica skeleton) templates are shown in Fig. 1 and Fig. 2 respectively. The average of cell size and wall thickness are summarised in Table 1. The thickness of the cell walls of cellulose template increased from 5.2 ± 1.6 μm to 6.2 ± 0.8 μm after infiltration with TEOS. The cell walls were coated with silica and SEM-EDX observation revealed the presence of SiO_2 in these templates. The Si-Kα X-ray mapping clearly showed the silica was homogeneously deposited within the cell walls (Fig. 3). This result confirms the good penetration of the TEOS solution, hence the success of the sol composition.

A silica template with a cellular structure replicating the structure of wood was prepared by calcining the silica-cellulose frame. The organic component was removed by calcining at 500 °C producing a porous biomorphic silica skeleton with wall thickness of 3.0 ± 0.3 μm. SEM micrograph (Fig. 2) shows the high quality of cellular microstructure replication

achieved in silica with a small reducing in cell size (17.5 %). Deep penetrating of sol solution into the cell walls clearly aiding in the perfect replicating of wood structure.

Table 1. Average cell size and cell wall thickness.

Sample	Cell size (μm^2)	Wall thickness (μm)
Cellulose-SiO_2	699 ± 64	6.2 ± 0.8
SiO_2 skeleton	576 ± 68	3.0 ± 0.3

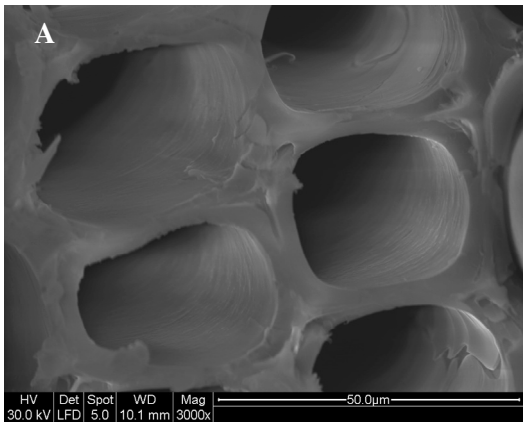

Fig. 1. Scanning electron micrograph of silica-cellulose template

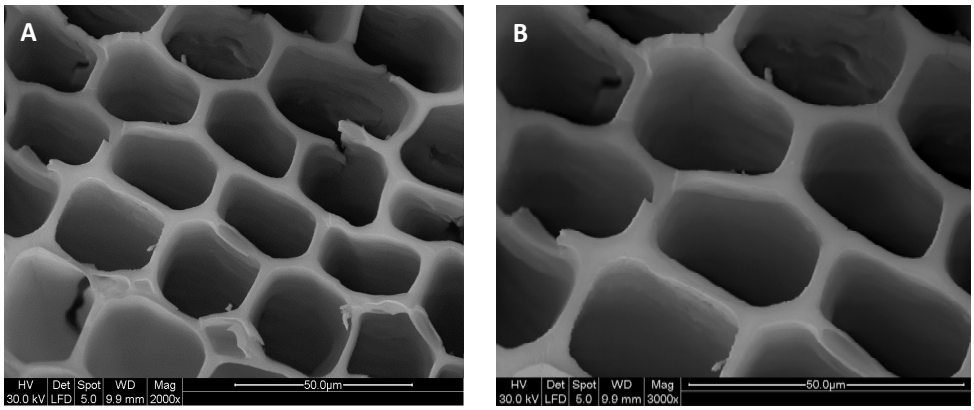

Fig. 2. Scanning electron micrograph of silica skeleton at magnification of (A) 2000x and (B) 3000x.

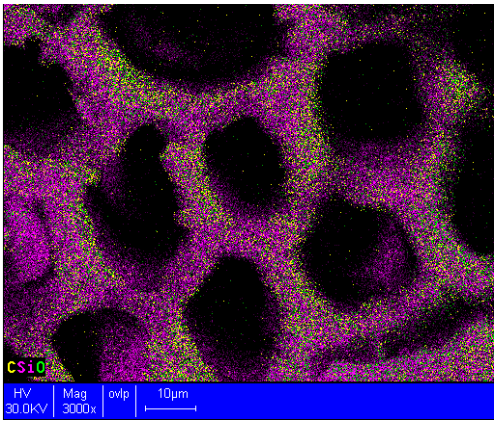

Fig. 3. SEM-EDX micrograph of silica-cellulose template.

Epoxy composites containing a silica frame, which mimic the cellular structure of wood were prepared through impregnation of silica skeleton with an epoxy resin. The fragile frame was strengthened by the epoxy resin which filled the empty lumens (Fig. 4). The impregnation with epoxy resin slightly distorted the otherwise perfect cellular structure of silica skeleton. The silica frame in the epoxy–silica composite can be seen clearly using SEM-EDX, as shown in Fig. 5.

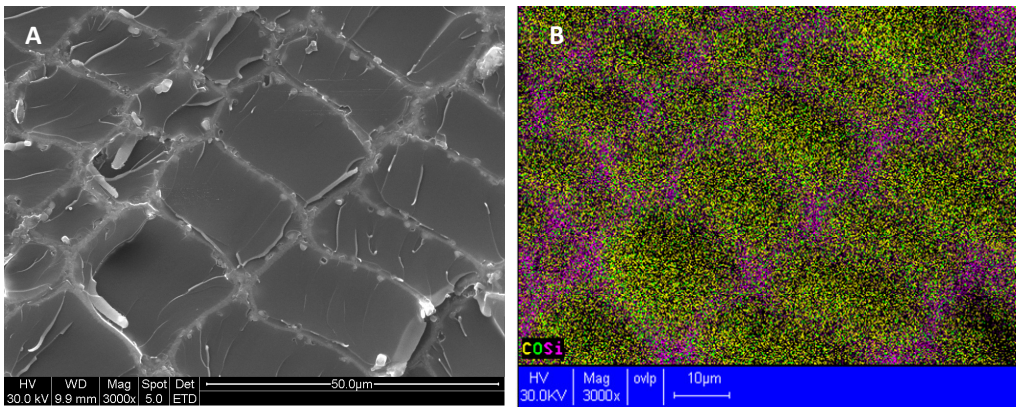

Fig. 4. Scanning electron micrograph of epoxy-silica composite and its C-O-Si-Kα X-ray map at 3000x.

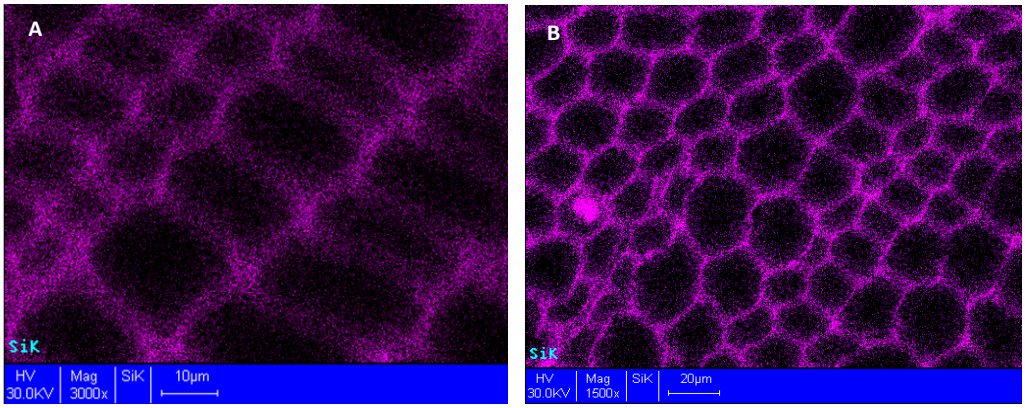

Fig. 5. SEM-EDX images of Si-Kα X-ray map at magnification of (A) 3000x and (B) 1500x.

4. Conclusion

A high quality of cellular microstructure replication of wood was achieved either with retention of the cellulose fibre skeleton or with a completely synthetic silica replica. Infiltration with epoxy resin and subsequent curing formed composite retaining the cellular structure of wood. Minimal distortion of the original wood cells occurred in the epoxy composite derived from the replicas. The techniques described demonstrate biomimetic preparations of semi-synthetic and synthetic composites based on wood that retain the morphology of the wood.

Acknowledgments

The authors would like to acknowledge the facilities, the scientific and technical assistance of the Australian Microscopy and Microanalysis Research Facility at the RMIT Microscopy and Microanalysis Facility, RMIT University.

References

[1] Fengel D and Weneger G 1984 *Wood* (Berlin, New York: Walter de Gruyter).

[2] Van Opdenbosch D 2011 *J. Mater. Res.* **26** 1193.
[3] Fan T, Chow S and Zhang D 2009 *Prog. Mater. Sc.* **54** 542.
[4] Daud N, Shanks R A, and Kong I 2012 *World J. Eng.*, **9** 385.
[5] Greil P, Lifka T and Kaindl A 1998 *J. Eur. Ceram. Soc.* **18** 1961.
[6] Ota T, Takahashi M, Hibi T, Ozawa M, Suzuki S and Hikichi Y 1995 *J. Am. Ceram. Soc.* **78** 3409.
[7] Singh M and Salem J A 2002 *J. Eur. Ceram. Soc.* **22** 2709.
[8] Yongsoon S, Jun L, Jeong H C, Zimin N and Exarhos G J 2001 *Adv. Mater.* **13** 728.
[9] Cao J, Rambo C R and Sieber H 2004 *J Porous Mater.* 2004 **11** 163.
[10] Cao J, Rusina O and Sieber H 2004 *Ceram. Int.* **30** 1971.
[11] Sun B, Fan T, Zhang D and Okabe T 2005 *J. Adv. Mater.* **37** 76.
[12] Sun B, Fan T, Zhang D and Okabe T 2004 *Carbon* **42** 177.
[13] Drum R W 1968 *Science* **161** 175.
[14] Furuno T and Immura Y 1998 *Wood Sc. Tech.* **32** 161.
[15] Gotze J, Mockel R, Langhof N, hengst M and Klinger M 2008 *Ceramics* **52** 268.
[16] Saka S and Ueno T 1997 *Wood Sc. Tech.* **31** 457.

Poly(trimethylene terephthalate) Block Co-polymer with Epoxy Resin: Preparation, Characterization and Properties

Sarath Chandran[a,b,c], S. Thomas[a,b], R. A. Shanks[c]

[a] *School of Chemical Science, Mahatma Gandhi University, Kottayam, Kerala, India 686560.*
[b] *Centre for Nanoscience and Nanotechnology, Mahatma Gandhi University, Kottayam, Kerala, India 686560.*
[c] *School of Applied Sciences, RMIT University, Melbourne, Australia.*

Processing of thermoplastics can be facilitated by plasticizer, though after processing the plasticizer remains to modify the properties of the product. Investigation of the plasticizing action of diglycidyl ether of bisphenol-A (DGEBA) epoxy resin for poly(trimethylene terephthalate) (PTT) using Fourier transform infrared spectroscopy, Raman spectroscopy and differential scanning calorimetry led to the introduction of a novel block co-polymer (DGEBA-*block*-PTT-*block*-DGEBA). The novel block co-polymer, formed by the reaction between the end groups of PTT and the oxirane ring of DGEBA, was dependent on the pH of the medium.

1. Introduction

Poly(trimethylene terephthalate) (PTT), first synthesized and patented in 1941 [1], remained obscure till recent times due to the high cost of production. Recent discovery of bioengineering route to synthesize 1, 3-propanediol [2] [3], has rekindled the scientific interest in this polymer. The unique zig-zag structure of PTT renders it a stretch recovery which is about 2-3 times greater than polyamides and other polyesters [4]. The use of epoxy resin as a modifier for PTT based blends has been tried by different researchers [5], [6] but the mechanism of modification was not addressed in these studies. The main aim here was to investigate how the addition of diglycidyl ether of bisphenol-A (DGEBA) epoxy resin affect the melting properties, glass transition temperature of PTT and the mechanism for plasticizing action of DGEBA which remained unattended is explained here.

2. Experimental

2.1 Materials used

DGEBA epoxy resin (Lapox L-12) with an epoxy equivalent between 5.25-5.40 $eq \cdot kg^{-1}$ and viscosity between 1.15-1.20 $g \cdot cm^{-3}$ was procured from Atul Industries, India. Poly(trimethylene terephthalate) (PTT or SORONA 3G) with a density between 1.3-1.5 $g \cdot cm^{-3}$, M_n of 22,500 $g \cdot mol^{-1}$ and degree of polymerization of 2.5 was kindly supplied by DuPont Industries USA. Details of the materials used are given in Table 1and their chemical structures are given in Figure 1. All \materials were used without further purification.

Table 1. Characteristics of PTT, DGEBA and DDS

	Poly(trimethylene terephthalate)	Diglycidyl ether of bisphenol-A	Diammino diphenyl sulfone
M_w [(a)] (g· mol^{-1})	58,400	-	-
M_n [(a)] (g· mol^{-1})	22,500	-	-
Viscosity [(b)] (g·cm^{-3})	-	1.15-1.2	-
Epoxy content [(b)] (equ·kg^{-1})	-	5.25- 5.40	-
T_g [(c)] (°C)	54	-16	-
T_m [(d)] (°C)	227	-	150
ΔH_{ref} [(e)] (J· g^{-1})	146	-	-
Supplier	DuPont Industries, USA.	Atul Industries, Gujarat, India.	Atul Industries, Gujarat, India.

(a) Molar mass estimated by gel permeation chromatography (Perkin-Elmer). Polystyrenes with low polydispersity were used as standards.
(b) Information provided by the supplier.
(c) Glass transition temperature as determined by DSC.
(d) Apparent melting temperature for the neat polymer during a first heating scan.
(e) The melting enthalpy of PTT crystals [7].

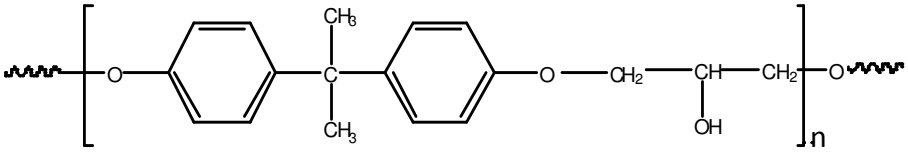

Diglicidyl ether of bisphenol-A

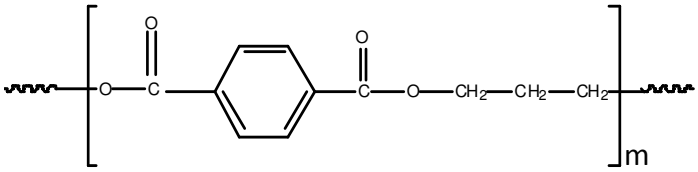

Poly(trimethylene terephthalate) (n≠ m)

Figure 1: Chemical structure of DEGEBA and PTT.

2.2 Blend preparation

PTT with varying amounts of DGEBA (5, 10, 20, 30 %·w/w) were prepared by using a Haake mixer. The blends were heated to 240 °C for 900 s with constant shearing at 80 rpm. After mixing the blends were removed and used for the study.

3. Equipment

3.1. *Differential Scanning Calorimetry*

Perkin-Elmer DSC7 (Shelton, CT, US), calibrated for temperature with indium and zinc standards, and for enthalpy with indium, was used for the analysis of the blends under a

nitrogen atmosphere. A new sample was used for each DSC experiment. The samples were exposed to different thermal histories:

3. 1. (A) Glass transition temperature determination.

Blends prepared were annealed at T_a =260 °C for 1 min, followed by cooling at a rate of 100 K·min^{-1} to -50 °C and held for 1 min The samples were then reheated 260 °C at a rate of 10 K·min^{-1}.

3.1. (B) Samples were annealed at T_a= 260 °C for 1 min followed by cooling at a rate of 20 K·min^{-1} to the T_c of 205 °C and held until crystallization was complete. The half-time of crystallization was determined at T_c = constant. The same procedure was applied for the determination of the melting temperature. After crystallization sample was heated to 260 °C at a rate of 10 K·min^{-1}.

3.2 ***Infrared Spectroscopy Analysis***

Fourier transform infrared (FTIR) spectroscopic studies were performed on neat polymers and the blends using attenuated total reflection (ATR) using Perkin-Elmer Spectrum One Spectrometer (Lanstrisant UK). FTIR spectra were recorded in transmittance mode over the range of 4000- 600 cm^{-1} by an averaging 16 scans at a resolution of 4 cm^{-1} in all cases.

3. 3. ***Raman spectroscopy analysis***

Raman spectroscopy analysis was performed on neat PTT and the blends using Perkin-Elmer Raman Station 400F Raman spectrometer.

4. Results and Discussion

Miscibility studies using modulated temperature DSC (MTDSC) shows that as the amount of DGEBA in the blends increases the glass transition temperature (T_g) decreases. Experimentally observed T_g values were fitted with the Fox equation and it shows that the blend exhibit a negative deviation from a Fox equation fitting. The experimentally observed T_g values and the Fox equation fitting results are shown in Figure 2.

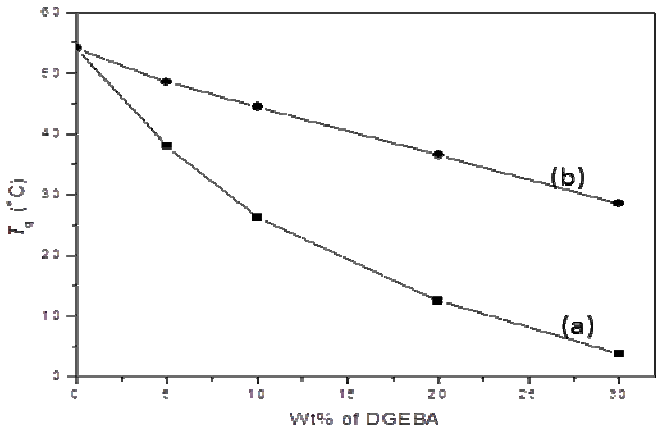

Figure 2: Plot of T_g against DGEBA concentration for PTT-DGEBA blends, (a) represents the experimentally observed values and (b) represents the Fox equation fitting.

The equilibrium melting temperature ($T°_m$) determined by using Hoffman-Weeks equation shows a regular decrease as the amount of DGEBA in the blends increases indicating that DGEBA can act as a plasticizer. The results of Hoffman-Weeks fitting are tabulated in Table 2.

Table 2: $T°_m$ and correlation coefficient (r) for T_m versus T_c relationship in the T_c range of 185-205 °C for PTT-DGEBA blends.

Blend composition	$T°_m$ /°C	α	r
100:0	229.0	0.060	0.899
95:5	227.7	0.043	0.899
90:10	225.5	0.024	0.968
80:20	221.8	0.023	0.999
70:30	221.0	0.035	0.996

The $T°_m$ values decreaseed as the amount of DGEBA increased in the blends. Analysis of the epoxy networks using FTIR spectroscopy is widely followed by researchers and the peak at 915 cm^{-1} is characterized as that of the oxirane ring [8], [9]. In the case of PTT-DGEBA blends it was observed that the peak at 915 cm^{-1} disappeared completely indicating the possibility of chemical reaction between the hydroxyl and carboxylic acid end groups of PTT and the epoxy group of DGEBA. The experimentally observed FTIR spectrum is shown in Figure 3.

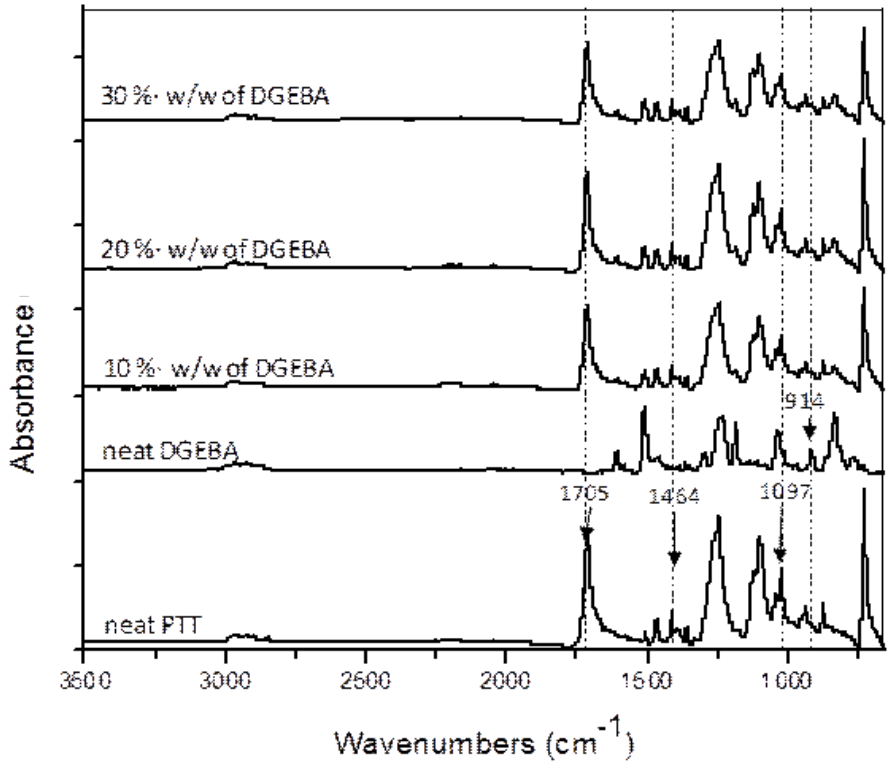

Figure 4: FTIR spectra of the blends, dotted lines represent the areas of interest.

The peak at 1464 cm^{-1} is assigned to gauche $–CH_2$ group of the crystalline region [10] indicating that the PTT retains its crystallinity in the blends. This possibility of chemical reaction between the end groups of PTT and DGEBA was further confirmed by Raman spectroscopy. Raman spectroscopy is more sensitive to polarizable bonds and less sensitive to polar bonds [11]. Epoxy ring produces two intense peaks at 846 cm^{-1}(epoxy deformation) and at 1259 cm^{-1} (in-plane deformation of the epoxy ring) [11]. The peak at 1259 cm^{-1} corresponds to the breathing mode of benzene rings and so the peak at 846 cm^{-1} is to be considered as the

presence of un-reacted epoxy groups. Raman spectroscopy results show that the peak at 846 cm^{-1} disappear completely confirming a chemical reaction between the end-groups of DGEBA and PTT.

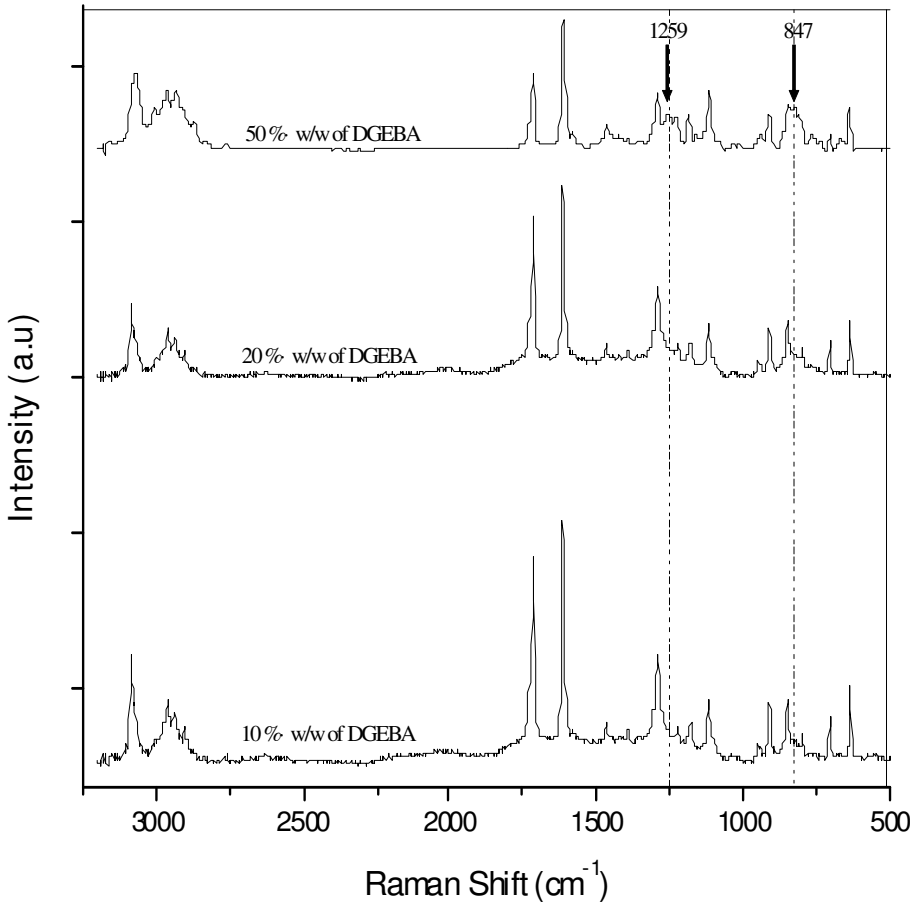

Figure 5: Raman spectroscopy results for PTT-DGEBA block co-polymers.

This shows that when the amount of DGEBA was between 0-30 %·w/w the pH of the medium induced a chemical reaction between the end groups of PTT and DGEBA. The nucleophiles (hydroxyl and carboxylic acid) at the ends of PTT attack the oxirane ring of DGEBA leading to it ring opening. This reaction leads to the formation of a block co-polymer (DGEBA-*block*-PTT-*block*-DGEBA). Further characterization of this novel block co-polymer by NMR spectroscopy was not successful due to practical difficulties.

5. Conclusion

A chemical reaction between the end groups of DGEBA and PTT was followed by using FTIR spectroscopy and Raman spectroscopy. Results showed that a chemical reaction occurred between the terminal hydroxyl and carboxylic acid end group of PTT and the oxirane ring of DGEBA. This chemical reaction was found to be highly sensitive to the amount of DGEBA which in turn can be correlated to the pH of the medium because when the amount of DGEBA was $\geq$ 40 %·w/w no ring opening reaction was observed. A steady decrease in the T_g as observed in the MTDSC studies shows that the block co-polymer formed follow a negative deviation from the Fox equation fitting. The steady decrease in the T_m° value indicate that DGEBA can act as a plasticizer for PTT. This result has been reported earlier by different researchers. The FTIR and Raman spectroscopy analysis shows that the plasticizing action of DGEBA is due to the formation of a block co-polymer. This novel block co-polymer (DGEBA-*block*-PTT-*block*-DGEBA) can find use in a variety of fields.

Acknowledgement
The authors thank: (1) Prof. H. W. Kammer and Senior Lecturer Dr. C. H. Chan, Universiti Teknologi MARA, Shah Alam, Malaysia for their contributions, (2) Frank Antolasic, Dr. Muthu P, Dr. Selvakannan, and Michael Czjaka, RMIT University, for their active support. (3) DuPont industries for providing SORONA 3G, (4) Aeronautic Research and Development Board, India and RMIT University, Melbourne for providing the financial support.

References
[1] Whinfield and Dickson. Improvements Relating to the Manufacture of Highly Polymeric Substances, British Patent 578,079, 1941; Polymeric Linear Terephthalic Esters, U.S. Patent 2,465,319, 1949.
[2] Broun P J, Blake M S, Richard W P, Cleve E D, Pedro A J. Process for preparing 1,3-propanediol; US 5770776, 1998. http://www.patentbuddy.com/Patent/5770776.
[3] Haas T, Jaeger B, Weber R, Mitchell S F, King C F. Appl. Catal. A-Gen. 2005; 280(1) 83 - 88.
[4] Wang B, Christopher Y L, Hanzlicek J, Stephen Z D C, Geil P H, Grebowicz J, Ho R M, Polymer 2001; 41: 7171-7180.
[5] Xue M L, Yu Y L, Chuah H H, Rhee J M, Kim N H, Lee J H. European Polymer Journal 2007; 43 3826-3837.
[6] Xue M L, Jing S, Chuah H H, Ya Z X. J. Macromol. Sci. Part B: Physics 2004;43: 1045–1061.
[7] Pyda M, Wunderlich B. J. Polym. Sci.Part B: Polym. Phys. 2000;38:2426.
[8] Scherzer T, Strehel V, Tanzer W, Wartewig S. Progr Colloid Polym Sci 1992; 90:202-205.
[9] Liang L, Qili W, Li S, Wu P. Applied Spectroscopy 2008; 62:1129-1136.
[10] Yamen M, Ozkaya S, Vasanthan N. Journal of Polymer Science: Part B: Polymer Physics 2008; 46: 1497-1504.
[11] P. Musto, Abbate M, Ragosta G Scarinzi G. Polymer 2007;48:3703-3716.

Non-isothermal Crystallization of Poly(lactic acid)-Hemp-Silica Nanocomposites Plasticized with Tributyl Citrate

I.R. Mustapa[a], S. Chandran[a,b], R.A. Shanks[a] and I. Kong[a]

[a]*School of Applied Sciences, RMIT University, Box 2476 GPO, VIC 3001, Australia.*

[b]*School of Chemical Science, Mahatma Gandhi University, Kottayam, Kerala, India 686560.*

Non-isothermal crystallization of PLA composites consisting of hemp fibres and nanosilica was studied by differential scanning calorimetry at various scanning rates. The crystallization peak of plasticized PLA composites increased 6-18 °C compared with plasticized PLA. Hemp fibres promoted imperfect crystals that recrystallize in the melting temperature range and nanosilica acted as a nucleating agent in the PLA composites, enhancing the crystallization rate of the PLA.

1. Introduction

Poly(lactic acid)(PLA) is a semi-crystalline polymer and its physical and mechanical properties largely depend on the degree of crystallinity and crystallization rate. In amorphous form, application of PLA is limited by low glass transition temperature (T_g) and at temperatures greater than T_g, the crystalline form offers useful mechanical and physical properties. Generally addition of filler and plasticizer provides effective nucleation and mechanical reinforcement in polymer composites that induced nucleation for crystallization of PLA matrix, accelerating the overall crystallization process. Nucleation agents such as talc [1], silica [2], and carbon black [3] intensified the crystallization by dense heterogeneous nucleation on the surface of additive particles. Meanwhile addition of plasticizer such as citrate esters [4], effectively reduce T_g and increase the chain mobility of PLA.

The aim was to prepare hybrid PLA composites containing micro-sized hemp fibres and nano-silica particles, measure crystallization and melting of the PLA matrix and interpret using kinetic model. Non-isothermal crystallization is a practical method to investigate the crystallization behaviour of PLA because polymers are usually processed under non-isothermal environments. Non-isothermal crystallization kinetics of PLA composites using Avrami model is used in this paper to evaluate the nucleation ability and crystal growth rate due to hemp fibres, nanosilica and the contribution of tributyl citrate (TBC) plasticizer in the PLA composites.

2. Composite preparation

2.1 Materials and Preparation: Poly(lactic acid) (2002D, extrusion grade) was obtained in pellet form from Natureworks Co., Minnetonka, USA. Hemp Fibre was purchased from Hemp Store Auckland, New Zealand. Fumed silica Cab-O-Sil M5 was purchased from Cabot Corporation USA. Chloroform (purity 99.0-99.4 %, laboratory grade) was obtained from Merck KGaA, Darmstadt, Germany. PLA composites with and without TBC (10 %·w/w of total composite) were prepared by solution casting followed by a film stacking method. A pre-determined amount of filler (2.5 %·w/w nanosilica) was added and well dispersed in PLA solution in chloroform by ultrasonication for 30-45 min. The sonicated PLA–silica dispersion was added to three layers woven hemp fibre mat. Solvent was evaporated, then the composite was consolidated by compression moulding at 180 °C for 10 min under a pressure of 2.4 MPa and 30 s at 12.1 MPa. Neat PLA and plasticized PLA were similarly prepared for comparison.

2.2 Characterization: Non-isothermal crystallization kinetics was performed with a Perkin Elmer Pyris 1 differential scanning calorimetry (DSC), calibrated with indium according to the recommended procedure. Crystallization curves were obtained by heating about 8 mg mass of composites in a sealed aluminum pan. The measurement was carried out at various scanning rates (1, 2 and 10 K·min^{-1}) using N_2 as the purging gas. Prior to a cooling scan, composites were first heated to 180 °C and held in the molten state for 2 min to remove any thermal history.

3. Results and Discussion

3.1 Non-isothermal Crystallization and Melting Behaviour

The action of hemp and nanosilica with and without TBC as a plasticizer on crystallization and melting behaviour of PLA composites was quantitatively analysed through non-isothermal DSC. Table 1 shows the thermal properties for PLA and PLA-silica (PS), PLA-hemp (PH), PLA-hemp-silica (PHS) and PLA, PS, PH, PHS plasticized with TBC known as (pPLA, pPS, pPH and pPHS) at selected scanning rates of 2.0 K·min^{-1}.

Table1: Thermal properties of PLA composite with and without plasticizer.

Composite	T_{cc} (°C)	T_{m1} (°C)	T_{m2} (°C)	Composite	T_{cc} (°C)	T_{m1} (°C)	T_{m2} (°C)	T_c (°C)
PLA	93.5	no peak	150.5	pPLA	80.9	no peak	150.4	81.2
PS	88.4	no peak	151.1	pPS	no peak	no peak	150.9	87.4
PH	99.8	149.1	159.3	pPH	no peak	140.1	153.7	96.0
PHS	98.1	150.1	160.3	pPHS	no peak	138.7	151.6	99.1

Crystallization of neat PLA and PLA composites on cooling, under cooling rate used, was negligible, whereas PLA crystallizes on heating above T_g producing a crystalline phase, through a cold crystallization process, as shown in Fig. 1a.

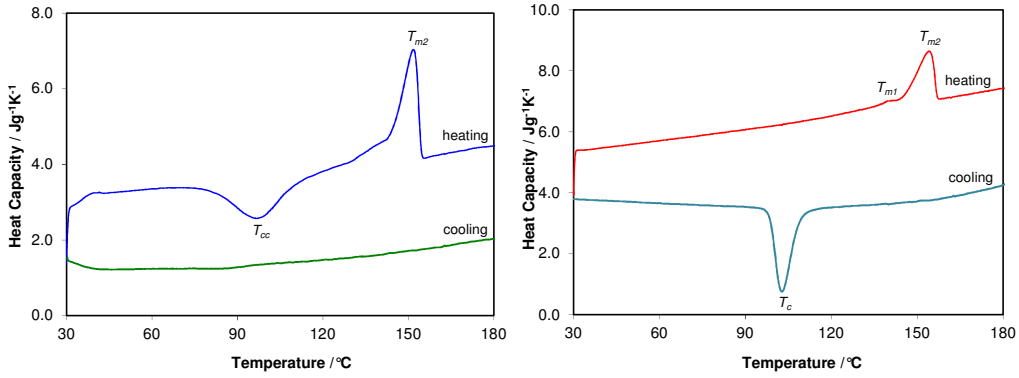

(a) (b)

Fig 1. Non-isothermal DSC curve of (a) PLA and (b) pPH at scanning rates of 2.0 K·min^{-1}.

The addition of 2.5 %·w/w nanosilica in PLA matrix (PS) reduced the cold crystallization temperature (T_{cc}) and slightly increased melting temperature (T_{m2}). This result revealed that nanosilica acted as an effective nucleating in the PLA matrix and it modified the morphology and the physical properties of PLA composites. However, T_{cc} and T_{m2} for PLA reinforced with hemp fibres (PH) and a combination of hemp and nanosilica in PLA composites (PHS) were higher than neat PLA because the hemp fibres restricted mobility of PLA in the composites and created imperfect crystals, which melt with two peaks or a double melting endotherm. The double melting peak indicates less perfect crystals melting at lower temperature (T_{m1}) and recrystallizing to more perfect crystals and then melting again at higher temperature (T_{m2}). An introduction of hemp fibres and nanosilica in PLA composites lead to

an increase of T_{cc} and T_{m2} of about 5.0 °C and 9.0 °C, respectively. As expected, the addition of TBC in PLA matrix reduced the T_{cc} of neat PLA and all PLA composites. TBC induced a crystallization peak (T_c) on cooling (Fig. 1b) that enhanced the nucleating ability of the fillers and chain mobility in PLA composites.

Non-isothermal crystallization kinetics was used to further analyse the nucleation activity of PLA composites with addition of TBC. The crystallinity $\chi(T)$ of PLA composites at temperature T was obtained by exploiting data from DSC curves as in equation 1,

$$\chi(T) = \int_{To}^{T}\left(\frac{dH}{dT}\right)dT \Big/ \int_{To}^{\infty}\left(\frac{dH}{dT}\right)dT \qquad (1)$$

where, $T_o = T_{onset}$, $T_\infty = T_{end}$ of the crystallization and dH = enthalpy of crystallization.

Equation 1 was transformed to χ(t) using a relationship between crystallization time t and temperature T in a non-isothermal crystallization process as in equation 2:

$t = (T_o - T)/\beta$, T = temperature at the crystallization time t, β = cooling rate. (2)

Hence, the fractional of crystallization of PLA composites are obtained from equation 3,

$$\chi(t) = \int_{0}^{t}\left(\frac{dH}{dt}\right)dt \Big/ \int_{0}^{\infty}\left(\frac{dH}{dt}\right)dt \qquad (3)$$

Fig. 2 represents the fractional degree of crystallinity, χ(t) of pPLA, pPS, pPH and pPHS composites as a function of time t at various scanning rate. Data was obtained from crystallization on cooling, as shown in Figure 1b (example of pPH at 2.0 K·min^{-1}). The half-time of crystallization ($t_{0.5}$) was directly obtained from a plot of χ(t) against t, which indicates the change in time from the onset of crystallization to the period when the χ(t) is 50 %. Results show that the $t_{0.5}$ of pPLA composites was higher than pPS, pPH and pPHS for all scanning rates. The addition of filler increased the crystallization rate indicating that the addition of plasticizer and nucleating agents enhanced the transportation ability of polymer chains.

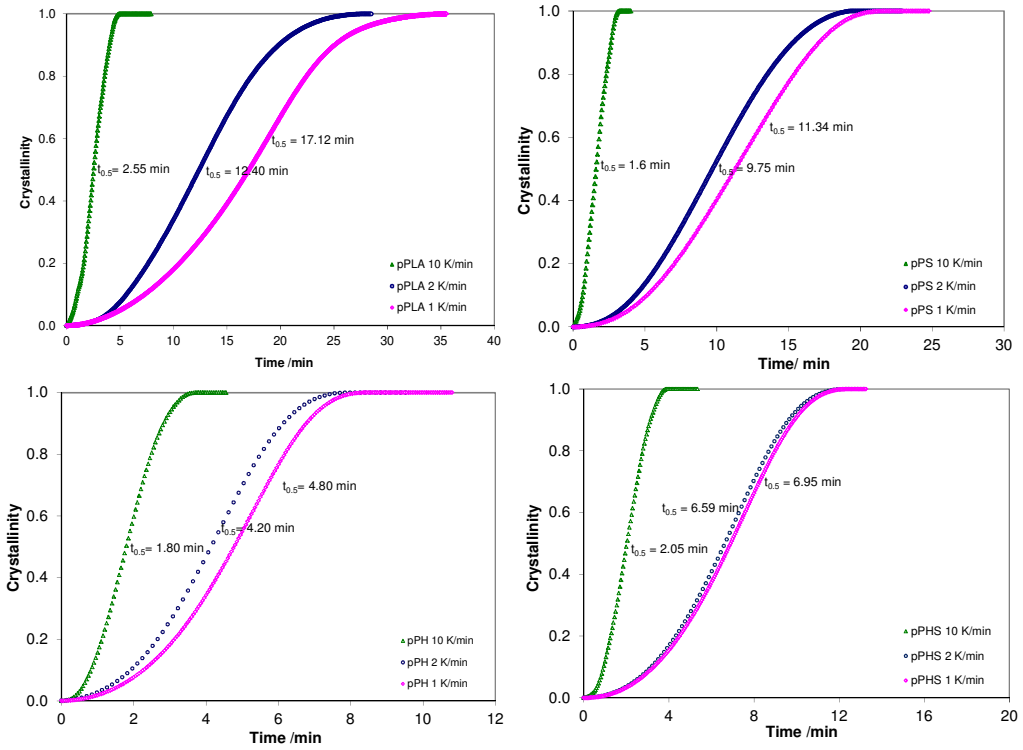

Fig 2. Plot of χ(t) against crystallization time at various scanning rate for pPLA, pPS, pPH and pPHS.

In addition to the $t_{0.5}$, kinetic rate coefficients based on Avrami model was used to characterize non-isothermal crystallization kinetics of plasticized PLA composites. Avrami equation explores the primary stage of non-isothermal crystallization, according to which the crystallinity, $\chi(t)$ dependent on crystallization time t as in equation 5,

$$1-\chi(t)=\exp[-kt^n] \quad (5)$$

$$\log[-\ln(1-\chi(t)] = \log k + n\log t \quad (6)$$

where, k = crystallization rate coefficient and n represents nucleation and growth geometry.

Fig. 3 shows a plot of log[-ln(1-$\chi(t)$] against log$t$ for pPLA, pPS,pPH and pPHS at various scanning rates. The Avrami exponent n was obtained from the slope and the intercept gave the crystallization rate constant k.

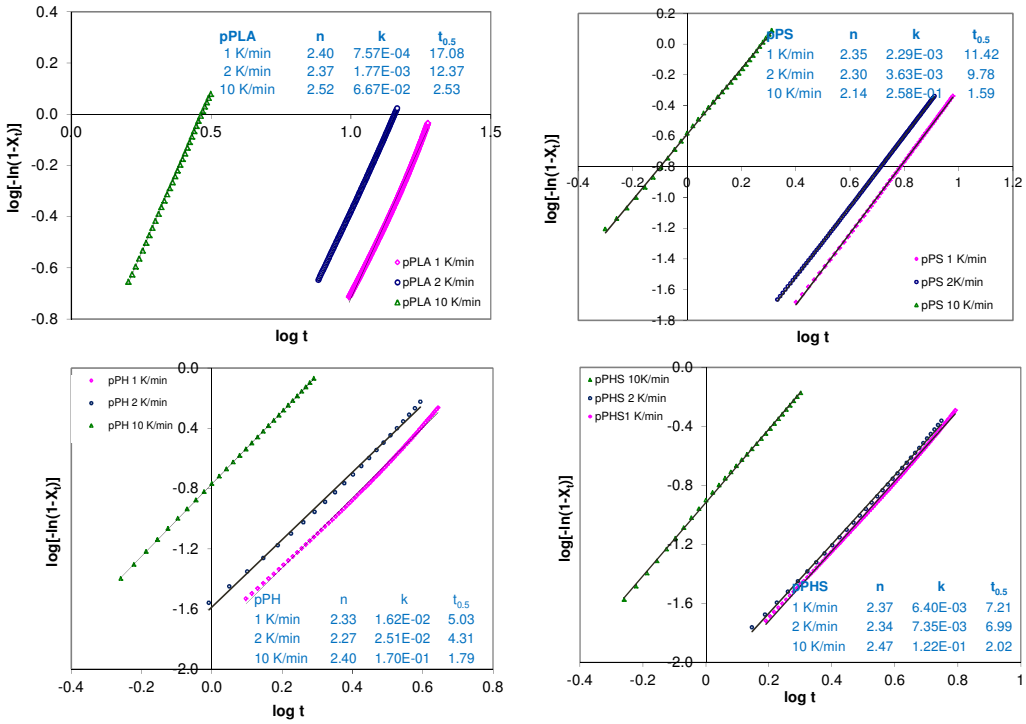

Fig. 3 log[-ln(1-$\chi(t)$] against log$t$ curve of pPLA, pPS, pPH and pPHS at various scanning rates.

Referring to Fig. 3, a linear relationship was obtained for all composites indicating that the Avrami equation is valid to analyse the non-isothermal crystallization of PLA composites. Results showed that nucleating agents in PLA composites enhanced the crystallization rate of PLA composites. The predicted $t_{0.5}$ by the Avrami fit of all PLA composites are in good agreement with experimental values for at least 50% conversion of crystalline state.

4. Conclusion

Hemp fibres promoted imperfect crystals revealed by double melting endotherms that undergo rearrangement and recrystallization through a partial melting, recrystallization and remelting (mrr) process. Hemp and nanosilica acted as nucleating agents that enhanced the nucleation and crystallization rate of PLA composites and increased overall crystallinity.

References

[1] Li M, Hu D, Wang Y and Shen C. 2010. *Polym Eng Sci*, **50**(12), 2298-2305.
[2] Zhang Y, Deng B, Liu Q and Chang G. 2012. *J of Macromol Sci, Part B,* **52**(2), 334-343.
[3] Su Z, Guo W, Liu Y, Li Q and Wu C. 2009. *Polymer Bulletin*, **62**(5), 629-642.
[4] Harte I, Birkinshaw C, Jones E, Kennedy J, DeBarra E. 2012. *J of Appl Polym Sci*, 1-7.

PROCEEDINGS - 37th ANNUAL CONDENSED MATTER AND MATERIALS MEETING, 5 - 8 February, 2013. Wagga Wagga, NSW, Australia

Electron Self-energy Variation from Rydberg Surface-state Resonances on Cu(110) surface

M. N. Read

School of Physics, University of New South Wales, Sydney NSW 2052, Australia.

We predict the energy position of five $n = \infty$ members of the Rydberg series of surface image barrier resonances above vacuum level to 75 eV for Cu(110) at $\bar{\Gamma}$. Measurement of these resonance positions would enable the real part of the excited quasi-electron self-energy to be determined for Cu.

1. Introduction

Here we seek to determine, by comparison with experiment, the energy dependence of the electron quasiparticle self-energy $\Sigma(E)$ at excited (above vacuum) energies for the Cu crystal. This is performed by calculating for the Cu(110) surface, the bulk and surface electronic band structure above the vacuum level and including any barrier image (Rydberg) surface-state resonances that may occur. Knowledge of $\Sigma(E)$ in this energy range is required for analysis in many bulk and surface spectroscopies including photoemission and low energy electron scattering.

2. Method

In the scattering method used here [1, 2] the electron or quasi-electron scatters between the crystal and surface barrier shown in Fig. 1. The wave function of the electron of energy E that is incident on the surface barrier is expanded into a combination of plane waves each with $\boldsymbol{k}_{\|}$ values that add multiples of the reciprocal-net vectors and corresponding $k_{\perp}$. Sustained multiple scattering can occur between barrier and crystal where the electron is trapped in the surface region and hence occupies a surface state or resonance. Near the top of the surface barrier in a series of image (Rydberg) state/resonances with members $n = 1$ to ∞ can occur as shown in Fig. 1. The $n = \infty$ state occurs at the energy at the top of the barrier. The energy separation of the muffin-tin zero of energy inside the crystal E_o (interstitial potential) and the energy at the top of the barrier gives the theoretical inner potential of the crystal surface.

The condition for a surface state/resonance is that one or more of the eigenvalues of the matrix $\boldsymbol{S}^{\mathrm{II}}\boldsymbol{M}$ approach unity where $\boldsymbol{M}$ is the reflection matrix of the crystal and $\boldsymbol{S}^{\mathrm{II}}$ is the internal reflection matrix of the surface barrier [1]. For computational purposes this can be expressed as

$$|\det [\boldsymbol{I} - \boldsymbol{S}^{\mathrm{II}}\boldsymbol{M}]| \rightarrow \text{ minimum} \qquad (1)$$

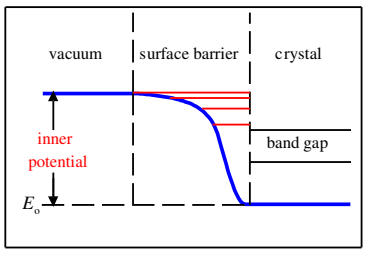

Fig. 1. Potential energy in the near-surface region of a crystal (vertical axis). Red lines indicate the image (Rydberg) series of surface-state resonances. The muffin-tin zero (interstitial potential) is E_o.

3. Calculations for ground-state electrons

First we calculate the near-surface complex bulk and surface band structure for Cu(110) in the ground state (below vacuum) where the self-energy correction to the electron one-particle ground-state is small. The surface barrier potential is obtained from the experimental

work function and two below-vacuum surface state energies at $\overline{\Gamma}$ [3, 4]. From this model we calculate all the other surface states and resonances for the whole surface Brillouin zone that have been found experimentally [5, 6]. We find that adjusting the surface atomic layer potential by a layer contraction of 10% has only a small effect on the energies of the surface states/resonances and is less than other theoretical and experimental uncertainties. Hence any redistribution of electrons in the surface atomic layer has negligible effect for this surface. This verifies the accuracy of the method. Here we show the calculations for $k_{\|} \equiv \overline{\Gamma}$, $\overline{X}$, $\overline{Y}$ in Figs. 2 (a), (b), (c).

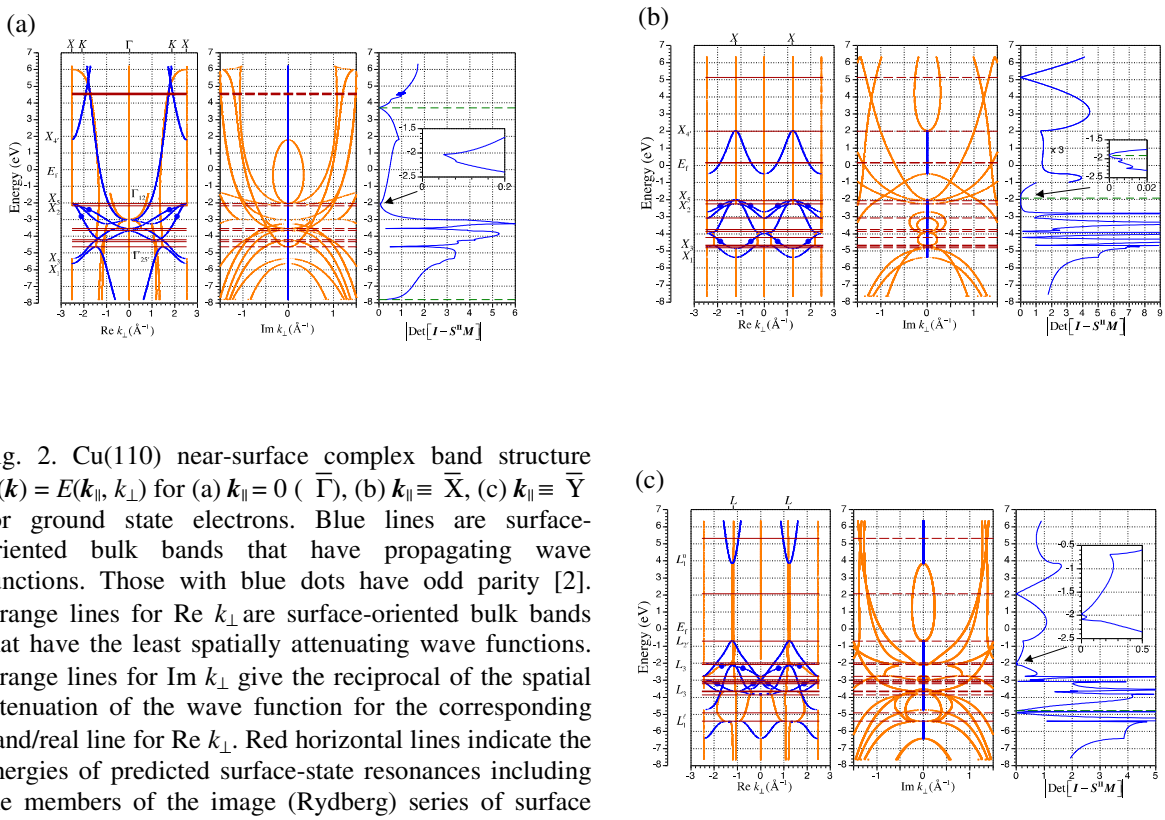

Fig. 2. Cu(110) near-surface complex band structure $E(\boldsymbol{k}) = E(\boldsymbol{k}_{\|}, k_{\perp})$ for (a) $\boldsymbol{k}_{\|} = 0$ ($\overline{\Gamma}$), (b) $\boldsymbol{k}_{\|} \equiv \overline{\mathrm{X}}$, (c) $\boldsymbol{k}_{\|} \equiv \overline{\mathrm{Y}}$ for ground state electrons. Blue lines are surface-oriented bulk bands that have propagating wave functions. Those with blue dots have odd parity [2]. Orange lines for Re $k_{\perp}$ are surface-oriented bulk bands that have the least spatially attenuating wave functions. Orange lines for Im $k_{\perp}$ give the reciprocal of the spatial attenuation of the wave function for the corresponding band/real line for Re $k_{\perp}$. Red horizontal lines indicate the energies of predicted surface-state resonances including the members of the image (Rydberg) series of surface resonances. Green dashed lines indicate the free-electron energies of the crystal surface.

4. Self-energy

The quasi-electron many-body self-energy $\Sigma(E)$ has real and imaginary parts; Re $\Sigma(E)$ arises from virtual excitations, Im $\Sigma(E)$ arises from inelastic collisions. For Re $\Sigma(E)$ for Cu we use a theoretical calculation [7] that is shown here in Fig. 3 (a). The difference between the excited and ground muffin-tin zero (interstitial potential) energies is $E_o^{ex} - E_o^{gr}$. Positive values indicate greater binding energy of the bands. Hence there is an energy-dependent excited inner potential that varies from the ground state value by an amount equal to Re $\Sigma(E)$. For Im $\Sigma(E)$ for Cu we use an estimate that was made from a LEED analysis [8] that is shown here in Fig. 3 (b).

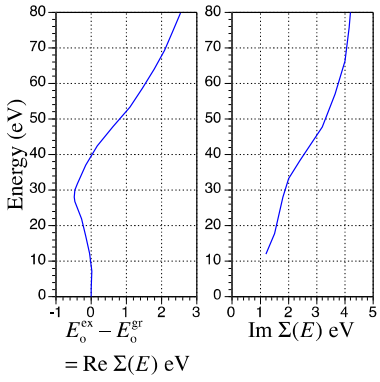

Fig. 3. Electron quasi-particle self-energy Σ variation with energy E from Fermi energy $E_f = 0$. Real part is from Ref. [7] and imaginary part from Ref. [8]. E_o^{ex} and E_o^{gr} are the excited and ground state muffin-tin zeros (interstitial potentials) respectively.

5. Calculations for excited-state quasi-electrons

The calculated bulk and surface-state resonances for excited states above vacuum level for Cu(110) for $k_{\|} \equiv \bar{\Gamma}$ including both Re $\Sigma(E)$ and Im $\Sigma(E)$ are shown in Fig. 4. All bands now have spatially attenuating wave functions. Red lines indicate the prediction of the energies of a number of Shockley (barrier-type) surface resonances. Black lines indicate the prediction of the energies of a number of $n = \infty$ Rydberg (image barrier) resonances.

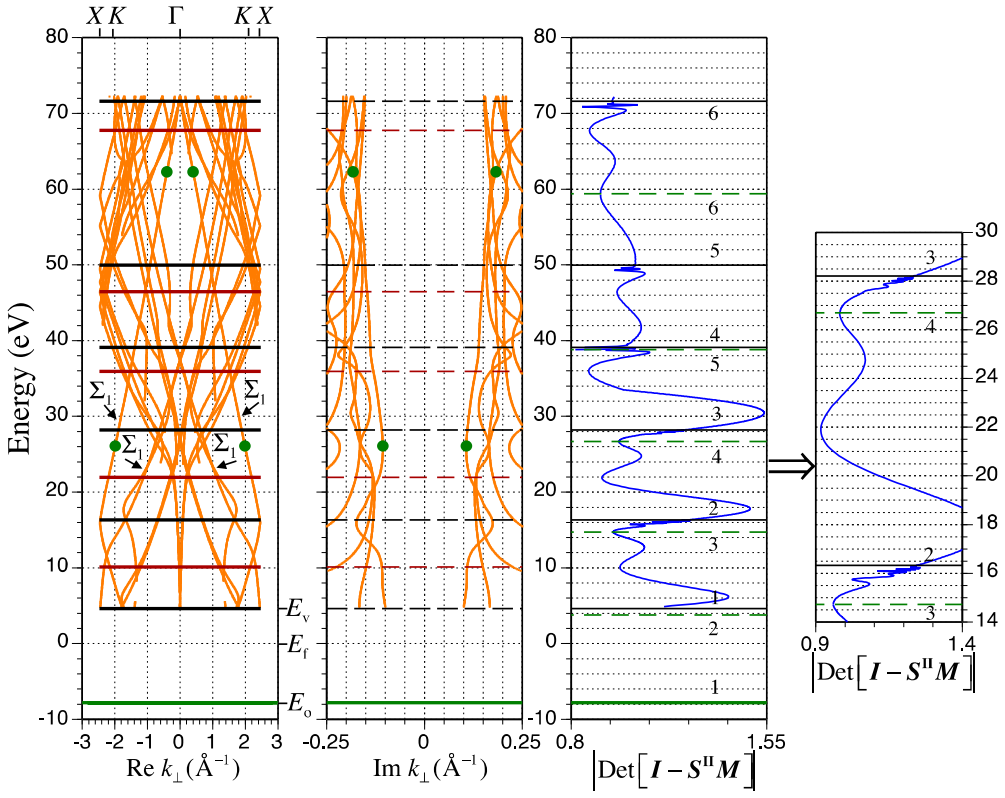

Fig. 4. Cu(110) near-surface complex band structure $E(\boldsymbol{k})=E(\boldsymbol{k}_{\|}, k_{\perp})$ for $\boldsymbol{k}_{\|} = 0$ ($\bar{\Gamma}$) for excited quasi-electrons with self-energy as in Fig. 3. Orange lines are surface-oriented bulk bands that have wave functions that are least spatially attenuating. Green dots indicate the corresponding real and imaginary parts for the band labelled Σ_1. Black horizontal lines inicate the energies of the predicted $n = \infty$ members of the Rydberg series of image surface resonances and red horizontal lines indicate other surface-state resonances. Green solid lines indicate the muffin-tin zero of potential E_o. E_f and E_v are the Fermi and vacuum levels respectively. Green dashed lines indicate the free-electron energies of the crystal surface. Refer to the text for the numbers in the third and fourth panel.

Phase shifts for Cu were recalculated taking into account the energy variation of the excited muffin-tin zero E_o^{ex} with respect to the ground state value E_o^{gr} from the data in Sec. 4. This includes Re $\Sigma(E)$ for the excited bulk band structure calculation relative to the zero of energy in the present calculation E_o. For the surface calculation the excited inner potential was introduced by varying the energy of the top of the surface barrier with respect to E_o by Re Σ(E). Inelastic collisions were included from the energy variation of Im $\Sigma(E)$ from the data in Sec. 4.

The formation of above-vacuum surface-state-resonances can be described qualitatively as follows. At any given energy E above vacuum level the plane-wave members of the expansion have different $\boldsymbol{k}_{\|}$ and corresponding $k_{\perp}$ values. Some of these plane-wave members will have sufficient $k_{\perp}$ to be transmitted above the barrier height and do not take part in the formation of surface-state resonances. Some will not have sufficient $k_{\perp}$ and will be internally reflected at the surface barrier. The scattering of these latter plane-wave members from the

crystal may form surface-state resonances when it is sustained scattering. Between solid green lines and black lines with the label '1' in the third and forth panel of Fig. 5 specific members of the plane-wave set scatter from the bottom to the top of the surface barrier and at the black line are transmitted above the barrier where they do not take part again in surface resonance formation. This situation continues progressively for each of the remaining plane-wave members in each of the regions labelled '2 to 6'.

The energy positions of the $n = \infty$ image resonances depend on the value of the excited inner potential and hence on the value of Re $\Sigma(E)$. In the calculations their energy position is insensitive to other aspects of the bulk and surface potentials because the asymptotic part of this potential extends far into the vacuum from the crystal surface region and has known form. Dilation of the surface layer/s or changes in their potentials do not effect the excited inner potential and hence the energy position of the $n = \infty$ image resonances. These changes and bulk potential changes may however significantly affect the energies of other surface resonances including lower energy members of the Rydberg series. The quantity E_o, the muffin-tin zero of energy used in the calculations is a theoretical quantity and is dependent on the theoretical bulk potential used. However the energy of the top of the ground-state surface barrier is the vacuum level E_v. The Fermi level E_f is this value minus the work function that is experimentally determined. Hence the calculations can be referred to the Fermi level which is a physically measurable quantity and E_o is not involved in determining Re $\Sigma(E)$ from the $n = \infty$ image resonances energy positions.

Self-energy corrections for bulk bands are significant in the analysis of photoemission experiments because of the precision with which the energy bands can be measured in these spectroscopies. Hence measurement with the required precision of the energies of the above-vacuum $n = \infty$ image resonances that are found for Cu(110) may be possible also and would permit Re $\Sigma(E)$ to be determined at certain energies. This would be achieved by including trial $\Sigma(E)$ variations in the calculations of the energy of $n = \infty$ image resonances relative to the Fermi energy as shown here and comparing with the experimental result.

6. Conclusion

Experimental measurement by multiphoton or inverse photoemission of the $n = \infty$ members of each set of Rydberg surface resonances would permit determination of the energy dependence of the excited inner potential and hence the real part of the self-energy. This would be achieved by comparison with calculations for trial self-energy corrections as shown here.

The excited attenuating bulk states at $\overline{\Gamma}$ (normal electron emission) on Cu(110) have not been calculated before. Comparison of such calculated bulk bands with measurement for different trial values of Im $\Sigma(E)$ could determine that value.

In general, knowledge of such excited attenuating bulk states and surface-state resonances to the energy precision shown in the above calculations, is required in the explanation and analysis of many surface spectroscopies.

References

[1] McRae E G 1979 *Rev. Mod. Phys.* **51** 541.
[2] Read M N 2009 *Phys. Rev. B* **80** 035435.
[3] Cord B, Courths R and Wern H 1985 *Phys. Rev. B* **31** 1164.
[4] Straub D and Himpsel F J 1986 *Phys. Rev. B* **33** 2256.
[5] Kevin S D 1983 *Phys. Rev. B* **28** 4822.
[6] Schneider R, Dürr H, Fauster Th and Dose V 1990 *Phys. Rev. B* **42** 1638.
[7] Nilsson P O and Larsson C G 1983 *Phys. Rev. B* **27** 6143.
[8] Lindgren S Å, Walldén L, Rundgren J and Westrin P 1984 *Phys. Rev. B* **29** 576.

PROCEEDINGS - 37th ANNUAL CONDENSED MATTER AND MATERIALS MEETING, 5 - 8 February, 2013. Wagga Wagga, NSW, Australia

Controlled Synthesis of Nanocrystalline BaFCl:Sm^{3+} X-ray Storage Phosphor

Xianglei Wang, Hans Riesen

School of Physical, Environmental and Mathematical Sciences, The University of New South Wales, UNSW Canberra (ADFA), Canberra, ACT 2600, Australia

Nanocrystalline BaFCl:Sm^{3+} was prepared by co-precipitation at room temperature employing methanol/water mixtures as the solvent. The structure of as-prepared samples was investigated by powder X-ray diffraction (XRD) and scanning electron microscopy (SEM). It is shown that the ratio of methanol/water can be used to control the crystallite size of the prepared phosphor.

1. Introduction

Nanocrystalline BaFCl:Sm^{3+} is a very efficient photoluminescent X-ray storage phosphor with potential applications in medical imaging and personal radiation monitoring [1-2]. Its storage mechanism is based on the capture of radiation generated electrons and holes upon ionizing radiation [1]. The detailed storage mechanism and optical properties have been investigated by Riesen and Liu [3-5]. The reported synthesis method of nanocrystalline BaFCl:Sm^{3+} is based on the co-precipitation of $BaCl_2 \cdot 2H_2O$, $SmCl_3 \cdot 6H_2O$ and $NH_4 \cdot HF$ dissolved in pure water [1]. Liang et al. synthesized BaFBr:Eu^{2+} crystals via the co-precipitation of $BaBr_2$, $EuBr_2$ and NH_4F dissolved in ethanol/water solutions [6]. According to Liang et al., the ratio of ethanol/water in the solvent has a control effect on the growth of crystals as ethanol has smaller dielectric constant and polarity than water. Enlightened by these previous reports, nanocrystalline BaFCl:Sm^{3+} is prepared using methanol/water mixtures as the solvent in the present paper. The structure and particle size of as-prepared samples from different mixtures are investigated by photoluminescence (PL), powder X-ray diffraction (XRD) and scanning electron microscopy (SEM).

2. Experimental

$BaCl_2 \cdot 2H_2O$ (ACS reagent, ≥99%), NH_4F (ACS reagent, ≥98%), $SmCl_3 \cdot 6H_2O$ (≥99%) and HCl (36%) were used as obtained from Sigma-Aldrich Pty Ltd without further purification. Methanol (analytical reagent, 99.8%) from Ajax Finechem Pty Ltd and milli-Q ultrapure water (Millipore, 14 MΩ·cm) were used for preparing solvents. For a typical sample preparation, two plastic centrifuge tubes (Corning self-standing, 50 mL PP) were both filled 22 mL methanol and 2 mL water. Then 0.407 g $BaCl_2 \cdot 2H_2O$, 100 µL of 1 mg/mL aqueous solution of $SmCl_3 \cdot 6H_2O$ (0.1 mg) and 10 µL of 36% HCl were added into one tube and the tube was shaken to make sure the chemicals were fully dissolved. At the same time, 0.031 g NH_4F was added to the other tube. Subsequently, the solutions from the two tubes were mixed to form a white precipitate. The precipitate was centrifuged and dried at 55 ºC for 24 h, cooled and ground gently to yield a white powder. The same procedures were used to prepare a range of samples with various methanol/water ratios (R). The as-prepared samples were denoted as S1 (R=11:1), S2 (R=3:1), S3 (R=2:1), S4 (R=1:1), S5 (R=1:2), S6 (R=1:3) and S7 (R=0:24), respectively. The detailed composition for each sample is summarized in Table 1.

Table 1: Compositions of samples.

No.	Methanol (mL)	Water (mL)	$BaCl_2 \cdot 2H_2O$ (g)	NH_4F (g)	$SmCl_3 \cdot 6H_2O$ (mg)	HCl (μL)
S1	22	2	0.4071	0.0308	0.1	30
S2	18	6	1.2214	0.0926	0.3	80
S3	16	8	1.6284	0.1234	0.4	100
S4	12	12	2.4428	0.1852	0.6	150
S5	8	16	2.4428	0.1852	0.6	150
S6	6	18	2.4428	0.1852	0.6	150
S7	0	24	2.4428	0.1852	0.6	150

The samples were characterized by a Siemens X-ray diffractometer (40kV, 25mA, CuK_{α}). The measured powder X-ray diffraction patterns were compared with the reference card ICDD No. 34-674 for standard BaFCl data. The secondary electron images were taken on a NanoSEM 230 ultra-high resolution field emission scanning electron microscopy (FESEM) at the Mark Wainwright Analytical Centre of The University of New South Wales and the particle size of the samples was analysed via ImageJ software. Photoluminescence spectra of the samples were measured using a Horiba Jobin-Yvon Spex Fluoromax-3 fluorometer before and after exposure under a dental X-ray unit (Belmont Searcher Model DX-068, 60 kVp, 8 mA).

3. Results

The powder X-ray diffraction (XRD) patterns of the as-prepared products were measured and compared with standard BaFCl data (ICDD card No. 34-674). The results confirm the BaFCl phase in all seven samples as are shown in Fig. 1. All prominent peaks could be indexed to the pure tetragonal BaFCl structure with the space group of P4/nmm [7]. No peaks from other phases are evident. It follows from Fig. 1 that, when the methanol/water ratio is decreasing from 11:1 to 0:24, the intensities of all diffraction peaks are becoming stronger and sharper. This implies an increase of crystallite size and crystallinity. Also from Fig.1 it follows that the XRD pattern shows a larger deviation from the ICDD card data with increasing crystallite size. This indicates a preferred orientation of the crystalline platelets with increasing size. According to the Scherrer equation [8], the crystallite size (D) can be crudely estimated as $D=\frac{k\lambda}{\beta \cos\theta}$ where k is a constant (0.89), λ is the wavelength of the X-ray, β is the full width at half maximum and θ is the diffraction angle. The prominent peaks, corrected for instrumental broadening, in the range of θ from 20 to 50 degrees are used to calculate the average crystallite sizes. The results for each sample are listed in Table 2 and a particle size range from around 110 nm to 370 nm is yielded.

Table 2: Crystallite size as a function of methanol/water ratio, determined by XRD and SEM

Sample No.	Methanol/Water Ratio (R)	XRD Crystallite Size (nm)	SEM Crystallite Size (nm)
S1	11:1	114	120-150
S2	3:1	187	160-170
S3	2:1	203	190-200
S4	1:1	225	230-240
S5	1:2	244	250-260
S6	1:3	251	260-270
S7	0:24	373	380-400

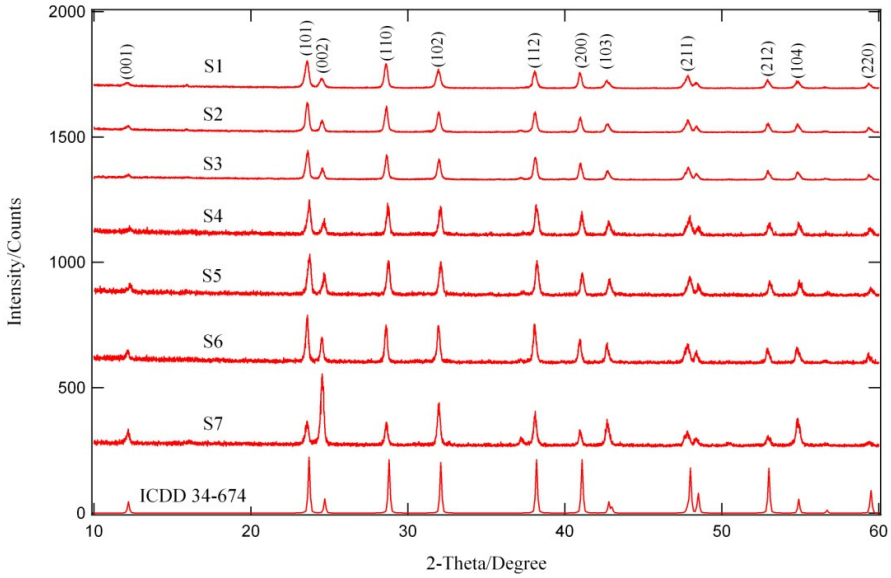

Fig. 1: XRD patterns of as-prepared samples S1 to S7 with corresponding methanol/water ratios from 11:1 to 0:24 compared with standard BaFCl data (ICDD card No. 34-674). Prominent peaks are indexed.

The secondary electron images taken by FESEM exhibit the morphology of the as-prepared samples. As shown in Fig. 2, all the samples have similar lamellar particles with irregular shapes and particles accumulate in a parallel direction in layers. It is clearly observed that when the methanol/water ratio is high the average particle size is small. With increasing water content of the solvent, larger particles are formed. In particular, as the methanol/water ratio decreases from 11:1 to 0:24, the particle size gradually increases from around 120 nm to around 400 nm. The estimated particle sizes of each sample are also listed in Table 2. The change of particle size indicates a strong dependence on the methanol/water ratio, which is in agreement with the results from the XRD measurement.

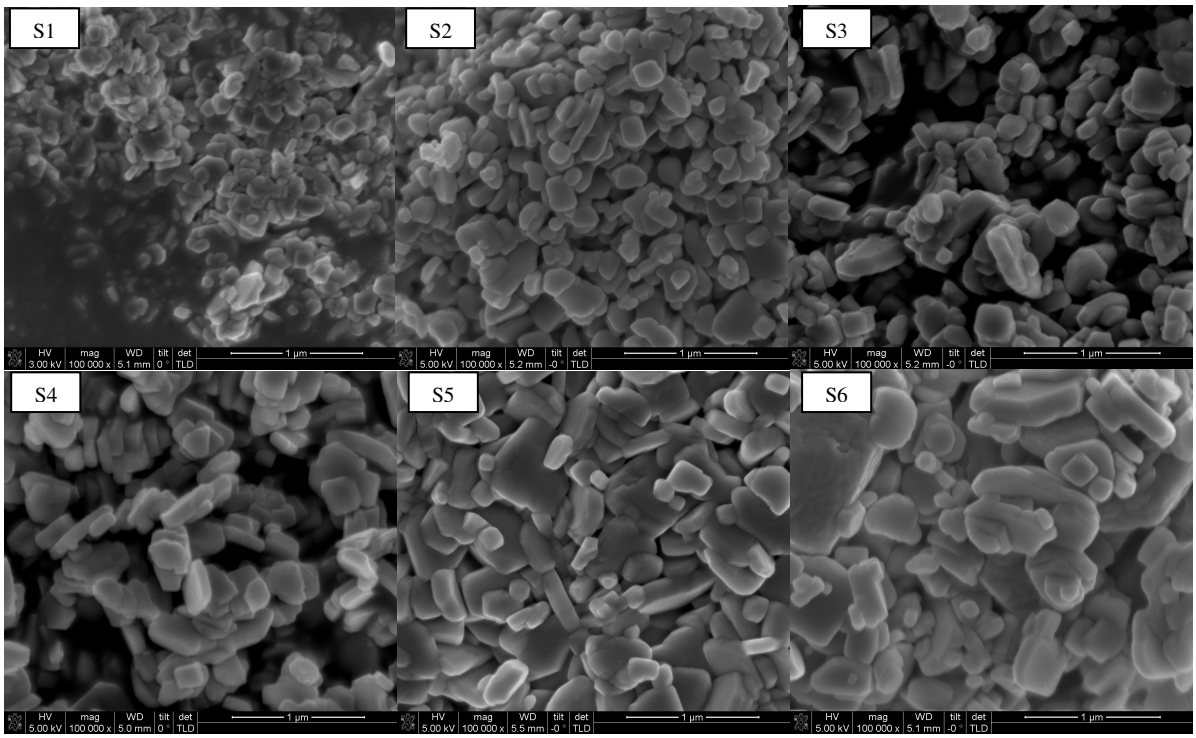

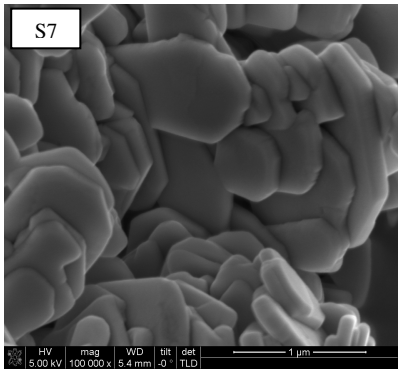

Fig.2: Secondary electron images of as-prepared samples S1 to S7 (see Table 1).

It appears that in general the X-ray induced photoluminescence signal of Sm^{2+} increases with increasing particle size.

4. Conclusion

A method for controlled synthesis of nanocrystalline BaFCl:Sm^{3+} at room temperature employing methanol/water mixtures is reported. The powder X-ray diffraction measurement confirms the purity of the BaFCl phase in the as-prepared samples and provides the average crystallite size in each sample. The secondary electron images characterize the morphology of the as-prepared samples and the average particle sizes can be estimated. The results from SEM and XRD both show an increase of particle size with the increase of water content in the mixture, indicating the influence of the high dielectric constant of water on the particle size in the final products.

Acknowledgements

The Australian Research Council (ARC Linkage Project LP110100451) and the Australian Microscopy and Microanalysis Facility are acknowledged for support of this work.

References

[1] Riesen H and Kaczmarek W A 2007 Inorg. Chem. 46 7235-7237
[2] Riesen H and Kaczmarek W A 2005 International PCT Application WO2006063409
[3] Riesen H and Liu Z 2012 Optical Storage Phosphors and Materials for Ionizing Radiation available from: http://www.intechopen.com/books/current-topics-in-ionizing-radiation-research/optical-storage-phosphors-and-materials-for-ionizing-radiation
[4] Liu Z 2012 PhD thesis The University of New South Wales Canberra
[5] Liu Z, Stevens-Kalceff M A and Riesen H 2012 J. Phys. Chem. C 116 8322-8331
[6] Liang Q, Li Z, Ma W, Shi Y and Yang X 2012 Mater. Res. Bull. 47 2357-2363
[7] Hagemann H, D'Anna V, Lawson Daku M and Kubel F 2012 Cryst. Growth Des 12 1124-1131.
[8] Scherrer P 1918 Nachr. Ges. Wiss. Göttingen 26 98-10.

PROCEEDINGS - 37th ANNUAL CONDENSED MATTER AND MATERIALS MEETING, 5 - 8 February, 2013. Wagga Wagga, NSW, Australia

Si Doping Induced Hydrophobic to Hydrophilic Transition on Graphene: a First Principles Study

Q. G. Jiang,[a,b] Z. M. Ao,[b*] S. Li[b]

[a] *Key Laboratory of Auto mobile Materials (Jilin University), Ministry of Education, and Department of Materials Science and Engineering, Jilin University, Changchun 130025, China*

[b] *School of Materials Science and Engineering, The University of New South Wales, Sydney, NSW 2052, Australia*

The dissociative adsorption of a H_2O molecule on Si-doped graphene is investigated by using first principles calculations. It is found that the dissociative energy barrier is reduced from 3.6 eV on pristine graphene to 0.5 eV on Si–doped graphene, which indicates that this dissociative adsorption can occur smoothly at room temperature. Therefore, doping Si into graphene can convert graphene from hydrophobic to be hydrophilic, which is important for its potential applications in electronic devices.

1. Introduction

Graphene has attracted enormous interests due to its novel electronic, thermodynamic and mechanical properties since it was first experimentally fabricated in 2004 [1]. The potential applications of graphene significantly depend on the surface wettability, which is mainly determined by the hydrophobic/hydrophilic character. It is well known that graphene is strongly hydrophobic. The hydrophobic graphene surface can reduce possible liquid deposition and prevents contamination of advanced nanoelectromechanical systems. However, controllable manipulation of the hydrophilic properties of graphene has plenty of applications, such as electrode materials of supercapacitors [2] and biomaterials supports [3].

Some groups have reported on controlling the hydrophilicity of graphene films by changing the concentration of water and acetone during synthesis [4]. However, the process mentioned above is complicated and needs further improvements. It is well known that doping of graphene is usually applied to tune the reactivity of graphene [5]. Since the H_2O molecule can dissociate on SiC, we expect that doping Si may induce the change of the wettability of graphene due to the production of hydrophilic OH group [6]. In this work, we perform a systematic density functional theory (DFT) calculations on the dissociative adsorption of a H_2O molecule on graphene doped with Si to understand the doping effect on the wettability of graphene.

2. Calculation methods

All calculations are implemented by Dmol^3 code [7]. The generalized gradient approximation (GGA) with Perdew-Burke-Ernzerhof (PBE) functional is employed to describe exchange and correlation effects [8]. A double numerical plus polarization (DNP) is employed as the basis set. The convergence tolerance of energy of 10^{-5} Ha is taken (1 Ha = 27.21 eV), and the maximal allowed force and displacement are 0.002 Ha and 0.005 Å, respectively. It was reported that the selection of exchange-correlation functional has small effect on the calculated energy barriers [9]. Linear synchronous transition/quadratic synchronous transit (LST/QST) [10] and nudged elastic band (NEB) [11] tools in Dmol^3 are used to investigate the minimum energy pathway for water dissociative adsorption on

* Corresponding author. Email: Zhimin.ao@uts.edu.au

graphene. The simulation cell consists of a 4×4 graphene supercell with a vacuum width of 20 Å above the layer to minimize the interlayer interaction. The *k*-point is set to be 5×5×1, and all atoms are allowed to relax according to previous reports. The DFT+D method within the Grimme scheme is used to consider the van der Waals forces [12].

For a H_2O adsorbed on graphene before and after dissociative adsorption, the adsorption energy E_{ad} is determined by,

$$E_{ad} = E_{H2O/graphene} - (E_{graphene} + E_{H2O}) \quad (1)$$

where $E_{H2O/graphene}$, $E_{graphene}$ and E_{H2O} are total energies of the H_2O/graphene system, the isolate graphene and a H_2O molecule in the same slab, respectively.

3. Results and discussion

3.1 The geometric structure of graphene

The atomic structure before and after Si doping is shown in Fig. 1. It is shown that the Si atom replaces one C atom and moves out of the plane graphene as shown in Fig. 1(b). The distance between dopant atom and graphene is h_{Si} = 1.20 Å, which is consistent with the reported result with h_{Si} = 1.457 Å [13]. The C-Si bond length is $l_{C\text{-}Si}$ = 1.76 Å, which was reported to be 1.767 Å [14]. In addition, Fig. 1 also shows the atomic charge near the doped Si atom obtained by Mulliken analysis. It is shown that the Si atom is positive charged and forms an electron–deficiency position. Therefore, Si atom changes the electron distribution in graphene, and thus changes the reactivity for the interaction between small molecules and graphene.

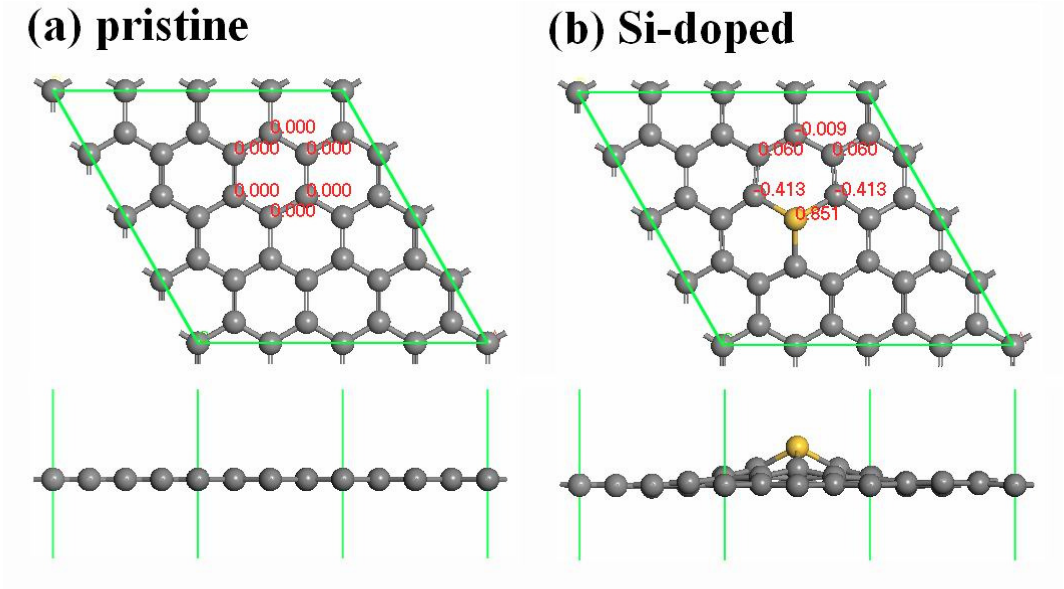

Fig. 1. The most stable configurations of pristine graphene (a), and Si-doped graphene (b). The atomic charge near the dopant obtained by Mulliken analysis is also given. The grey and yellow atoms are C and Si, respectively.

3.2 Dissociative adsorption of a H_2O molecule on pristine graphene

For a H_2O molecule adsorption on pristine graphene, the favorable adsorption site of the H_2O is at the hollow site with two OH bonds pointing down to the graphene surface with adsorption energy of –0.1 eV as shown in the Fig. 2(a), which is consistent with Ref. 15. This configuration is adopted as the initial structure in the subsequent transition state search calculations. For the H_2O dissociative adsorption on graphene, the most favorable

configuration is that H and OH are chemisorbed on the face-by-face carbon atoms in the six-member ring with adsorption energy of 2.5 eV, as shown as the FS in Fig. 2(a). After LST/QST and NEB calculations, it is found that the reaction barrier E_{bar} is 3.6 eV. This E_{bar} value is similar to the reported result of 3.599 eV [16]. Therefore, the dissociative adsorption of water on pristine graphene is difficult and the pristine graphene is strongly hydrophobic.

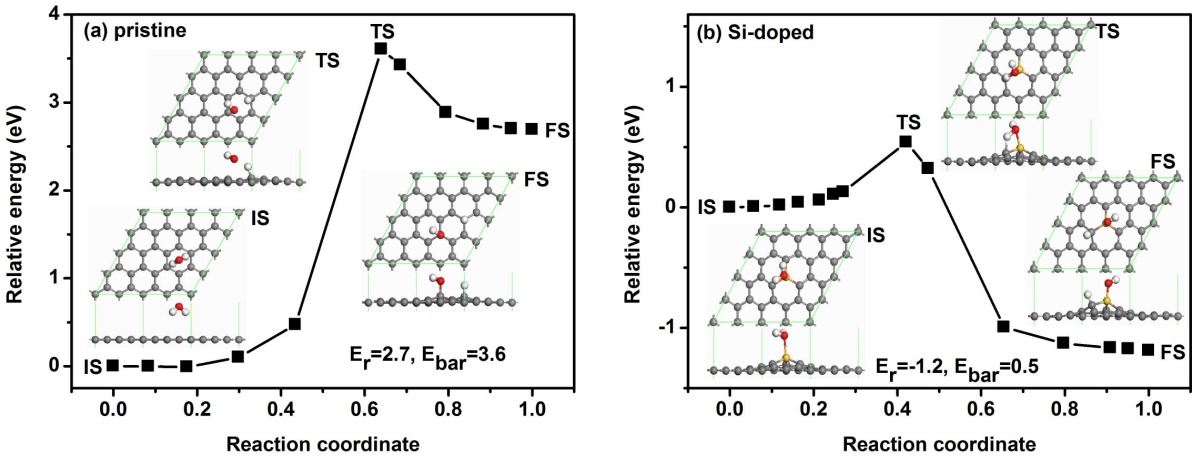

Fig. 2. The reaction pathway of a H_2O molecule dissociative adsorption on pristine and doped graphene. IS, TS and FS represent initial structure, transition structure and final structure, respectively. The energy of IS is taken to be zero. The units of E_{bar} and E_r are eV, where E_{bar} is the energy barrier and E_r is the reaction energy. The grey, white, red and yellow atoms are C, H, O, Si in this figure and below, respectively.

3.3 Dissociative adsorption of a H_2O molecule on Si-doped graphene

The obtained adsorption energy E_{ad_IS} between a H_2O molecule and the Si-doped graphene is -0.4 eV and the Si-O bond length D_{Si-O} is 2.126 Å, which indicates that the H_2O molecule chemically binds to the Si atom on Si-doped graphene as shown as IS in Fig. 2(b). This structure is the initial structure in the subsequent transition state search calculations as shown in Fig. 2(b). For the dissociative adsorption of H_2O molecule on the Si-doped graphene, the adsorption energy E_{ad_FS} for the dissociative chemical adsorption is -1.7 eV and this structure is the final structure (FS) in Fig. 2(b). It is found that the Si atom transfers electrons to the C atoms nearby and is positively charged as shown in Fig. 1(b), which is preferable for the adsorption of negatively charged OH. Meanwhile, C atoms near the dopant with negative charges are preferable for the adsorption of positively charged H atom, which makes the dissociative adsorption of the H_2O molecule on graphene more stable.

After LST/QST and NEB calculations, the detailed reaction pathway and the energy barrier for the dissociative adsorption of a H_2O molecule on the Si-doped graphene system is shown in Fig. 2(b). It is found that E_{bar} of the electron-deficiency system doped with Si dopant decrease from 3.6 eV in pristine graphene system to 0.5 eV. In addition, the reaction process is exothermic on Si–doped graphene with negative reaction energy E_r of –1.2 eV. It has been reported that surface reactions at ambient temperature may occur when $E_{bar} < 0.75$ eV [17]. We also consider the larger doping concentration of 12.5% with 2×2 graphene supercell, which shows that the dissociative energy barrier of H_2O on doped graphene is 0.6 eV. Under this doping concentration, the entire graphene surface can be considered being hydrophilic, while the basic lattice parameters of graphene remain. Therefore, doping Si into graphene can facilitate the dissociative adsorption of H_2O on graphene, which induces the transition of graphene from hydrophobic to hydrophilic spontaneously at room temperature.

4. Conclusion

In summary, the effect of Si dopant on the dissociative adsorption of H_2O molecules on graphene is investigated by using first principles calculations. The Si–doped graphene can efficiently decrease the dissociative barrier of H_2O molecules on graphene and change the wettability of graphene from hydrophobic to hydrophilic spontaneously at room temperature, which is important for its potential applications, such as in supercapacitors and biomaterials.

Acknowledgements
We acknowledge supports by National Key Basic Research, Development Program (Grant No. 2010CB631001) and China Scholarship Council (No. 201206170088). ZA acknowledges the finance supports from the Vice-Chancellor's Postdoctoral Research Fellowship Program of the University of New South Wales (SIR50/PS19184), and the Goldstar Award of the University of New South Wales (RG124422).

References
[1] Novoselov K S, Geim A K, Morozov S V, Jiang D, Zhang Y, Dubonos S V, Grigorieva I V and Firsov A A 2004 *Science* **306** 666.
[2] Stoller M D, Park S, Zhu Y, An J and Ruoff R S 2008 *Nano Lett.* **8** 3498.
[3] Chen H Q, Müller M B, Gilmore K J, Wallace G G and Li D 2008 *Adv. Mater.* **20** 3557.
[4] Rafiee J, Rafiee M A, Yu Z Z and Koratkar N 2010 *Adv. Mater.* **22** 2151.
[5] Ao Z M and Peeters F M 2010 *J. Phys. Chem. C* **114** 14503.
[6] Jiang Q G, Ao Z M, Chu D W and Jiang Q 2012 *J. Phys. Chem. C* **116** 19321.
[7] Delley B 2000 *J. Chem. Phys.***113** 7756.
[8] Perdew J P, Burke K and Ernzerhof M 1996 *Phys. Rev. Lett.* **77** 3865.
[9] Roldán A, Ricart J M and Illas F 2009 *Theor. Chem. Acc.* **123** 119.
[10] Halgren T A and Lipscomb W N 1977 *Chem. Phys. Lett.* **49** 225.
[11] Henkelman G and Jonsson H 2000 *J. Chem. Phys.***113** 9978.
[12] Grimme S 2006 *J. Comput. Chem.* **27** 1787.
[13] Dai J Y and Yuan J M 2010 *Phys. Rev. B* **81** 165414.
[14] Denis P A 2010 *Chem. Phys. Lett.* **492** 251.
[15] Li X, Feng J, Wang E G, Meng S, Klimeš J and Michaelides A 2012 *Phys. Rev. B* **85** 085425.
[16] Xu S, Irle S, Musaev D G and Lin M C 2005 *J. Phys. Chem. A* **109** 9563.
[17] Shang C and Liu Z P 2011 *J. Am. Chem. Soc.* **113** 9938.

A New Preparation Method to Significantly Improve the Photocatalytic Activity of ZnO Nanoparticles

Z.M. Xu,[a,b] J. Lu,[b,*] Z.M. Ao,[a,□] and S. Li[a]

[a] *School of Materials Science and Engineering, the University of New South Wales, NSW, 2052, Australia.*
[b] *Faculty of Science, Gansu Agricultural University, China.*

ZnO nanoparticles, which are considered as a photocatalyst for effluent degradation, are prepared by homogeneous precipitation and negative pressure baking at low temperature. The diameter of the ZnO nanoparticles is 16 ± 7 nm as determined by TEM. The results indicate that the usage of emulsifier in synthesis process can reduce the nanopartical aggregation and the low-temperature negative pressure baking method can avoid particle size expansion. Therefore, the ability of effluent degradation of the ZnO nanoparticles obtained by this method has been improved significantly.

1. Introduction

Metal-oxide photocatalysts are currently of great interest due to their potential application in degrading environmental organic contaminants and the conversion of solar-energy [1]. As a non-toxic, low cost and environmental friendly metal-oxide, ZnO is a wide gap oxide semiconductor, which is a promising photocatalyst. With a band gap of 3.2 eV, ZnO can be used to degrade organic effluent under visible light irradiation [2].

Among various methods of synthetising ZnO nanoparticles (ZnO-NPs), homogeneous precipitation method is one of the most widely used, because it provides an easier access to smaller, homogeneous nanoparticles with less impurity. Meanwhile, ZnO-NPs can be prepared in large scale at low cost and with simple requirements on reactors [3].

It is known that the activity of photocatalysis mainly relies on the shape and size distributions of ZnO [4]. Although ZnO-NPs are remarkable in photocatalyst, the particle aggregation and particle size expansion during baking process reduce the activity of photocatalysis. According to literature reports, the range of size of ZnO-NPs is from 20 to 50 [5]. Normally, the baking temperature is between 400 and 800℃ [5]. The high baking temperature is the main factor for the expansion. In order to prevent the ZnO nanoparticles aggregation and thus to improve the activity of photocatalysis, we provide two solutions: adding emulsifier in synthesis process and altering chemical equilibrium by negative pressure in low temperature baking process. Subsequently, Fourier transform infrared spectroscopy (FT-IR) and powder X-ray diffraction (XRD) are used to determine the presence of ZnO-NPs, and transmission electron microscopy (TEM) is used to determine the nanoparticle size distribution, and the activity of the photocatalyst is tested through degrading effluent.

2. Experimental

All the chemicals used in this work were of analytical reagent grade and used as received without further purification.

2.1 Preparation of ZnO-NPs

* Corresponding author. Email: lujunchem@163.com
□ Corresponding author. Email: Zhimin.ao@unsw.edu.au

$Zn(NO_3)_2{\cdot}6H_2O$ and urea are used as starting materials. 0.6 $molL^{-1}$ of $Zn(NO_3)_2$ solution was prepared by dissolving 35.7233 g of $Zn(NO_3)_2{\cdot}6H_2O$ in 200 ml ultra-purified water, and 2.1 $molL^{-1}$ of urea solution was prepared by dissolving 25.2276 g of urea in 200 ml ultra-purified water. The urea solution together with 0.4 ml of the Triton 100 (also known as emulsifier OP-10) was heated to 95°C while stirring. Subsequently, 200ml of $Zn(NO_3)_2$ solution was added into the mixed urea solution by drops with constant stirring by mechanical rabble (3000 rpm for 2h). Keep stirring for 3.5 h after $Zn(NO_3)_2$ solution added, a clear and homogenous non-aggregated basic zinc carbonate ($ZnCO_3{\cdot}2Zn(OH)_2{\cdot}H_2O$) was obtained as precursor [6].

When the mixed solution was cool, precursor was purified with ultra-purified water while vacuum filtrating and drying at 95 °C until no weight changed. After baking the precursor powder at 160 °C under negative pressure with vacuum degree of 0.08 MPa for 3h, non-aggregated ZnO-NPs with narrow diameter distribution can be obtained. In order to compare the photocatalytic activity of ZnO-NPs prepared by different methods, ZnO-NPs samples were prepared by repeating above experiment without adding Triton 100 and baking the precursor powder at 350℃ under atmospheric pressure for 3h according to traditional method [7]. The characterization of the prepared ZnO-NPs was taken by FT-IR, XRD and TEM.

2.2 Degradation of organic effluent

The degradation efficiency of ZnO-NPs to organic effluent was determined by chemical oxygen demand (COD) test with $K_2Cr_2O_7$.The organic effluent was supplied by Lanzhou Auxiliary Agent Plant, China. 1 g of non-aggregated ZnO-NPs was added into 200 ml of effluent sample and then the sample was exposed under the sun for 4h while stirring. After irradiation, effluent sample was centrifuged at 3000 rpm and decanted supernate was collected for further test. 0.50 ml effluent sample from supernate was diluted with 20 ml ultra-purified water and then adding 20 ml of 0.25 $mol{\cdot}L^{-1}$ $K_2Cr_2O_7$ solution. After adding 30 ml of concentrated sulphuric acid while stirring, the effluent sample was ready for redistilling, which took 2h. After redistilling and cooling, the treated effluent sample was diluted with ultra-purified water to 150 ml and then dropping 3 drops indicator of 1,10-Phenanthroline iron(II) sulphate solution. Titrated sample with ammonium iron(II) sulphate solution till the yellow sample solution turns reddish blue, the dosage of ammonium iron(II) sulphate solution was recorded as V_1.

Two blank samples were prepared for comparison. One contained ultra-purified water instead of effluent and the other one contained the traditional ZnO-NPs instead of non-aggregated ones. The dosage of ammonium iron(II) sulphate solution used in the blank was recorded as V_0. Then the COD and photodegradation rate can be determined by the equations as following,

$$\mathrm{COD} = (V_0\text{-}V_1)\, c\times 8\times 1000/V_2 \quad (1)$$

$$a = (n_0\text{-}n_x)/n_0 \times 100\% \quad (2)$$

where c is concentration of ammonium iron(II) sulphate solution, V_2 is the volume of effluent sample, a is photodegradation rate, n_0 is COD of original effluent (which is 120 $mg{\cdot}L^{-1}$), and n_x is COD of degraded effluent.

3. Results and Discussion

3.1 Fourier transforms infrared spectroscopy (FT-IR) analysis

Figure 1 shows the FT-IR result of the ZnO-NPs prepared by homogeneous precipitation method under negative pressure at 160 °C, in the range of 4000–400 cm^{-1}. A

broad absorption valley is observed at around 474.0 cm^{-1}, which indicates the existence of ZnO. There are several small absorption valleys at 1384.64, 1637.27, and 3469.31 cm^{-1}. These absorption bands are related to adsorption of CO_2 (C-O) and H_2O (O-H) from the atmosphere, and these therefore can be neglected. The FT-IR results show the high purity of the obtained ZnO-NPs.

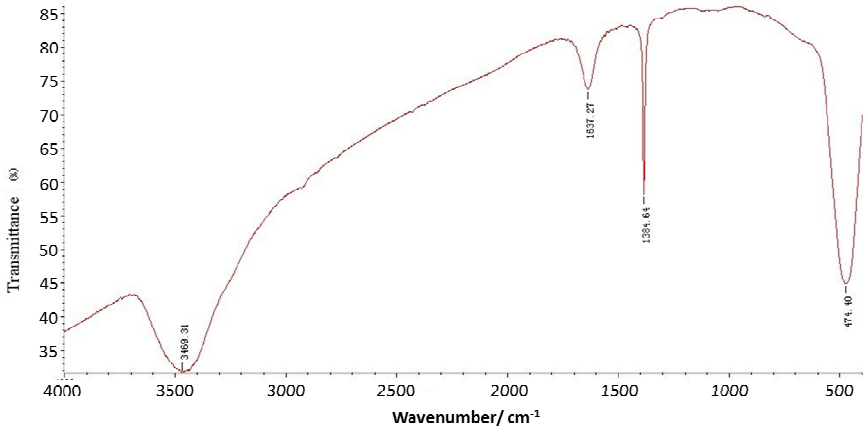

Fig. 1. The FT-IR spectroscopy pattern of the zinc oxide nanoparticles prepared by homogeneous precipitation method at 160°C under negative pressure

3.2 Powder X-ray diffraction (XRD) analysis

The XRD pattern of the ZnO-NPs prepared by homogeneous precipitation method under negative pressure at 160°C is shown in Figure 2. All the reflectance peaks can be indexed to ZnO structure (PDF code no: 00-036-1451). No diffractions from impurities appear in the XRD pattern, which show that ZnO-NPs were pure.

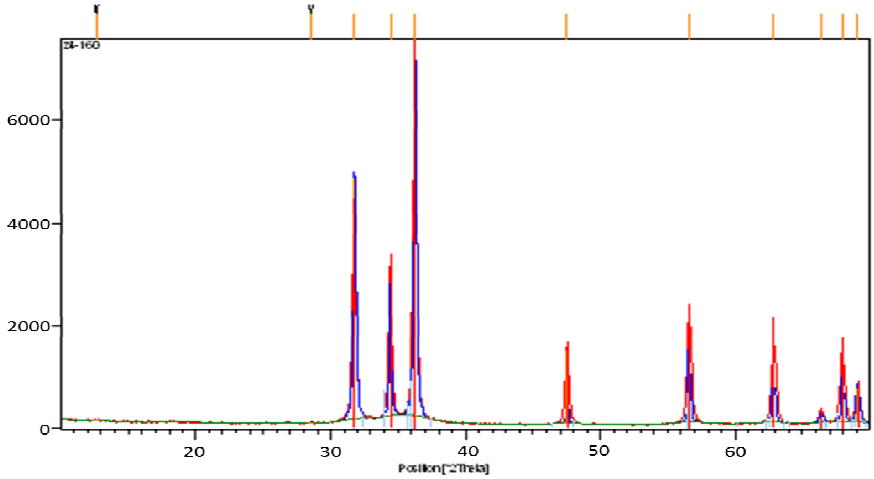

Fig. 2. The XRD pattern of the zinc oxide nanoparticles prepared by homogeneous precipitation method at 160°C under negative pressure

3.3 Transmission electron micrographs images

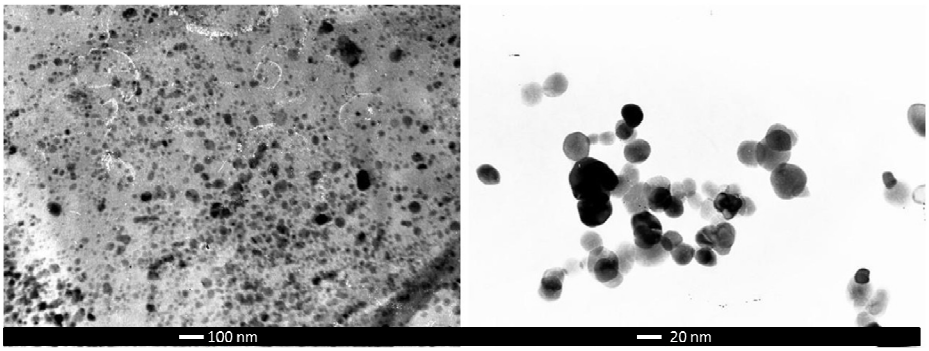

Fig. 3. The TEM images of the zinc oxide nanoparticles prepared by homogeneous precipitation method at 160°C under negative pressure. Scale bar of the images are 100nm (left) and 20nm (right), respectively.

The TEM images of the ZnO-NPs prepared by homogeneous precipitation method under negative pressure at 160 °C are provided in Figure 3, which indicates the narrow particle diameter distribution, and most of the particle size is in the range of 16 ± 7 nm.

3.4 Photocatalytic degradation of effluent

Effluent from Lanzhou Auxiliary Agent Plant, China was used as a test contaminant. Table 1 shows the photodegradation rate of the effluent samples with different ZnO-NPs powders as photocatalyst. COD and Photodegradation rate (*a*) were obtained by Eqs. (1) and (2). From the table, it is found that the photodegradation rate of effluent with non-aggregated ZnO-NPs as photocatalyst was 85.75%, while under the same situation, that with the traditional ones was 21.36%. It is found that non-aggregated ZnO-NPs prepared by homogeneous precipitation method at 160°C under negative pressure have high activity in photodegradation.

Table 1. The photodegradation rate of non-aggregated ZnO-NPs and traditional ZnO-NPs

Photocatalyst	Concentration	COD	Photodegradation rate
Non-aggregated ZnO-NPs	1.5g/L	1712	85.75%
Traditional ZnO-NPs	1.5g/L	9437	21.36%

4. Conclusion

The non-aggregated homogeneous ZnO-NPs with narrow diameter distribution were prepared by homogeneous precipitation method at 160 °C under negative pressure. The average particle size was 16 ± 7 nm. The XRD and FT-IR results confirmed the quality of the ZnO-NPs. Non-aggregated ZnO-NPs with narrow diameter distribution photocatalyst showed improved photocatalytic activity in degradation of effluent under visible light irradiation, which induced as much as 85.75% degradation of the effluent sample in 4h. All these indicated that non-aggregated ZnO-NP was a promising potential photocatalyst for the practical application in photodegradation of organic contaminants.

Acknowledgments

This work was supported by Faculty of Science, Gansu Agricultural University, China and the finance supports from the Vice-Chancellor's Research Fellowship Program of the University of New South Wales (SIR50/PS19184), and the Goldstar Award of the University of New South Wales (RG124422) are acknowledged.

References

[1] Sakthivel S 2003 *Solar Energy Materials and Solar Cells*. **77** 65
[2] Al-Momani F T E, Degorce-Dumas J R, Roussdy J and Thomas O J 2002 *Photochem. Photobiol. A: Chem.* **153** 191.
[3] Yu X 2012 *Materials Letters*. **86** 112
[4] U C S, L M G and HONG S S, 1997*J. Hwahak Konghak*. **35** 655.
[5] Wang X P and X.Y. 2010 *J. Guangdong Chemical Industry*. **37** 37.
[6] Deng H M 2001 *Journal of Materials Science*, **36** 3273.
[7] XIN X S, B B Z, LIU S Q, XIAO Z Y and LU S C 2002 *Chemistry and Adhesion* **1001** 203.

PROCEEDINGS - 37th ANNUAL CONDENSED MATTER AND MATERIALS MEETING, 5 - 8 February, 2013. Wagga Wagga, NSW, Australia

Exploiting Fitted Electric Field Gradient Parameters: Axis Ambiguity and the Asymmetry Parameter Constraint, $0 \leq \eta \leq 1$

G.A. Stewart

School of Physical, Environmental and Mathematical Sciences, UNSW Canberra, Australian Defence Force Academy, PO Box 7916, Canberra BC 2610.

Electric field gradient results derived from experimental nuclear quadrupole interaction data can appear deceptively straightforward. This paper explains the connection between the conventional frame (for which the asymmetry parameter lies between zero and unity) and its five perturbations. Consequences are illustrated through two case studies.

1. Introduction

In experimental hyperfine interaction techniques such as nuclear magnetic resonance and Mössbauer spectroscopy, it is common to fit the quadrupole interaction in terms of the electric field gradient (efg), $V_{ZZ} = \partial^2 V/\partial Z^2$, and the asymmetry parameter,

$$\eta = (V_{XX} - V_{YY})/V_{ZZ} \quad (1)$$

where η is constrained to lie within the range $0 \leq \eta \leq 1$. Implicit in this approach are two assumptions:

(i) *The axes, X, Y and Z, are the principal efg axes*. That is, when expressed with respect to this particular spatial alignment of axes, the 3 x 3 efg tensor is diagonalised.

(ii) *The principal efg axes are labelled to give* $|V_{ZZ}| \geq |V_{YY}| \geq |V_{XX}|$. It is only when this convention is satisfied that $0 \leq \eta \leq 1$. This frame will be referred to as the *conventional* frame.

How well the implicit axes are known depends on the local site symmetry of the probe atom. In the case of hexagonal, trigonal or tetragonal symmetries, the situation is clear. The principal Z-axis is the only axis of importance ($\eta = 0$) and it is aligned with the local symmetry axis. For orthorhombic symmetry, the three principal axes are aligned with the local 2-fold symmetry axes but the labelling that is consistent with $0 \leq \eta \leq 1$ is unknown. For lower symmetries, the spatial alignment of at least two of the three principal axes is also unknown, providing a complication further to the axis labelling ambiguity. Unless additional experimental information or theoretical calculations can be drawn on to resolve these issues, care must be taken when exploiting the fitted V_{ZZ} and η values in an alternative frame of reference.

2. The asymmetry parameter in alternative (non-conventional) frames

Bearing in mind that the efg tensor components are not influenced by axis sense, there are only 6 ways that the principal axes can be labelled (Fig. 1). The upper three coordinate frames in Fig. 1 represent the conventional frame, X Y Z, and its two cyclic permutations. The lower frames are generated from the upper frames by a simple rotation through $\pi/2$ about the Z′ axis. By combining Laplace's equation and the definition of the asymmetry parameter,

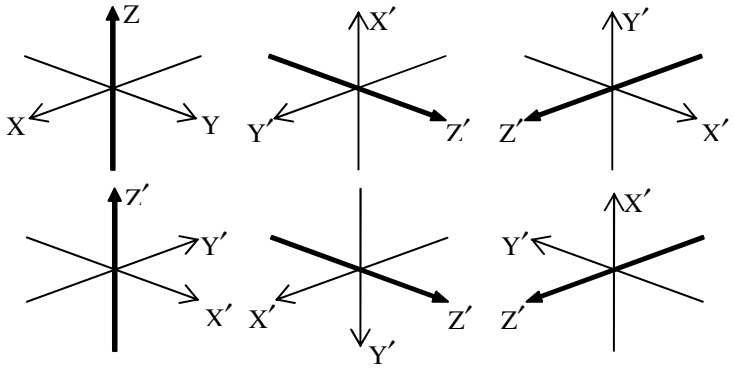

Fig. 1. Alternative axis labels for the same set of principal efg axes. The conventional frame (top left) is assumed to be labelled such that $|V_{ZZ}| \geq |V_{YY}| \geq |V_{XX}|$ with $0 \leq \eta \leq 1$.

it is straightforward to solve for the individual principal efg values in the conventional frame:

$$\left.\begin{array}{lcl} V_{XX} + V_{YY} + V_{ZZ} = 0 & \rightarrow & V_{XX} + V_{YY} = -V_{ZZ} \\ \eta = (V_{XX} - V_{YY})/V_{ZZ} & \rightarrow & V_{XX} - V_{YY} = \eta\, V_{ZZ} \end{array}\right\} \rightarrow \boxed{\begin{array}{lcl} V_{XX} & = & +\tfrac{1}{2}(\eta-1)\, V_{ZZ} \\ V_{YY} & = & -\tfrac{1}{2}(\eta+1)\, V_{ZZ} \\ V_{ZZ} & = & V_{ZZ} \end{array}} \qquad (2)$$

The left hand sides of the boxed expressions in (2) can then be relabelled as required and the $V_{Z'Z'}$ and η' expressions derived for the five alternative frames in terms of V_{ZZ} and η for the conventional frame. The resulting expressions are summarised in Table 1 and the values of η' are presented in Fig. 2 as a function of $0 \leq \eta \leq 1$ for the conventional frame. Based on the results provided in Table 1 and Fig. 2, it is observed that

(i) There is no constraint on the value of η' that might be calculated with respect to an arbitrary set of principal efg axes. It can range over all values from $-\infty$ to $+\infty$. However, the range that the calculated value falls into points to the relative orientation of the conventional frame via Fig. 2 coupled with Fig. 1.

(ii) As a special case, the calculated value of $\eta' = +3$ (-3) implies that $\eta = 0$ in the conventional frame with Z // Y′ (X′) as its symmetry axis.

(iii) The situations for the upper and lower coordinate frames shown in Fig. 1 differ only with respect to the sign of η'. That is, a coordinate rotation through $\pi/2$ about the Z′ axis serves only to change the sign of η'.

Table 1. Electric field gradient $V_{Z'Z'}$ and asymmetry parameter η' expressed in terms of their conventional frame values. The Euler angles α, β, γ correspond to the transformation from the conventional frame to the alternative frames (shown in Fig. 1).

X Y Z //	X′ Y′ Z′	-Y′ X′ Z′	Y′ Z′ X′	X′ Z′ –Y′	Z′ X′ Y′	Z′ -Y′ X′
α, β, γ	$0, 0, 0$	$0, 0, \frac{\pi}{2}$	$-\frac{\pi}{2}, -\frac{\pi}{2}, 0$	$-\frac{\pi}{2}, -\frac{\pi}{2}, \frac{\pi}{2}$	$0, \frac{\pi}{2}, \frac{\pi}{2}$	$0, \frac{\pi}{2}, \pi$
$V_{Z'Z'}/V_{ZZ}$	1	1	$-\frac{1}{2}(\eta+1)$	$-\frac{1}{2}(\eta+1)$	$\frac{1}{2}(\eta-1)$	$\frac{1}{2}(\eta-1)$
η'	η	$-\eta$	$\left(\frac{\eta-3}{\eta+1}\right)$	$-\left(\frac{\eta-3}{\eta+1}\right)$	$-\left(\frac{\eta+3}{\eta-1}\right)$	$\left(\frac{\eta+3}{\eta-1}\right)$

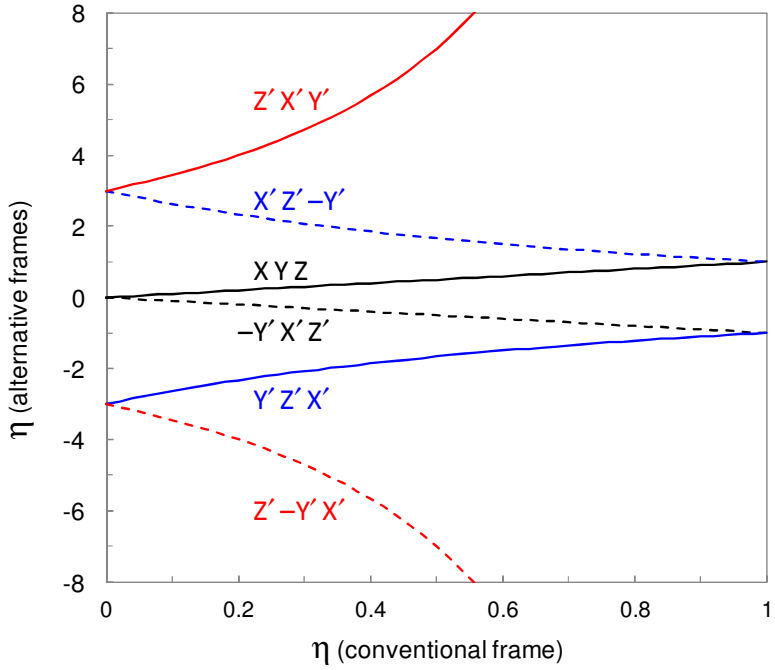

Fig. 2. The electric field gradient asymmetry parameter, η', for alternative frames is plotted as a function of its value in the conventional frame (for which $|V_{ZZ}| \geq |V_{YY}| \geq |V_{XX}|$ and $0 \leq \eta \leq 1$).

3. Applications in rare earth crystal field theory

The perturbative crystal field (CF) interaction of the local charge distribution with a rare earth ion's 4f shell is commonly represented as a multipole expansion of Stevens operator equivalents [1], $O_n^m(J)$,

$$\mathcal{H}_{CF} = \sum_{m=-2}^{+2} B_2^m O_2^m(J) + \sum_{m=-4}^{+4} B_4^m O_4^m(J) + \sum_{m=-6}^{+6} B_6^m O_6^m(J) \qquad (3)$$

and its characterization is then reduced to a matter of determining the sometimes considerable number of CF parameters B_n^m. A useful semi-empirical approach is to use

(i) theoretical calculations to estimate the higher rank ratios $r_4^m = B_4^m/B_4^0$ and $r_6^m = B_6^m/B_6^0$ so that only B_4^0 and B_6^0 need to be determined (fitted) independently, and

(ii) experimental quadrupole interaction determinations of the lattice efg components to estimate the rank 2 CF parameters

$$B_2^0 \propto V_{ZZ}^{latt} \quad \text{and} \quad B_2^2 = \eta^{latt} B_2^0 \qquad (4)$$

with respect to the conventional efg frame.

However, as emphasised in section 2, it is necessary to allow for the possibility that the axes implicit in (ii) may not align with those used for the theoretical calculation in (i).

3.1 Interpretation of inelastic neutron scattering results for intermetallic $ErNiAl_4$

In this recent example [2], cold source neutron inelastic neutron scattering (INS) was employed to determine the first three excited levels of the CF scheme for the single Er^{3+} site in $ErNiAl_4$ and then the semi-empirical approach described above was used to fit a preliminary set of CF parameters. For the orthorhombic C_{2v} (mm) site symmetry, the CF

Hamiltonian simplifies to

$$\mathcal{H}_{CF} = B_2^0O_2^0 + B_2^2O_2^2 + B_4^0O_4^0 + B_4^2O_4^2 + B_4^4O_4^4 + B_6^0O_6^0 + B_6^2O_6^2 + B_6^4O_6^4 + B_6^6O_6^6 \qquad (5)$$

as long as the coordinate axes X′ Y′ Z′ are chosen to align with the 2-fold symmetry axes (in this case, the crystallographic axes). Point charge model values of the higher rank ratios r_4^m and r_6^m were therefore calculated with respect to X′ Y′ Z′ // a b c. Experimental ^{155}Gd-Mössbauer results published earlier for isostructural $GdNiAl_4$ provided estimates of V_{ZZ}^{latt} and η^{latt} for the implicit conventional efg frame X Y Z. However, because of the labelling ambiguity described in Fig. 1, six possible sets of B_2^0 and B_2^2 were estimated using Table 1 and equation (4). Independent B_4^0/ B_6^0 grid searches were conducted for all 6 scenarios and the best set of CF parameters was found to correspond to X Y Z // a –c b. Planned thermal source neutron INS measurements should result in a further refinement of the set of CF parameters.

3.2 Analysis of ^{169}Tm-Mössbauer results for the "green phase" cuprate Tm_2BaCuO_5

In this second example [3], ^{169}Tm-Mössbauer spectroscopy was employed to monitor the temperature-dependent nuclear quadrupole splitting at the two Tm-sites of Tm_2BaCuO_5 (space group Pnma). A semi-empirical approach similar to that described for $ErNiAl_4$ in section 3.1 was then used to fit sets of CF parameters to the experimental data. However, the monoclinic C_s (m) site symmetry introduces an additional ambiguity. The CF Hamiltonian simplifies to

$$\mathcal{H}_{CF} = B_2^0O_2^0 + B_2^2O_2^2 + B_2^{-2}O_2^{-2} + B_4^0O_4^0 + B_4^2O_4^2 + B_4^{-2}O_4^{-2} + B_4^4O_4^4 + B_4^{-4}O_4^{-4} + B_6^0O_6^0 + B_6^2O_6^2 + B_6^{-2}O_6^{-2} + B_6^4O_6^4 + B_6^{-4}O_6^{-4} + B_6^6O_6^6 + B_6^{-6}O_6^{-6} \qquad (6)$$

as long as the Z′-axis is set perpendicular to the a-c mirror plane (i.e. parallel to the b axis). Although one of the principal efg axes must also align with the b-axis, the spatial orientation of the remaining two principal efg axes in the mirror plane is unknown. For each of the six possible sets of B_2^0 and B_2^2, an additional fit parameter, χ, was therefore needed to account for the angle of coordinate frame rotation about the b axis necessary to line up the efg principal axes and the CF theory axes in the mirror plane. This introduced the extra rank 2 CF parameter B_2^{-2} observed in (6) according to

$$(B_2^2)' = B_2^2\cos 2\chi \qquad \text{and} \qquad (B_2^{-2})' = -B_2^2\sin 2\chi \ . \qquad (7)$$

The best sets of CF parameters matched well with available optical spectroscopy and INS determinations of the lowest excited CF levels. They also led to useful predictions regarding low temperature induced Tm magnetisation.

4. Conclusion

This brief overview provides information in a user-friendly form designed to assist researchers endeavouring to exploit experimental efg results in an alternative frame of reference (i.e. a frame other than the conventional efg coordinate frame implicit in the asymmetry parameter condition that $0 \le \eta \le 1$).

References

[1] Rudowicz C 1985 *J. Phys. C* **18** 1415.
[2] Saensunon B, Stewart G A, Gubbens P C M, Hutchison W D and Buchsteiner A 2009 J.Phys.: Condens. Matter **21** 124215; 2010 J. Phys.: Condens. Matter **22** 029801.
[3] Stewart G A and Gubbens P C M 1999 J. Magn. Magn. Mater. **206** 17 - 26.

In Scotch Whisky, From Where are the Fe^{3+} and Cu^{2+} Ions Sourced?

S.C. Drew,[a] B. Roberts[a] and G.J.Troup[b]
[a] *Mental Health Research Institute, University of Melbourne, Victoria 3010, Australia*
[b]*School of Physics, Monash University, Victoria 3800, Australia.*

The distillate which becomes Single Malt Scotch Whisky has an Electron Paramagnetic Resonance (EPR) signal attributable to Cu^{2+} but no Fe^{3+} signal. After aging in used oak sherry barrels, the bottled product contains an additional Fe^{3+} signal at g ~ 4 appears. Spectra of the same product aged for different lengths of time were very similar. Are the barrels or the metals in the distilling apparatus the source? What happens with Brandy?

1. Introduction

A previous EPR study of Scotch whiskies [1] showed Fe^{3+} and Cu^{2+} signals, each whisky having a unique spectrum. The Fe^{3+} and Cu^{2+} have previously been attributed to the metals in the distilling vessels [1]. To check the consistency of a particular spectrum from different years, the present study compared specimens of the distillate (from 2008) before transfer to the aging process and of the aged whisky (before bottling) from two different years (1960 and 1970). Since once of us has also previously investigated brandies by EPR [2], we obtained similar specimens of two brandies for comparison. The consistency of the aged whisky spectra was good. The most interesting observations, however, were that Fe^{3+} and Mn^{2+} were detectable by EPR in final aged product but not in the distillate and that the Cu^{2+} ligand environment changed upon aging.

2. Methods and Sample Preparations

Double distilled brandy and whisky undergo similar preparations. The 'first' process is distilling the filtered liquid from the must/mash at least twice in a pot still, usually made of copper, or copper and stainless steel. Then the liquor was again twice distilled, and the final product placed in old oak sherry barrels (whisky) or old oak wine barrels (brandy). We examined the following specimens: (1) a 1960 and a 1970 whisky sample from each aging barrel and a 2008 final distillate prior to barrel ageing; (2) a ‘first’ (double) and ‘second’ (double) distillate for brandy.

Accurate metal concentration analysis was analysed by inductively-coupled plasma mass spectrometry (ICP-MS). Continuous-wave EPR spectra were obtained at X-band (9.45 GHz) using a Bruker E500 spectrometer fitted with a Bruker super-high-Q probe-head and a quartz cold finger insert (Wilmad, WG-816-B-Q). To increase the strength of the EPR signal, specimens were cold evaporated to dryness, then redissolved in a minimal volume of DMF. Samples were then transferred to 4 mm OD quartz sample tubes (Wilmad). The spectra are plotted as the usual first derivative of the microwave absorption. Unless otherwise indicated, experimental conditions were as follows: microwave power, 5 mW; magnetic field modulation amplitude, 4 G; field modulation frequency, 100 kHz; receiver time constant, 164 ms; sweep rate, 6.67 $G.s^{-1}$. Background correction was performed by subtraction of a third order polynomial.

Figure 1. Concentration of selected metal ions in distillate and aged whiskies produced in 1960 and 1970 from the same still.

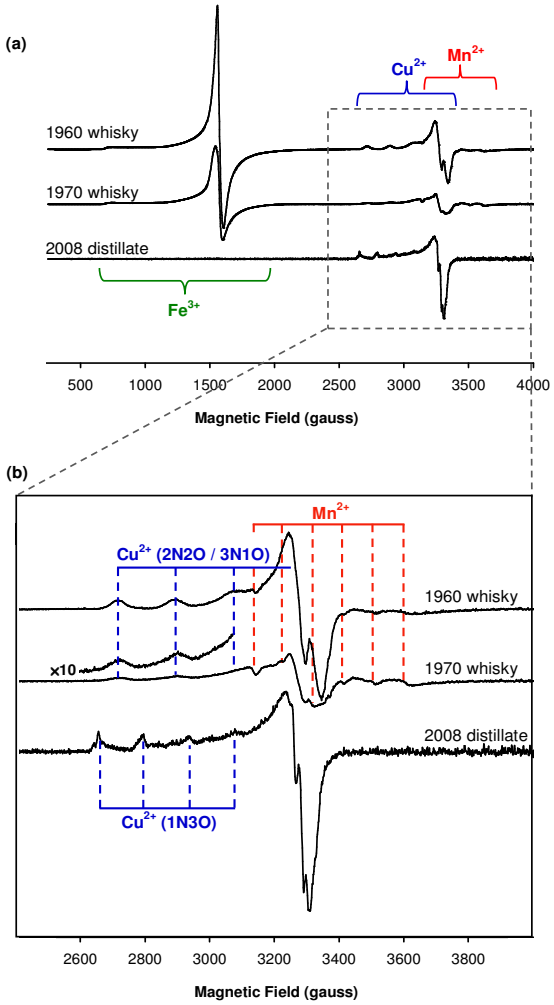

Figure 2. EPR spectra of a 2008 distillate and as-bottled aged whiskies from 1960 and 1970. The distillate shows no Fe^{3+} (500–2000 gauss) or Mn^{2+} (500–2000 gauss) signals, while the aged whiskies exhibit features characteristic of high-spin Fe^{3+}. Panel (b) is the same as panel (a) but with an expanded field scale. The spectrum of the 1970 whisky in the range 2600–3000 gauss is shown with an expanded intensity scale to enable clearer comparison with of the Cu^{2+} features. Dashed vertical lines are a guide to the eye to highlight the approximate positions of key spectral features of each

metal-bound species. The predicted number of nitrogen and oxygen ligands in each Cu^{2+} complex is indicated in parentheses. All spectra are normalised with the same intensity scale.

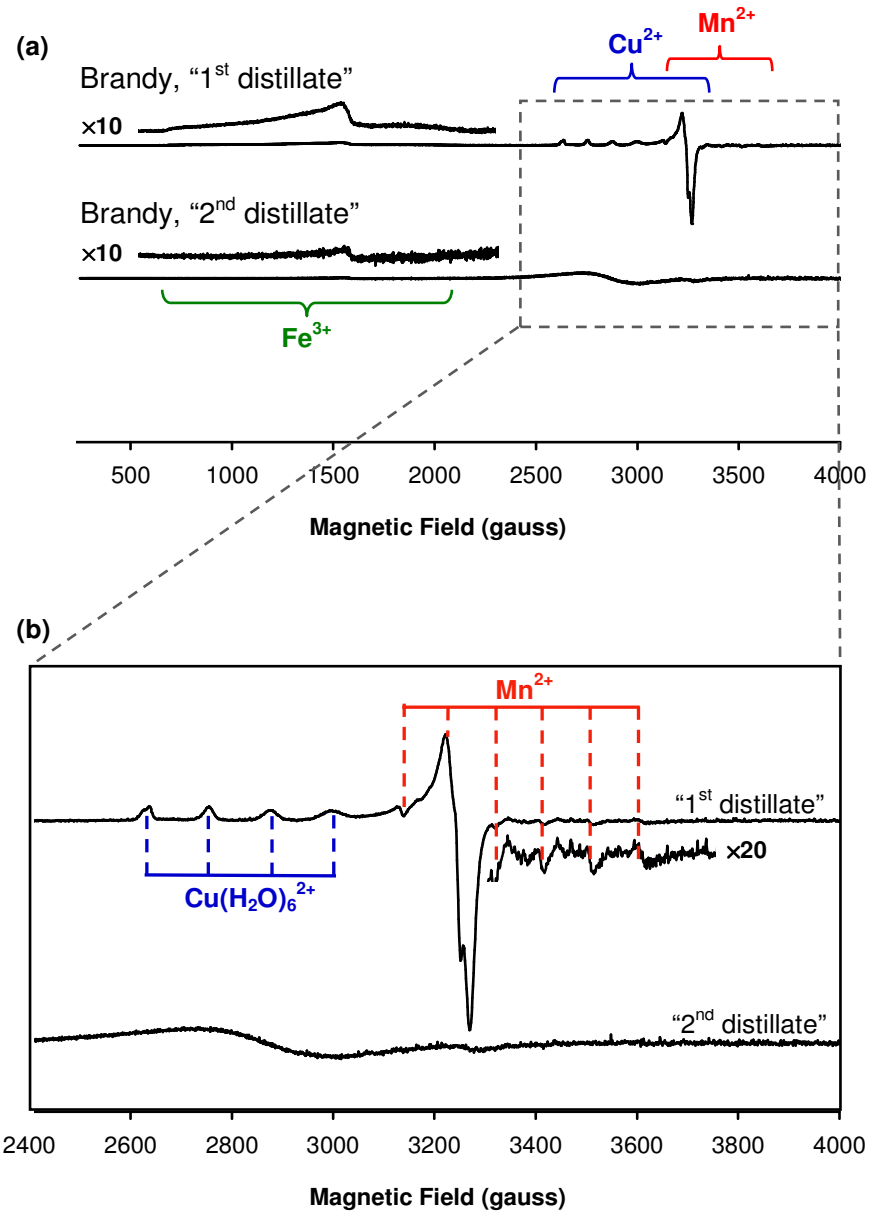

Figure 3. EPR spectra of a 'first' (double) and 'second' (double) distillate of brandy. Both distillates show relatively weak high-spin Fe^{3+} (500–2000 gauss) and Mn^{2+} (500–2000 gauss) signals. Panel (b) is the same as panel (a) but with an expanded field scale. Spectra are shown with expanded intensity scales as indicated to enable clearer identification of various features. Dashed vertical lines are a guide to the eye to highlight the approximate positions of key spectral features of each metal-bound species. The predicted number of nitrogen and oxygen ligands in each Cu^{2+} complex is indicated in parentheses. All spectra are normalised with the same intensity scale.

3. Results and Discussion

The ICP-MS analysis indicated substantial differences between the metal levels of the distillate and the final aged products; levels of copper in the distillate were 2–3 times higher than the aged products, whilst the levels of iron and manganese were greater than 20 times and 5 times lower, respectively (Fig. 1). Comparing the final aged products, the total zinc, iron and manganese levels were 20–30% higher in the 1960 whisky as compared with the

1970 whisky, whereas its copper levels were around 30% lower (Fig. 1). However, the relative intensity of the Cu^{2+} EPR spectra appeared to indicate the reverse (Fig. 2). Since any aqueous Cu^{+} and Fe^{2+} iron originating from the pot still would be oxidised to Cu^{2+} and Fe^{3+} upon exposure to an aerobic environment, this difference was unlikely due to the presence of "EPR-silent" Cu^{+} in solution. A close inspection of the Cu^{2+} spectral features indicated broader linewidths in the 1970 whisky sample (Fig. 2b), which would result in an apparent reduction in signal intensity (the EPR intensity depicts the first derivative of the microwave absorption, wherein narrower lines may appear more intense, although a true intensity comparison can only made after double-integration of the spectra). It is also possible that residual insoluble (and EPR-silent) metal-hydroxides were present in the dried films prior to reconstitution in DMF.

Referring to EPR spectra in Fig. 2b, the distillate exhibited a Cu^{2+} spectrum characteristic of square planar or tetragonal coordination by 1 nitrogen and three oxygen ligands (1N3O), whereas the aged whiskies contain Cu^{2+} in 2N2O or 3N1O coordination spheres [4]. The aged whisky spectra were very similar but subtly different. Due to the interference from the Cu^{2+} spectra, it was not possible to conclusively determine whether any significant spectral differences due to Mn^{2+} coordination were present in the aged whiskies. The relative intensity of the Fe^{3+} EPR spectra (Fig. 2a) was consistent with the total Fe levels measured by ICP-MS (Fig. 1). Both of the aged whiskies exhibited resonances at effective *g*-values in the range $g \sim 4–9$ (field values between ~500–2000 gauss), consistent with one or more high-spin Fe^{3+} centres possessing large zero-field splitting and a high rhombic distortion [5]. Some differences in linewidth were evident (eg. the strong feature near 1500 gauss in Fig. 2a) due to microheterogeneity of the Fe^{3+} coordination sphere and/or due to a combination of adventitious and bound high spin Fe^{3+}, whose EPR signatures are difficult to distinguish [5,6]. The lack of detectable Fe^{3+} and Mn^{2+} by EPR in the distillate was consistent with the relatively low total iron and manganese levels measured by ICP-MS (Fig. 1).

In the case of the two brandies, the same (low) copper and manganese levels were measured by ICP-MS (Fig. 1). Total iron and zinc levels were both >2 times higher in the 'first' (double) distillate compared with the 'second' (double) distillate. The EPR spectra (Fig.3) indicated that Cu^{2+} was unbound (aqueous) in the 'first' distillate [4], whereas only a broad, mostly featureless feature between 2000–4000 gauss was present in the spectrum of the 'second' distillate, possibly due to an insoluble Cu^{2+} species. The presence of Mn^{2+} could be identified in the 'first' distillate by EPR but not in the second. The Fe^{3+} spectra of both distillates were both characteristic of high-spin Fe^{3+}, although they appeared as almost pure absorption spectra rather than first-derivative due to rapid-passage effects. For similar reasons to above, it was not possible to identify clear spectral differences in Fe^{3+} coordination between the two distillates.

Acknowledgments

S.C.D. was supported by a Future Fellowship administered by the Australian Research Council.

References

[1] Cheah *et al.* 2003 *AIP CMM Conference proceedings* paper WW 03 21.
[2] Troup G J *et al.* 2006 *AIP CMM Conference proceedings* paper WP 31.
[3] Troup G J *et al.* 2008 *AIP CMM Conference proceedings* paper 28.
[4] Peisach J, Blumberg W E. *Arch. Biochem. Biophys.* **1974**, *165*, 691–698.
[5] Palmer G. *Biochem. Soc. Trans.* **1985**, *13*, 548–559.

[6] Cross M, Xiao Z, Maes E M, Czernuszewicz R S, Drew S C, Pilbrow J R, George G N, Wedd A G. *J. Biol. Inorg. Chem.* *7* **2002**, *7*, 781–790.

A Novel Multi-scale Modelling Approach for Determining the Bulk Properties of Difficult-to-Characterise Composites

P.J. Mignone[a,d,1], M. Wang[a,d], T.R. Finlayson[a,d], M.P. Echlin[c], A. Mottura[c], T.M. Pollock[c], D.P. Riley[b,d], G.V. Franks[a,d]

[a] *Department of Chemical & Biomolecular Engineering, The University of Melbourne, Victoria, 3010, Australia*
[b] *Australian Nuclear Science and Technology Organisation, Lucas Heights, NSW, 2234, Australia*
[c] *Materials Department, University of California – Santa Barbara, Santa Barbara, CA, 93106-5050, USA*
[d] *Defence Materials Technology Centre, Hawthorn, VIC, 3122, Australia*

A multi-scale modelling approach is presented for determining the bulk properties of copper-infiltrated Tungsten (W-Cu). A three-dimensional (3D) data-set of the W-Cu microstructure was generated using a novel serial-sectioning instrument. The image data were then reconstructed into a 3D Finite Element (FE) mesh. This made it possible to determine the bulk properties of W-Cu by simulating a representative volume of the microstructure.

1. Introduction

In many of today's cutting-edge engineering applications, the demand placed on the critical components of a system cannot be met by any single material or alloy. Future aerospace and energy technologies will require materials that can effectively manage and dissipate ultra-high temperatures (2000°C and higher), while retaining high thermo-mechanical strength over long time domains [1]. However, long lead times and high financial costs are typical during the development and certification stages of such materials [2].

Recent advances in microstructural imaging techniques, multi-scale computational modelling, and high-performance computing, have led to a drive towards implementing these methods into material development and certification processes. The ultimate objective is the reduction of experimentation costs and lead times required to bring ultra-high temperature materials to commercial applications. These computational techniques require significant financial investment and time to develop expertise. More importantly, accurate image-processing and FE meshing of the material microstructure are critical for numerically correct results, and require best-practice techniques to control [3].

In addition, the 3D microstructure of some materials is difficult to characterise (DTC) using traditional x-ray tomography (μCT) techniques. X-ray absorption makes the characterisation of highly dense materials (e.g. tungsten) impractical with low-energy μCT. Neutron tomography is currently not an alternative as it lacks the resolution to characterise fine-grained microstructures (Fig. 1) [4].

[1] mignonep@unimelb.edu.au

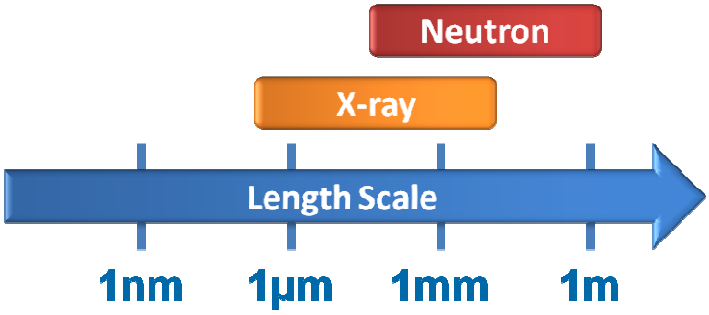

Fig. 1: Resolutions of x-ray and neutron tomographic techniques

The following research presents a technique for characterising microstructural data and generating FE meshes for determining the bulk mechanical properties of DTC composite microstructures. The 3D microstructural data of W-Cu, a candidate material for high-temperature applications, were generated using serial-sectioning and image-processing techniques. The image data were then reconstructed into a 3D FE mesh using iso2mesh (i2m), an open-source meshing library traditionally used in medical applications [5]. A mesh-sensitivity study was conducted on this microstructure using i2m, and compared against Simpleware (SIP), a commercial mesh generator, via the Finite Element Method (FEM).

2. Methodology

A sample of W-Cu (15wt% Cu) was obtained from Plansee, a manufacturer of high-performance, refractory-metal components [6]. The material was created using the infiltration technique. The exact infiltration process and its parameters for this sample are propriety to Plansee and not known for this investigation. A typical infiltration process to create W-Cu composites of 98-99% density is outlined in the literature [7]. To obtain the 3D dataset of the W-Cu microstructure, the use of non-destructive techniques, such as low-energy x-ray or neutron tomography, is currently impractical. However, destructive techniques (i.e., serial-sectioning) whereby material is removed and images are taken to build the 3D dataset are a viable alternative. For this investigation, the sample was placed in a new serial sectioning device called the TriBeam [8], which combines a femtosecond laser with a Focused Ion Beam (FIB) and a Scanning Electron Microscope (SEM). This allows for the fast acquisition of 3D microstructural data sets.

The TriBeam uses a femtosecond laser to ablate the top surface of the sample at 250 nm intervals. Between each interval or ‘slice’, the sample is tilted so that the ablated surface is normal to the electron beam. A two-dimensional (2D) secondary-electron image is then collected from the recently ablated sample surface. The process is continued to produce a stack of secondary electron images through the sample thickness. On completion of the data collection, further image processing was required to characterise accurately the microstructure before FE meshing and simulation. Individual images in the stack were aligned to correct for any planar displacement during sample rotation towards the electron beam. Image filters were used to remove image artefacts, and to define clearly the separate copper and tungsten material phases. The modified image stack was then converted into a black/white (i.e. binary) image. Fig. 2a shows a 25µm x 25µm x 25µm sample stack of W-Cu (with 15% wt Cu), that was used for further analysis.

The image stack was imported into Matlab as a 3D image array. Iso2mesh was used to convert the 3D image array into an all-tetrahedron mesh (Fig. 2b). Simpleware meshes were generated using its proprietary mesh algorithm and graphical user interface. The meshes were

then imported into Abaqus 6.11-1 for Finite Element Analysis (FEA) simulations. The tungsten Young's modulus and Poission's ratio used for the simulations were 408.0 GPa and 0.28, respectively [9]. The copper Young's modulus and Poission's ratio used for the simulations were 129.8 GPa and 0.34, respectively [9]. Periodic (i.e., symmetry) boundary conditions are applied to fix the model in 3D space. A known, compressive displacement is applied to the model to obtain the reaction force and displacement output. Hooke's law is then used to determine the Young's modulus.

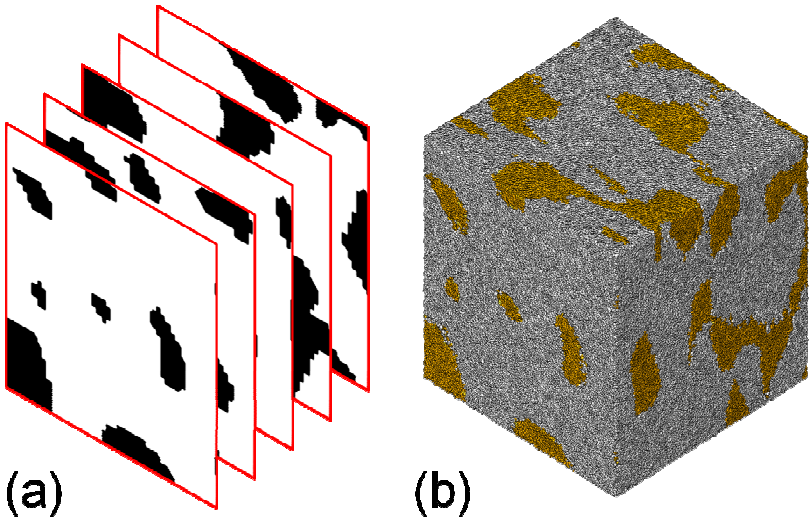

Fig. 2: (a) Binarised microstructure showing Tungsten (white) and Copper (black) phases. (b) Microstructure converted into a FE mesh.

3. Results & Discussion

Fig. 3 shows the average Young's modulus comparison between the Simpleware and iso2mesh meshing techniques at different levels of mesh refinement. For the Simpleware result, as the model size increases, there is a slight drop in the Young's modulus value. This shows a small, yet present amount of mesh sensitivity in the model as the model size is increased from 800,000 to 1.6 million elements. The change in result is less than 0.5% between coarse- and fine-mesh results, indicating Simpleware's capability in accurately capturing the microstructure at its most-coarse mesh generation settings.

The iso2mesh result shows a similar relationship between Young's modulus and mesh refinement, with less than a 0.5% change between coarse- and fine-mesh results. An exception exists however, when the iso2mesh models use coarse meshes (i.e., 800,000 to 1 million elements). In this region the Young's modulus result peaks at approximately 1 million elements before dropping in value. This small change is possibly due to how iso2mesh approximates the microstructure at coarse mesh values. The effect however is negligible and disappears when the mesh density is increased.

Table 1 shows a summary of the most coarse (800,000 elements approx.) and most fine (6.5 million elements approx.) Simpleware (SIP) and iso2mesh (i2m) mesh results, and compares them with analytical and literature-based results. The theoretical result was calculated using the rule of mixtures [10]. The coarse and fine results of both mesh techniques are within 0.2% of the official result for W-Cu (15wt% Cu) in Plansee literature, indicating the robustness of the multi-scale modelling approach. A 7% variation between the FE results and theory is also observed. However, the rule of mixtures is an ideal calculation and does not consider factors such as material morphology, which can significantly affect material properties.

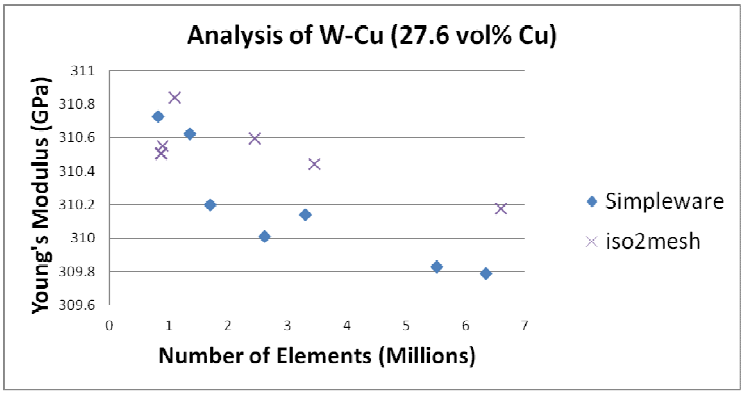

Fig. 3: Average Young's modulus comparison between the Simpleware and iso2mesh techniques.

W-Cu Result	Young's modulus (GPa)
Theory	331.20
Plansee [6]	310.00
i2m (Coarse)	310.51
i2m (Fine)	310.18
SIP (Coarse)	310.73
SIP (Fine)	309.59

Table 1: Summary of Simpleware and iso2mesh results.

4. Conclusion

The variations of results were found to be less the 0.5% at different mesh densities for both meshing techniques. This indicates that both iso2mesh and Simpleware are capable of calculating the bulk mechanical properties of microstructures at reasonably coarse mesh densities. This would be ideal for the simulation of larger samples, such as would be required for representative volume-element studies. Future research is currently investigating this. Both mesh techniques generated mechanical properties within 7% and 0.2% of the theoretical and literature-based results, respectively. While further research is required, iso2mesh has shown significant capability as an open-source alternative for low-cost pre-processing of complex material microstructures.

Acknowledgments

We should like to thank the Defence Materials Technology Centre (Project 4.2) for their technical and financial support for this research. We should also like to thank the support staff at the Materials Department in the University of California Santa Barbara, for their efforts in preparing and sectioning material samples with their TriBeam system. Finally we should like to thank Mr. Jamie Whiteford from BAE Systems Australia for providing the W-Cu materials used in this research.

References

[1] S.J. Zinkle, J.T. Busby, Materials Today, 12 (2009) 12-19.
[2] P.D. Mangalgiri, Bull Mater Sci, 22 (1999) 657-664.
[3] J. Mackerle, Finite Elements in Analysis and Design, 15 (1993) 177-188.
[4] J. Banhart, Advanced tomographic methods in materials research and engineering, Oxford University Press, 2008, Chapter 1.
[5] F. Qianqian, D.A. Boas, Biomedical Imaging: From Nano to Macro, 2009. ISBI '09. IEEE International Symposium on, 2009, pp. 1142-1145.
[6] http://www.plansee.com/
[7] J. Das, A. Chakraborty, T.P. Bagchi, B. Sarma, International Journal of Refractory Metals and Hard Materials, 26 (2008) 530-539.
[8] M.P. Echlin, A. Mottura, C.J. Torbet, T.M. Pollock, Review of Scientific Instruments, 83 (2012) 023701-023706.
[9] P. J. Karditsas, M. J. Baptiste, Website, http://aries.ucsd.edu/LIB/PROPS/PANOS/ (23/02/2013).
[10] M.F. Ashby, D.R.H. Jones, Engineering Materials 2: An Introduction to Microstructures, Processing and Design, Elsevier Science, 2005, Chapter 25.

PROCEEDINGS - 37th ANNUAL CONDENSED MATTER AND MATERIALS MEETING, 5 - 8 February, 2013. Wagga Wagga, NSW, Australia

The Effect of Fe and Ni Substitution in Magnetocaloric MnCoGe

Q. Y. Ren[a], W. D. Hutchison[a], J. L. Wang[b,c], W. Kemp[a], R. Cobas[a], J. M. Cadogan[a] and S. J. Campbell[a]

[a] *School of Physical, Environmental and Mathematical Sciences, The University of New South Wales, Canberra, ACT 2600*
[b] *Institute for Superconductivity and Electronic Materials, University of Wollongong, Wollongong, NSW, 2522*
[c] *Bragg Institute, Australian Nuclear Science and Technology Organisation, Lucas Heights, NSW, 2234*

The MnCoGe family of compounds shows potential as a rare-earth free material for magnetocaloric applications around room temperature. We present initial findings on the effects of the substitution of Fe and Ni for Mn in a series of $Mn_{1-x}T_xCoGe$ compounds (T = Fe, Ni; x = 0.04 - 0.10). Investigations include x-ray diffraction, differential scanning calorimetry(200 - 670 K) and magnetisation (5 - 350 K) measurements in magnetic fields up to 8 T. The influence of the Fe and Ni substitutions on the transformation temperature between the hexagonal and orthorhombic structures, the resultant phase fractions and their magnetic phase transitions are reported.

1. Introduction

Materials which utilise the magnetocaloric effect (MCE) have attracted increasing attention in the past two decades due to the promise of refrigeration applications as an alternative to conventional vapour-cycle systems with the prospects of energy savings and environmentally friendly technology [1]. In particular, the work of Pecharsky and Gschneidner [2] reported in 1997 offered scope for applications around room temperature. Many systems have been explored since then including $Gd_5Ge_2Si_2$ [2], $LaFe_{11.4}Si_{1.6}$ [3] and $NdBaMn_2O_6$ [4].

MnCoGe also exhibits transitions around room temperature and, given that it comprises relatively low cost materials, systems based on MnCoGe have also attracted attention [5-7]. MnCoGe can form in two crystal structures [8]: an orthorhombic TiNiSi-type structure (space group P*nma*) with a Curie temperature T_C^{orth} = 345 K [5]; and a hexagonal Ni_2In-type structure (space group P6_3/*mmc*) with a Curie temperature T_C^{hex} = 275 K [9]. With decreasing temperature, MnCoGe shows a diffusionless transformation from the austenitic hexagonal phase to the martensitic orthorhombic phase at T_{str} ~ 650 K [10]. T_{str} can be controlled in a variety of ways including: pressure [11], introduction of substitutional [12] or interstitial atoms [13], leading to the observation of first order phase transitions (FOPT) in several MnCoGe-based systems [14-16]. For materials with a FOPT, a magnetic field can simultaneously change the magnetic and lattice entropies due to the coupling between the crystallographic structure and the magnetism and hence may exhibit a giant magnetocaloric effect (GMCE). Here, we report the initial findings of our attempt to tune the T_{str} of $Mn_{1-x}Fe_xCoGe$ and $Mn_{1-x}Ni_xCoGe$ compounds in order to create a first order phase transition.

2. Sample preparation

The polycrystalline $Mn_{1-x}Fe_xCoGe$ and $Mn_{1-x}Ni_xCoGe$ samples (x= 0.04, 0.06, 0.08, 0.10) were prepared by repeated argon-arc melting of stoichiometric amounts of 99.9% pure Mn, Co, Ge plus 99.99% Fe and Ni. The mass loss of Mn during melting was compensated by adding 3% excess Mn to the starting materials. The resulting ingots were wrapped in tantalum

foil and sealed in evacuated quartz tubes, then annealed at 850°C for five days followed by quenching in water. The samples were characterised by powder x-ray diffraction measurements at room temperature (XRD; CuKα radiation). The magnetisation was measured in magnetic fields of 0.01 T in both zero field cooling (ZFC) and field cooling (FC) modes over the temperature range from 5 K to 350 K using a Physical Properties Measurement System (Quantum Design PPMS). In addition, the field dependence of the magnetisation was measured in magnetic fields up to 8 T, from 200 K to 350 K in steps of 5 K. Several samples were also investigated by differential scanning calorimetry (DSC) measurements from 200 K to 670 K.

3. Results and Discussion

3.1 Structures; Phases

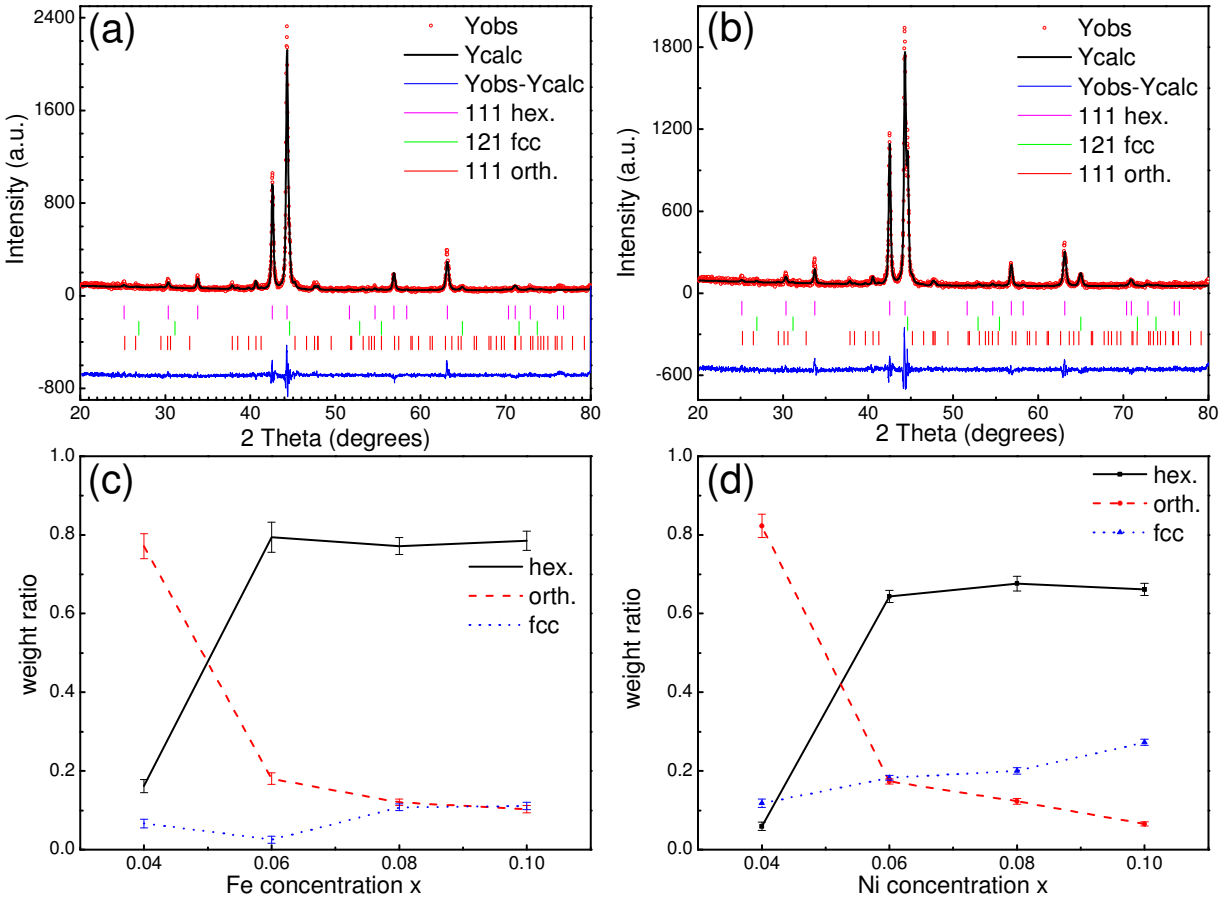

Fig. 1 X-ray diffraction patterns and Rietveld refinements (see text) for: (a) $Mn_{0.92}Fe_{0.08}CoGe$ and (b) $Mn_{0.90}Ni_{0.10}CoGe$; individual phase contents ("weight ratio") as functions of dopant concentration for: (c) $Mn_{1-x}Fe_xCoGe$ and (d) $Mn_{1-x}Ni_xCoGe$

The x-ray diffraction Rietveld refinements (using FullProf) of $Mn_{0.92}Fe_{0.08}CoGe$ and $Mn_{0.92}Ni_{0.08}CoGe$ are shown in Figs. 1(a) and 1(b) respectively with both systems found to exhibit coexistence of the hexagonal and orthorhombic phases as expected. This phenomenon indicates that the transformation temperature is around room temperature. However, an impurity phase identified as $MnCo_2Ge$ (fcc structure, space group F*m-3m*) is also observed in both systems. As shown by Figs. 1(c) and 1(d), the $MnCo_2Ge$ phase is more pronounced in $Mn_{0.90}Ni_{0.10}CoGe$ than in $Mn_{0.92}Fe_{0.08}CoGe$. The preliminary assumption is that Ni shows a

greater preference than Fe to enter into the Co site in $MnCo_2Ge$ rather than the Mn site in MnCoGe.

The fraction of the three phases identified in $Mn_{1-x}Fe_xCoGe$ and $Mn_{1-x}Ni_xCoGe$ - hexagonal, orthorhombic and $MnCo_2Ge$ - are shown as functions of Fe and Ni concentrations in Figs. 1(c) and 1(d) respectively. The hexagonal phase is found to increase with increasing Fe and Ni concentrations while the orthorhombic phase decreases. This implies that T_{str} is reduced with increasing Fe or Ni content. The fraction of the fcc $MnCo_2Ge$ phase present in the $Mn_{1-x}Fe_xCoGe$ system remains relatively low (< 11(1) %) with increases in x while the fraction of the fcc $MnCo_2Ge$ in $Mn_{1-x}Ni_xCoGe$ increases from ~ 12(1) % to ~ 27(1) %. The $MnCo_2Ge$ phase is likely to have occurred during the sample preparation process, when the arc beam encounters the raw materials, causing a dispersal of the Ge powder. The loss of Ge drives $Mn_{1-x}T_xCoGe$ towards the $MnCo_2Ge$ structure. To avoid this problem in future sample preparations, the Ge powder will first be melted to solid form.

3.2 Magnetic properties

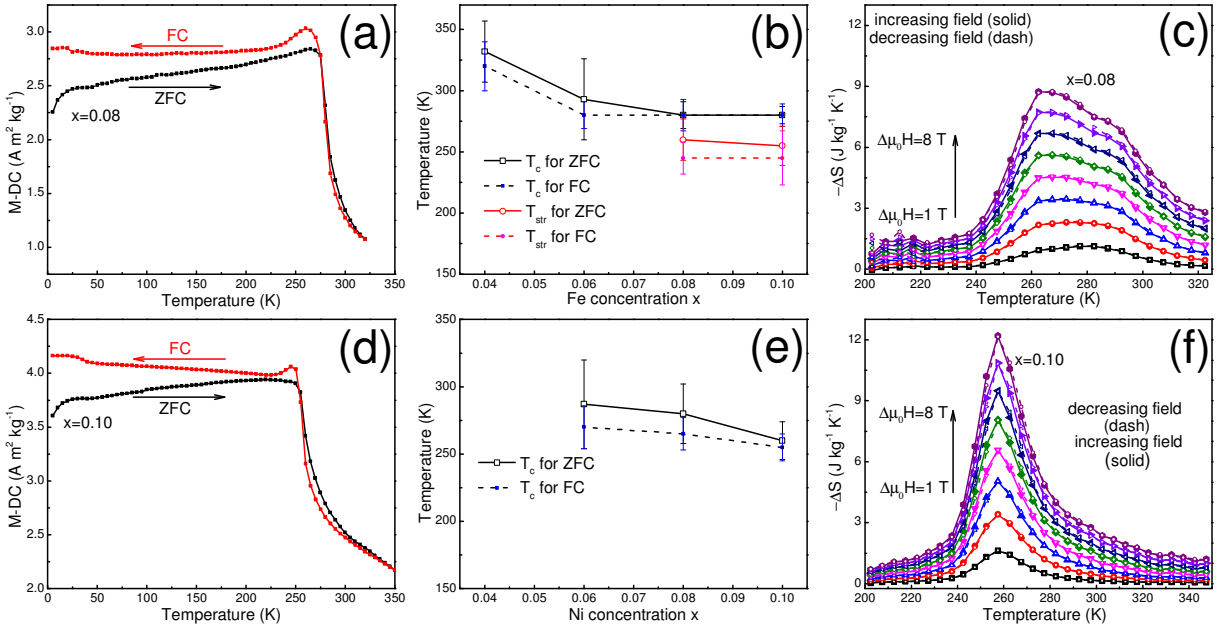

Fig. 2 Magnetic data for $Mn_{1-x}Fe_xCoGe$ ((a), (b), (c)) and $Mn_{1-x}Ni_xCoGe$ ((d), (e), (f)): (a) and (d) M-T curves (B=0.01 T); (b) and (e) transition temperatures (determined from dM/dT curves) versus Fe and Ni concentrations; (c) and (f) isothermal entropy changes. ($\Delta\mu_0H$ = 1 T to 8 T in (c) and (f); the data points are linked by straight lines as a guide to the eye.)

The magnetisation curves for $Mn_{0.92}Fe_{0.08}CoGe$ and $Mn_{0.90}Ni_{0.10}CoGe$ are shown as a function of temperature in Figs. 2(a) and 2(d). The magnetisation does not tend to zero beyond the main magnetic phase transition up to 350 K. This is attributed to the existence of the fcc phase. The transition temperatures obtained by differentiation of the M-T curves are summarized in Figs. 2(b) and 2(e). For $Mn_{1-x}Fe_xCoGe$ (x = 0.04 and 0.06) there is only one transformation. For each transformation, however, two different temperature points were obtained according to the splitting between the ZFC and the FC curves around the magnetic transition temperature, which indicates the presence of thermal hysteresis [17, 18]. In many magnetocaloric materials [2, 12, 19], such hysteresis implies the existence of FOPT due to the combination of magnetic and structural transitions. For $Mn_{1-x}Fe_xCoGe$ with x = 0.08 and 0.10 two transitions are observed up to 350 K; the transitions around 280 K most likely indicate the magnetic transition of the hexagonal phase for both samples with the lower transitions around 260 K and 255 K, respectively, being due to transformation to the orthorhombic structure. In

contrast, only one transition temperature (FOPT) is observed up to 350 K for each of the $Mn_{1-x}Ni_xCoGe$ samples.

The isothermal entropy changes -ΔS for $Mn_{0.92}Fe_{0.08}CoGe$ and $Mn_{0.90}Ni_{0.10}CoGe$ derived from the magnetisation versus field curves (T = 200 - 350 K; B = 0 - 8 T; not shown) are shown in Figs. 2(c) and 2(f) respectively. The entropy changes were calculated using the standard Maxwell function (see e.g. [20]). $Mn_{0.92}Fe_{0.08}CoGe$ exhibits two peaks in -ΔS ~ 5.6 J/kg·K at ~ 262 K and ~ 5.0 J/kg·K at ~ 283 K for ΔB = 0 - 5 T. The isothermal entropy change for $Mn_{0.90}Ni_{0.10}CoGe$ is -ΔS ~ 8.0 J/kg·K at ~258 K (ΔB = 0 - 5 T).

3.3 Differential Scanning Calorimetry

DSC curves for $Mn_{0.92}Fe_{0.08}CoGe$ and $Mn_{0.90}Ni_{0.10}CoGe$ are shown in Figs 3(a) and 3(b) respectively. Preliminary analyses (e.g. inserts to Fig. 3) indicate two transitions, ~ 292 K and ~267 K, within the range 200-350 K for $Mn_{0.92}Fe_{0.08}CoGe$, compared with ~ 270 K and ~ 250 K as indicated by the magnetic measurements (Fig. 2(b)) with a single transition ~ 258 K for $Mn_{0.90}Ni_{0.10}CoGe$ as also observed in magnetic measurements (~ 265 K; Fig. 2(e)). Differences in transition temperatures are probably associated with differences between the rates at which the magnetic and DSC measurements were carried out.

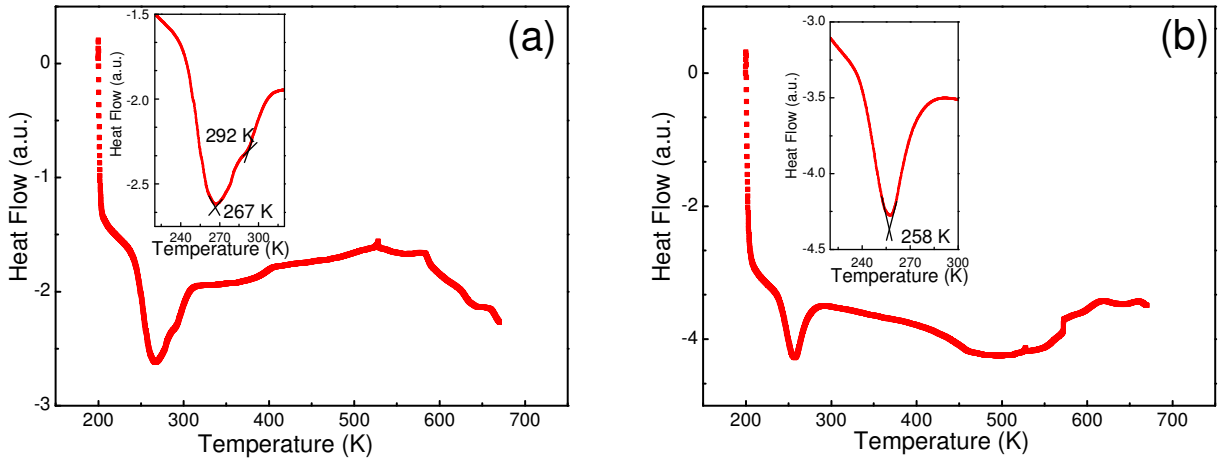

Fig. 3 DSC curves for (a) $Mn_{0.92}Ge_{0.08}CoGe$ and (b) $Mn_{0.90}Ni_{0.10}CoGe$ with insets showing the preliminary analyses of the transition temperatures.

4. Conclusions

The effects of substituting Fe and Ni atoms for Mn on the structural and magnetic transitions in $Mn_{1-x}Fe_xCoGe$ and $Mn_{1-x}Ni_xCoGe$ (x = 0.04 - 1.0) have been investigated over the temperature range 5 - 350 K by x-ray diffraction, magnetisation and DSC measurements. The impurity phase $MnCo_2Ge$ was obtained in all samples. The isothermal entropy changes for $Mn_{0.92}Fe_{0.08}CoGe$ are -ΔS ~ 5.6 J/kg·K at ~ 262 K and ~ 5.0 J/kg·K at ~ 283 K and for $Mn_{0.90}Ni_{0.10}CoGe$ -ΔS ~ 8.0 J/kg·K at ~ 258 K (ΔB = 0 - 5 T). Investigations are continuing to obtain samples free of $MnCo_2Ge$ and to obtain combined magnetic and structural entropy changes around a common transition temperature to maximise the magnetocaloric effects.

Acknowledgments

This work is supported in part by the Australian Research Council (DP110102386; LE1001000177). Q.Y. Ren is supported by a UNSW Canberra Research Training Scholarship. The authors thank Mr. M.F. Md Din, University of Wollongong, for carrying out the DSC measurements.

References

[1] Brück E, 2005 *J. Phys. D: Appl. Phys.* **38** R381
[2] Pecharsky V K and Gschneidner J K A, 1997 *Phys. Rev. Lett.* **78** 4494
[3] Hu F-x, Shen B-g, Sun J-r, Cheng Z-h, Rao G-h and Zhang X-x, 2001 *Appl. Phys. Lett.* **78** 3675
[4] Zhang Q, Guillou F, Wahl A, Bréard Y and Hardy V, 2010 *Appl. Phys. Lett.* **96** 242506
[5] Song L, Tegus O, Brück E, Dagula W, Gortenmulder T J and Buschow K H J, 2006 *Magnetics, IEEE Transactions on* **42** 3776
[6] Zhang C L, Wang D H, Cao Q Q, Han Z D, Xuan H C and Du Y W, 2008 *Appl. Phys. Lett.* **93** 122505
[7] Shamba P, Wang J L, Debnath J C, Kennedy S J, Zeng R, Din M F M, Hong F, Cheng Z X, Studer A J and Dou S X, 2013 *J. Phys.: Condens. Matter* **25** 056001
[8] Johnson V, 1975 *Inorg. Chem.* **14** 1117
[9] Koyama K, Sakai M, Kanomata T and Watanabe K, 2004 *Jpn. J. Appl. Phys.* **43** 8036
[10] Kanomata T, Ishigaki H, Suzuki T, Yoshida H, Abe S and Kaneko T, 1995 *J. Magn. Magn. Mater.* **140–144, Part 1** 131
[11] NizioŁ S, Zach R, Sénateur J P and Beille J, 1989 *J. Magn. Magn. Mater.* **79** 333
[12] Caron L, Trung N T and Brück E, 2011 *Phys. Rev. B* **84** 020414
[13] Trung N T, Zhang L, Caron L, Buschow K H J and Bru□ck E, 2010 *Appl. Phys. Lett.* **96** 172504
[14] Morrison K, Moore J, Sandeman K, Caplin A and Cohen L, 2009 *Phys. Rev. B* **79**
[15] Liu E K, Zhu W, Feng L, Chen J L, Wang W H, Wu G H, Liu H Y, Meng F B, Luo H Z and Li Y X, 2010 *Europhys. Lett.* **91** 17003
[16] Güçlü F, Özdemir A, Dubenko I, Samanta T, Ali N, Kervan N and Kervan S, 2013 *J. Magn. Magn. Mater.* **327** 7
[17] Tegus O, Brück E, Buschow K H J and de Boer F R, 2002 *Nature* **415** 150
[18] Krenke T, Duman E, Acet M, Wassermann E F, Moya X, Manosa L and Planes A, 2005 *Nat. Mater.* **4** 450
[19] Wada H and Tanabe Y, 2001 *Appl. Phys. Lett.* **79** 3302
[20] Wang J L, Campbell S J, Cadogan J M, Studer A J, Zeng R and Dou S X, 2011 *Appl. Phys. Lett.* **98** 232509

PROCEEDINGS - 37th ANNUAL CONDENSED MATTER AND MATERIALS MEETING, 5 - 8 February, 2013. Wagga Wagga, NSW, Australia

Effect of External Electric Field on the Application of Graphene

Z. M. Ao,[a,b*] Q. G. Jiang,[a] and S. Li[a]

[a] *School of Materials Science and Engineering, The University of New South Wales, Sydney, NSW 2052, Australia.*

[b] *Centre for Clean Energy Technology, School of Chemistry and Forensic Science, University of Technology, Sydney, PO Box 123, Broadway, Sydney, NSW 2007 Australia*

External electric field, which is often encountered in practical applications, can induce substantial alterations in materials with respect to chemical potentials and electronic properties. In this work, based on first-principles calculations, it presents the effect of an external electric field on inducing the dissociative adsorption of H_2 and H_2O molecules for the application of graphene as hydrogen storage materials and in electronic devices, respectively.

1. Introduction

Graphene with unique electronic, thermal, and mechanical properties, has been regarded as one of the most promising candidates for the next generation of electronic materials and hydrogen storage materials [1]. Pristine graphene is not a good hydrogen storage material because of the very weak interactions between hydrogen and graphene through the van deer Wales interaction [2]. Hydrogenation of graphene is alternative promising way to store atomic hydrogen with hydrogen storage capacity up to 7.7 wt%. In addition, hydrogenation of graphene can also open the band gap of graphene, which is desirable for its application in electronic devices [3-5]. However, the hydrogenation reaction has high energy barrier [4], which we are trying to reduce in this work. In addition, in some application, for example as electrode materials of supercapacitors and as biomaterials supports, it is desirable that graphene is hydrophilic in order to improve the wetting between graphene and polar electrolytes or biological molecules [6,7].

External electric field *F*, which is often encountered in practical applications, could induce substantial alterations in materials with respect to their geometry, binding energies, vibrational spectra, chemical potentials and electronic properties [8]. For example, Zhou et al. found that the H-C bond in graphane could increase under an electric field, and finally H atoms at one side of graphane would be desorbed with increasing *F* [9]. Therefore, based on density functional theory (DFT) calculations, external electric field is considered in this work to apply to the graphene system to seek the possibility of lowering the energy barrier of hydrogenation and facilitating the transition of graphene from hydrophobic to hydrophilic through the dissociative adsorption of H_2O molecules on graphene.

2. Computational Methodology

The DFT calculations were performed using the DMOL3 code [10]. The generalized gradient approximation (GGA) with revised Perdew-Burke-Ernzerhof (RPBE) functional was employed as the exchange-correlation functional [11]. A double numerical plus polarization (DNP) was used as the basis set, while the DFT semicore pseudopotentials (DSPP) core treatment was employed to include relativistic effects that replaces core electrons by a single effective potential. Spin polarization was considered in the calculations. The convergence tolerance of the energy was set to 10^{-5} Ha (1 Ha = 27.21 eV), and the maximum allowed force

* E-mail: Zhimin.ao@uts.edu.au

and displacement were 0.02 Ha and 0.005 Å, respectively. To investigate the dissociative adsorption of H_2 or H_2O molecules on graphene surface, linear synchronous transition /quadratic synchronous transit (LST/QST) [12] and nudged elastic band (NEB) [13] tools in the DMOL3 code were used. These methodologies have been demonstrated as fantastic tools to search for the structure of the transition state (TS) and the minimum energy pathway. In the simulations, three-dimensional periodic boundary conditions were imposed, and all the atoms are allowed to relax. We minimized the interlayer interaction by allowing a vacuum width of 18 Å normal to the layer. The supercell used to investigate the dissociative adsorption of H_2 and H_2O molecules on graphene is shown in Figs. 1 and 3, respectively. Different size of supercell is used for two reactions for demonstrating the results clearly. The size of the supercell has only very limited effect on the final results.

3. Results and discussion

A. Electric field induced hydrogenation of graphene

Fig. 1 shows the favourite atomic structure before and after hydrogenation. Before hydrogenation, the H_2 molecule is physically adsorbed at the hollow site of graphene as shown in Fig. 1(a). The distance between the H_2 molecule and the graphene layer $d_{H2\text{-graphene}}$ is 2.612 Å with adsorption energy $E_{b\text{-}H2} = -0.153$ eV, which are consistent with other simulation results of $d_{H2\text{-graphene}} = 2.635$ Å and $E_{b\text{-}H2} = -0.159$ eV in Ref. [2]. For the case of atomic hydrogen adsorption on graphene, the favourable configuration is two H atoms adsorbed on two face-by-face carbon atoms in the same hexagon as shown in Fig. 1(b), which is consistent with the reported DFT result [14].

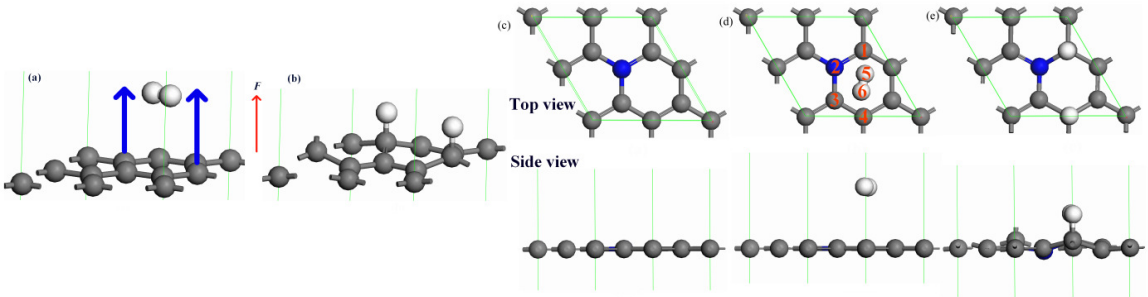

Fig. 1. The atomic structure of a H_2 molecule physical adsorption on pristine graphene (a), dissociative adsorption on pristine graphene (b), N-doped graphene (c), a H_2 molecule physical adsorption on N-doped graphene (d), and dissociative adsorption on N-doped graphene (e). The gray, white and blue balls are C, H and N atoms, respectively. The direction of the electric field is indicated by the arrow.

The energy minimum pathway for a H_2 molecule dissociative adsorption on graphene, that is from the structure of Fig. 1(a) to that of Fig. 1(b), is shown in Fig. 2(a). This dissociative adsorption reaction barrier E_{bar} is 2.734 eV, which is a little smaller than 3.3 eV found by others [14]. Regarding TS, the H_2 molecule is dissociated into two free H atoms without any binding with the C atoms. From Fig. 2(a), it is known that this reaction requires two steps: the H_2 molecule is dissociated into two free H atoms, then the two H atoms are bound to the two C atoms. Step one needs an energy of 2.7 eV to overcome the barrier and the second step releases an energy of 1.9 eV. Therefore, the dissociation of H_2 is the rate-limiting step, hydrogenation of graphenen is very difficult to realise due to the high energy barrier.

The effect of electric field on this reaction is investigated. The results show that E_{bar} decreases as the intensity of F increases. When F reaches -0.02 au (1 au = 5.14×10^{11} V/m), E_{bar} is negative to be -0.222 eV as shown in Fig. 2(b), which means that there is no energy barrier from IS to state 2. Thus, such a negative electric field can act as a catalyst to significantly speed up the hydrogenation process of graphene. However, the second step that two H atoms chemically adsorb on C atoms requires a high energy, which prevents the

hydrogenation of graphene. Alternatively, the free H atoms are considered to automatically bind with the C atoms once removing the electric field after H_2 dissociation since there is no potential barrier after TS as shown in Fig. 2(a). In addition, experiment has also indicated that the graphene layer can be automatically hydrogenated by free H atoms [15].

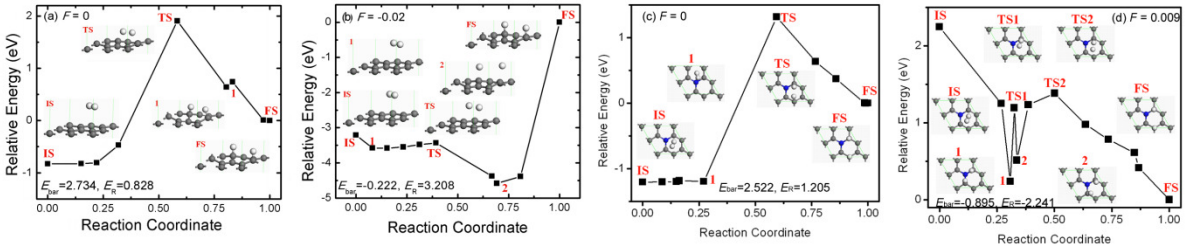

Fig. 2. The reaction pathway of a H_2 molecule that undergoes a dissociative adsorption on pristine and N-doped graphene under different electric field. (a) and (b) in pristine graphene system, (c) and (d) in N-doped graphene system. IS, TS, FS, and 1 and 2 represent initial structure, transition structure, final structure, and energy minimum states 1 and 2, respectively. The energy of FS is taken to be zero. The unit of F, E_{bar}, and E_R are atomic unit and electron volt, respectively, where E_{bar} is the energy barrier and E_R is the reaction energy.

Doping N into carbon nanotube was reported to reduce the energy barrier of hydrogen molecule adsorption [16]. Therefore, the effect of N doping of graphene on the dissociative adsorption of a H_2 molecule is considered here. The favourable atomic structure of N-doped graphene, a H_2 molecule physical adsorption of N-doped graphene, and a H_2 molecule dissociative adsorbed on N-doped graphene is shown in Figs. 1(c)-1(e). It shows that the planar structures remain after N doping and with H_2 physical adsorption, and the H_2 molecule is located on the hollow site of the carbon hexagon. Fig. 2(c) shows the pathway of the H_2 molecule dissociative adsorption on N-doped graphene. E_{bar} is 2.522 eV, which is a little smaller than 2.734 eV for the H_2 molecule dissociative adsorption on pristine graphene. When considering the electric field effect, we find that F reduces the barrier significantly. When F = 0.009 au as shown in Fig. 2(d), both E_{bar} and E_R are negative. Therefore, the electric field can induce molecular hydrogen dissociative adsorption in the N-doped graphene. In other words, the electric field and N doping are catalyzers for graphene hydrogenation.

B. Electric field manipulated reversible transition from hydrophobic to hydrophilic

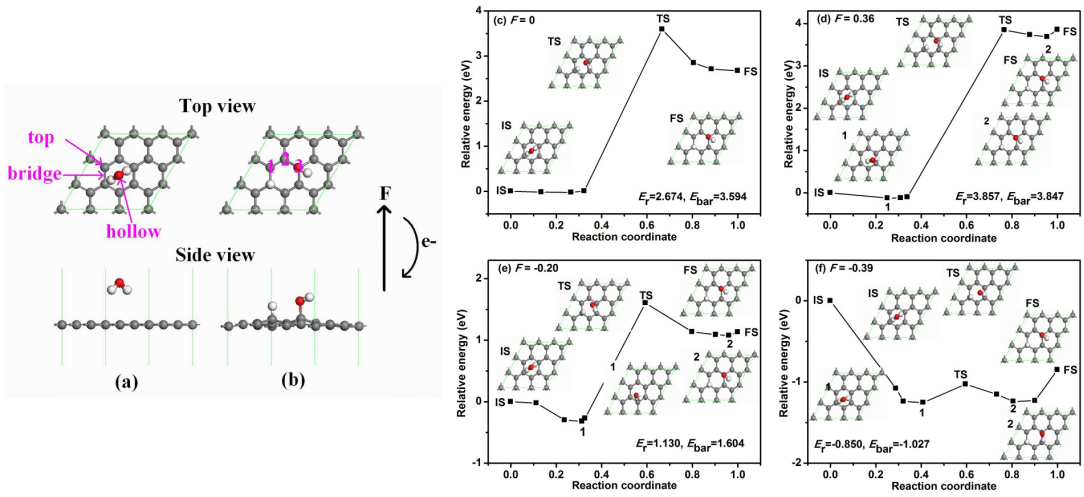

Fig. 3. Initial (a) and final structure (b) for a H_2O molecule dissociative adsorption on graphene. Reaction pathway of a H_2O molecule dissociative adsorption on grapheme under different electric field, F = 0 (c), F = 0.36 (d), F = -0.2 (e), and F = -0.39 (f). The red balls are O atoms. The unit of F is V/Å.

To understand the transition of graphene from hydrophobic to hydrophilic, which is

induced by the dissociative adsorption H_2O molecules on graphene, the reaction is studied by DFT calculations. The initial structure is shown in Fig. 3(a) where a H_2O molecule is physically adsorbed at the hollow site of C ring, while the final structure is shown in Fig. 3(b) where the H atom and HO group take the two face by face sites. The reaction pathways under different electric field are also shown in Fig. 3. It is known that the reaction barrier for the H_2O molecule dissociative adsorption is as high as 3.594 eV when without electric field as shown in Fig. 3(c). However, in the presence of an negative electric field as shown in Figs. 3(e) and 3(f), both E_{bar} and E_r decrease and they are even to be negative when F = -0.39 V/Å. The presence of the chemically adsorbed hydrophilic OH group makes graphene hydrophilic. When removing the electric field after dissociative adsorption, the reaction of H + OH → H_2O is considered, which is from FS to IS in Fig. 3(c). The reaction barrier and reaction energy are E_{bar} = 0.921 eV and E_r = -2.534 eV, respectively. As E_{bar} > 0.75 eV, which is believe that this reaction hardly occurs at ambient temperature. However, if a positive electric field is applied as shown in Fig. 3(d), E_{bar} and E_r of the reaction from FS to IS are respectively -0.006 and -3.717 eV. Therefore, the electric field can act as the switch to realise the reversible transition of graphene from hydrophobic to hydrophilic.

4. Conclusion

The dissociative adsorption of a H_2 and a H_2O molecule on graphene is investigated through DFT calculations for its potential application as hydrogen storage materials and in electronic devices. It is found that applying an external electric field can act a catalyst for the hydrogenation of graphene, which is a promising way to store hydrogen in its atomic form. Applying an external electric field can also induce the dissociative adsorption of H_2O molecules on graphene to realise the reversible transition of graphene from hydrophobic to hydrophilic, which is essential for applications in supercapacitors and in biomaterial supports.

Acknowledgments

Finance supports from the Vice-Chancellor's Research Fellowship Program of the University of New South Wales (SIR50/PS19184), and the Goldstar Award of the University of New South Wales (RG124422) are acknowledged.

References

[1] Geim A K, 2009 *Science* **324** 1530
[2] Ao Z M, Jiang Q, Zhang R Q, Tan T T, and Li S 2009 *J. Appl. Phys.* **105** 074307
[3] Novoselov K S, Geim A K, Morozov S K, *et al* 2004 *Science* **306** 666
[4] Ao Z M and Peeters F M 2010 *Appl. Phys. Lett.* **96** 253106
[5] Sofo J O, Chaudhari A S and Barber G D 2007 *Phys. Rev. B* **75** 153401
[6] Stoller M D, Park S, Zhu Y, An J and Ruoff R S 2008 *Nano Lett.* **8** 3498
[7] Pantelic R S, Suk J W, Hao Y F, Ruoff R S and Stahlberg H 2011 *Nano Lett*. **11** 4319
[8] Liu W and Jiang Q, 2010 *J. Comput. Theor. Nanosci.* **7** 2225
[9] Zhou J, Wu M M, Zhou X, and Sun Q, 2009 *Appl. Phys. Lett.* **95** 103108
[10] Delley B, 2000 *J. Chem. Phys.* **113** 7756
[11] Hammer B, Hanse L B and Nϕrskov J K, 1999 *Phys. Rev. B* **59** 7413
[12] Halgren T A and Lipscomb W N, 1977 *Chem. Phys. Lett.* **49** 225
[13] Henkelman G and Jonsson H, 2000 *J. Chem. Phys.* **113** 9978
[14] Miura Y, Kasai H, Diño W, Nakanishi H, and Sugimoto T, 2003 *J. Appl. Phys.* **93** 3395
[15] Elias D C, Nair R R, Mohiuddin T M G, et al, 2009 *Science* **323** 610
[16] Zhang Z and Cho K, 2007 *Phys. Rev. B* **75** 075420